AD_____

Award Number: W81XWH-13-1-0390

TITLE: Reciprocal Interactions between Multiple Myeloma Cells and Osteoprogenitor Cells Affect Bone Formation and Tumor Growth"

PRINCIPAL INVESTIGATOR: Michaela Reagan

CONTRACTING ORGANIZATION: Dana-Farber Cancer Institute, Inc
Boston, MA 0211

REPORT DATE: October 2014

TYPE OF REPORT: Annual

PREPARED FOR: U.S. Army Medical Research and Materiel Command
Fort Detrick, Maryland 21702-5012

DISTRIBUTION STATEMENT: Approved for Public Release;
Distribution Unlimited

The views, opinions and/or findings contained in this report are those of the author(s) and should not be construed as an official Department of the Army position, policy or decision unless so designated by other documentation.

REPORT DOCUMENTATION PAGE

Form Approved
OMB No. 0704-0188

Public reporting burden for this collection of information is estimated to average 1 hour per response, including the time for reviewing instructions, searching existing data sources, gathering and maintaining the data needed, and completing and reviewing this collection of information. Send comments regarding this burden estimate or any other aspect of this collection of information, including suggestions for reducing this burden to Department of Defense, Washington Headquarters Services, Directorate for Information Operations and Reports (0704-0188), 1215 Jefferson Davis Highway, Suite 1204, Arlington, VA 22202-4302. Respondents should be aware that notwithstanding any other provision of law, no person shall be subject to any penalty for failing to comply with a collection of information if it does not display a currently valid OMB control number. **PLEASE DO NOT RETURN YOUR FORM TO THE ABOVE ADDRESS.**

1. REPORT DATE	2. REPORT TYPE	3. DATES COVERED
October 2014	Annual Report	30 Sep 2013 - 29 Sep 2014

4. TITLE AND SUBTITLE

Reciprocal Interactions between Multiple Myeloma Cells and Osteoprogenitor Cells Affect Bone Formation and Tumor Growth

5a. CONTRACT NUMBER

5b. GRANT UMBER
W81XWH-13-1-0390

5c. PROGRAM ELEMENT NUMBER

6. AUTHOR(S)
Michaela Reagan
E-Mail: Michaela.r.reagan@Gmail.com

5d. PROJECT NUMBER

5e. TASK NUMBER

5f. WORK UNIT NUMBER

7. PERFORMING ORGANIZATION NAME(S) AND ADDRESS(ES)

Dana-Farber Cancer Institute
450 Brookline Ave.
Boston, MA. 02155

8. PERFORMING ORGANIZATION REPORT

9. SPONSORING / MONITORING AGENCY NAME(S) AND ADDRESS(ES)

U.S. Army Medical Research and Materiel Command
Fort Detrick, Maryland 21702-5012

10. SPONSOR/MONITOR'S ACRONYM(S)

11. SPONSOR/MONITOR'S REPORT NUMBER(S)

12. DISTRIBUTION / AVAILABILITY STATEMENT
Approved for Public Release; Distribution Unlimited

13. SUPPLEMENTARY NOTES

14. ABSTRACT

Clonal proliferation of plasma cells within the bone marrow (BM) affects local cells, such as mesenchymal stromal cells (MSCs), leading to osteolysis and fatality in multiple myeloma (MM). Consequently, there is an urgent need to find better mechanisms of inhibiting MM growth and osteolytic lesion development. To meet this need and accelerate clinical translation, better models of MM within the BM are required. We developed a clinically-relevant, 3D myeloma BM co-culture model that mimics bone cell-cancer cell interactions within the bone microenvironment. The co-culture model and clinical samples were utilized to investigate myeloma growth, osteogenesis inhibition, and myeloma-induced abnormalities in MM-MSCs. This platform demonstrated myeloma support of capillary-like assembly of endothelial cells and cell adhesion mediated-drug resistance (CAM-DR). Also, distinct normal donor (ND)- and MM-MSC miRNA signatures were identified and used to uncover osteogenic miRs of interest for osteoblast differentiation. More broadly, our 3D platform provides a simple, clinically-relevant tool to model cancer growth within the bone, useful for investigating skeletal cancer biology, screening compounds, and exploring osteogenesis. Our identification and efficacy validation of novel, bone anabolic miRs in MM opens the floodgate for novel approaches to cancer.

15. SUBJECT TERMS
Multiple Myeloma, Blood Cancer, Hematological Malignancy, Bone Metastasis, 3D Model, In vitro, silk scaffolds, osteogenic microRNAs.

16. SECURITY CLASSIFICATION OF:			17. LIMITATION OF ABSTRACT	18. NUMBER OF PAGES	19a. NAME OF RESPONSIBLE PERSON
a. REPORT	b. ABSTRACT	c. THIS PAGE			19b. TELEPHONE NUMBER *(include area code)*
U	U	U	UU	67	

Table of Contents

Introduction....4
Keywords....4
Accomplishments (Overview)....4
Impact....7
Changes/Problems....8
Products....8
Participants & Other Collaborating Organizations....9
Key Research Accomplishments: Data and Results....10
Conclusions....19
Reportable Outcomes....19
Publications, Abstracts and Presentations....19
Opportunities for Training and Professional Development....20
References:....20
Appendix I: Full Journal articles (2)....21

Introduction

Osteolytic cancers such as Multiple Myeloma (MM) develop via forward feedback mechanisms with local Mesenchymal Stem Cells (MSCs) in the bone marrow (BM), leading to devastating skeletal consequences (ie. pain, hypercalcemia, and fracture) and accelerated tumor growth(Roodman, 2004). MM cells insidiously hijack normal bone homeostasis to decrease osteoblastic activity and increase osteoclastic activity by altering local microenvironment cells(Reagan & Ghobrial, 2012). MM patient derived MSCs (MM-MSCs) exhibit decreased proliferation and osteogenesis, an inability to repair osteolytic damage, and display great patient-to-patient heterogeneity in their ability to undergo differentiation and induce changes in MM cells(Markovina et al., 2010; Reagan & Ghobrial, 2012; Yaccoby et al., 2006). The tumor BM microenvironment also supports tumor growth(Azab et al., 2012), induces chemoresistance and selects for tumor-initiating clones(Fuhler et al., 2010). Therefore, the work herein discusses our development of a realistic model of the abnormal BM seen in MM patients, which will greatly benefit translational research scientists. The research provides novel targets for anti-cancer treatment by helping to heal osteolytic lesions in cancer patients, and provides a new platform to study cancer-bone interactions.

Keywords

Multiple Myeloma, Blood Cancer, Hematological Malignancy, Bone Metastasis, 3D Model, *In vitro* model, silk scaffolds, osteogenic microRNAs, nanoparticles, osteolysis.

Accomplishments (Overview)

- **What were the major goals of the project?**
  - *See Statement of Work below.*
- **What was accomplished under these goals?**
  - *Please see the the 2 articles in Appendix 1. Also, please see Statement of Work below.*
- **What opportunities for training and professional development has the project provided?**

Honors, Training, Professional Development, Conference/Committee Participation based on or involving this work for Michaela Reagan:

- Abstract Submission, Dana-Farber Cancer Institute Post-Doctoral Retreat. September 2014.
- Application to Maine Medical Center, Portland Maine, for position as assistant professor.
- CURE (Continuing Umbrella of Research Experiences) Mentor to Undergraduate Student at UMass Boston (Mr. Ted Hilaire), Summer/Fall 2014.
- Invited Speaker, Maine Medical Center Research Institute, June 2014.
- Guest Speaker, Boston University High School Summer Education Program, Calculus Class July 2014.
- Scientific Committee Member of joint ECTS (European Calcified Tissue Society)- CABS (Cancer and Bone Society)-IBMS Conference in Rotterdam, Netherlands. April 2015.
- Conference Session Chair: IBMS Herbert Fleisch Workshop, Brugge, Belgium 2014 and Cancer and

Bone Society Meeting, Miami, FL 2013.

- IBMS Young Investigator Committee Member (2012-2014), Committee Co-chair (2013-2015).
- Herbert Fleisch Workshop Abstract Travel Award 2014.
- Best Poster Award, Dana-Farber Cancer Institute Post-Doctoral Retreat. Cambridge, MA. 9/30/2013.
- Offered a job as a Research Scientist I at Maine Medical Center Research Institute (MMCRI) in Scarborough, Maine at the end of her post-doc position at Dana-Farber. This position includes a position as assistant Professor at Tufts University, Boston MA, also. Until she begins her own lab, Dr. Reagan holds a position as Visiting Scientist at Maine Medical Center Research Institute and has begun collaborations with her new colleagues there. This work has also allowed her to apply for funding from the NIH through a pilot grant at MMCRI in collaboration with Dr. Clifford Rosen, who she met at a conference presenting her work supported by this funding.
- **How were the results disseminated to communities of interest?**
    - Work was presented at multiple conferences above, published in peer-reviewed journals, and also presented in an hour long course to a group of high school summer students (Boston University High School Summer Education Program, Calculus Class, July 2014).
- **What do you plan to do during the next reporting period to accomplish the goals?**
    - We plan to follow the Statement of Work we outlined in the grant. Also, we plan to continue established new collaborations with the bone expert, Dr. Clifford Rosen's lab in Maine (MMCRI), which has been a great support in terms of the mouse work and bone phenotype studies.

Statement of Work	Actual Tasks Performed
Task 1 (Months 1-8)	
a) Seek regulatory approval from IRB	All approvals have been sought and obtained.
b) Make Silk Scaffolds (Carmen Preda)	Silk scaffolds have been formulated and obtained from Tufts.
c) Isolate MSCs from bone marrow	Marrow MSCs have been collected from IRB-approved sources.
d) Generate Models of osteogenesis in 3D scaffold cultures.	This has been designed, optimized and performed with microCT, confocal imaging, H&E and alizarin red staining for validation.
e) Assess GFP+/Luc+ MM1S, OPM2, other cells, on scaffolds in response to osteoprogenitors using confocal imaging	This has been done with MM1S, OPM2, RPMI cells, as well as primary patient cells, and imaged with confocal imaging.
f) Remove stromal and MM1S cells from mono- and co-cultures, separate using FACS (fluorescence-activated cell sorting) or MACS™ magnetic sorting beads, assess both cell types for proteomics, mRNA expression and miRNA expression.	This has been done using FACS and cells were assessed for miRNA, mRNA and proteomics. Focus remained on stromal cells, as the cultures of myeloma cells alone did not grow well and so were hard to compare to the co-culture systems. Also, due to low numbers of cells obtained after flow sorting, only miRNA analysis was deeply pursued further and done in replication.
g) Validate changes in stroma and in myeloma using immunohistochemisty, flow cytometry, and/or western blotting	This was done using nanoString molecular biology analysis and q-RT-PCR. As we began focusing on microRNA expression changes in MM vs ND MSCs, IHC, WB and Flow cytometry were irrelevant.
g.i) Validate results in osteoprogenitors regarding bone differentiation	This was done using the confocal microscopy and histology for alizarin red staining, to show that indeed MM cells do inhibit osteogenesis and patient MM-MSCs don't differentiate correctly.
g.ii) Characterize functional differences between normal and myeloma osteoprogenitors samples using assays for proliferation	This has been performed using cell counting of both clinical samples (ND- and MM-MSCs), and in the 3D Model with vs without MM1S myeloma cells using direct cell counting.
g.iii) Culture ND-MSCs with and without MM cells for different time regimens to determine if changes induced in MSCs are reversible and how long it takes for these changes to arise	This question of reversibility has not been addressed yet, but remains under investigation in collaboration with Shokichi Tsukamoto in our lab.
g.iv) Explore methods of reversing the effects of cancer on osteoprogenitors such as knockdown or	This was done using miRvana mimics and inhibitors in vitro to increase and decrease the expression of certain microRNAs that

overexpression techniques, pharmaceuticals, neutralizing antibodies, or cell therapies.	differed in ND- vs MM-MSCs from clinical samples and from the 3D co-culture system (see data below). In a related project, I used our findings to study if increased osteogenesis of osteoprogenitors inhibits tumor growth, which was published in PNAS, June 2014.
Task 2: Develop an *in vivo* model from osteo-transgene mice and Vk*myc MM cells. (Months 1-15) (Aim 1b and 2b).	
a) Begin ACURO and IACUC approval for a total of 90 mice	I wrote an entirely new IACUC approved protocol for this purpose, and obtained ACURO approval for this work.
b) Isolate GFP+CD138+ MM cells from Vk*myc mice using FACS	The cells we obtained were not GFP+, but we did obtain CD138+ Vk*Myc cells and are currently still attempting to label these with Luciferase and GFP, which is challenging since they don't grow *in vitro*. Cells are being expanded *in vivo*.
c) Inject MM cells into osteo-transgene mice and assess disease course.	We have initiated these studies and have preliminary data; this needs to be validated before we can be certain of the meaning.
i) Refine model variables such as numbers of Vk*myc-MM cells injected, injection site, and timeframes.	We have done this and are still in the process of perfecting the model. We have shown that bone metastasis and osteolysis occurs with tail-vein injection and tumor cell expansion works well when injected subcutaneously in matrigel. Timeframes as dependent on number of cells injected is still being studied, as are the differences in metastatic sites based on different methods of implantation (ex: sub-Q, within a donor mouse femur).
ii) If necessary, develop a NOD/SCID model where osteoprogenitor cells from osteo-transgene mice are isolated based on fluorescence (and hence osteogenic status) and co-injected with Luc+ MM1S cells. (Aim 1b Alternative)	We have not had to pursue this alternative direction since it appears that Vk*Myc cells are growing well in the Black6 background.
2) Task 3: Utilize the *in vivo* model of Task 2 to address biological questions: 1) how do different types of osteoprogenitors affect MM cells? and 2) how do MM cells affect different types of osteoprogenitors? 3) What new targets and therapies does this work suggest? (Months 15-21) (Aim 1b and 2b). a) Identify effects of osteoprogenitor cells on MM1S. (Aim 1b) i) Assess disease progression and bone marrow homing using bioluminescent imaging, *in vivo* fluorescent confocal microscopy of the calvaria, bone marrow flow cytometry, survival, mouse weight, and IHC. ii) Determine differential disease progression and preferential bone homing based on osteoprogenitor status. Once osteoprogenitor subtypes are identified as preferentially tumor-supportive *in vitro* and *in vivo*, lentiviral or RNAi knockdown or overexpression methods will be used to elucidate underlying mechanisms of osteoprogenitor support of MM disease progression.	As planned, this step will be pursued during the next 1 year research period. Vk*Myc myeloma cells will be expanded in mice subcutaneously and infected with luciferase/GFP genes, and then administered to Ocn-Cre Mice that are being bred and genotyped and analyzed for their changes in their bone microstructure (using uCT and histology).
b) Identify effects of MM1S on osteoprogenitor cells.(Aim 2b) i) Utilize live *in vivo* calvaria confocal imaging, dual-energy X-ray absorptiometry for bone density, and serum analysis for ALP or osteocalcin, (osteogenesis markers) and serum TRAP 5b (bone resorption markers).	We are on track to perform this work over the next 1 year.
c) Perform endpoint analysis including histology for bone health, IHC for characterization of osteoprogenitor subtypes within endosteal and periosteal surfaces, and microCT/X-ray analysis for osteolytic formation.	This will also be performed over the next 1 year period.
d) Test therapies for their ability to correct and normalize	This will be done over the next 1 year; we hypothesize that using

osteoprogenitors, enable bone healing, and reduce tumor burden in mouse models and assess results using techniques described above (BLI, histology, in vivo confocal, bone marrow flow cytometry, microCT, serum biomarkers, mouse weight, etc.) i) Explore decoy ligands, exogenous proteins, ECM proteins, small molecule inhibitors or alternative delivery mechanisms in Aim 2 to normalize aberrant osteoprogenitors and impede stromal support of MM.	Sost inhibitors may be one interesting and clinically translatable direction for this work.
Task 4: Compile data, write manuscript, submit to high-impact journal and perform extra experiments potentially requested by reviewers. (Months 21-24).	We have already done some of this work, as we published a manuscript in Blood this year, and we plan to publish a review paper in Bone within the next few weeks. We will hopefully also publish another manuscript of original research at the 21-24 month time point on the in vivo work described in Task 3.

Impact

What was the impact on the development of the principal discipline(s) of the project? Our work has opened the door and revealed the ability for microRNAs to affect osteogenesis, which could be a novel mechanism to heal osteolytic lesions and block tumors from growing in bone. Our work has also demonstrated the ability to target the bone marrow to modify the bone before cancer has arrived, to make the microenvironment less hospitable to cancer cells, by using bortezomib-loaded bisphosphonate-conjugated nanoparticles. We have developed novel technologies (3D Bone models, and bone-targeting nanoparticles), and novel results (specifically that microRNA-199a is able to induce osteogenic differentiation), and novel findings (that the bone can be modulated to make it less hospitable to cancer cells, and that microRNA levels are significantly different in MSCs from normal donors and myeloma patients). We are building on this work to better understand how cancer grows in the bone and how we can better stop its growth and destruction of the bone marrow. We are currently discussing performing clinical trials with bone-targeting nanoparticles with bortezomib to reduce off-target side effects associated with bortezomib.

What was the impact on other disciplines? Many other types of bone cancer, such as metastatic breast or prostate cancer, may benefit from the work described here. We have demonstrated that stromal cells from cancer patients are abnormal and that one of the abnormalities is expression of a certain microRNA, and that by correcting that microRNA, you can return the stromal cells to normal function and osteoblastic differentiation.

What was the impact on technology transfer? It is possible that government research or industries will now start to research how they can target or deliver certain microRNAs to the bone marrow to affect bone strength and normalize the bone cells, which have been altered by cancer cells. Also, a start-up company called BIND may build on the bortezomib nanoparticle technology and may start to produce these nanoparticles in much higher quantities so that they can be used in more cancer trials and eventually, hopefully, in patients.

What was the impact on society beyond science and technology? Our research will potentially have impact on changing the way society sees cancer of the bone. If we are successful in showing that the bone microenvironment is able to foster or inhibit bone cancer growth, we may be able to empower individuals more into prevention of bone cancer, which is something that people currently do not think they are personally able to predict or change. If we can show that stronger bones are better able to protect against bone cancer, we may change people's attitudes towards exercise and bone strength and give them even more reasons to do weight-training exercises. We may thusly prevent future cancers or

inhibit osteolytic lesion development, but much of this work still needs to be carried out within the next year to show how and why stronger bones could prevent myeloma growth.

Changes/Problems

Nothing to Report

Products

Publications, conference papers, and presentations

Report only the major publication(s) resulting from the work under this award.

Peer-Reviewed Scientific Journals Publications:

1. Swami A & Reagan MR*, Basto P, Mishima Y, Kamaly N, Glavey S, Zhang S, Moschetta M, Seevaratnam D; Zhang Y, Liu J, Memarzadeh T, Wu J, Manier S, Shi J, Bertrand N, Lu ZN, Nagano K, Baron R, Sacco A, Roccaro AM, Farokhzad OC, Ghobrial IM. 2014. Engineered Nanomedicine for Myeloma and Bone Microenvironment Targeting. *PNAS;*111(28):10287-922014. **Co-first authorship.* Acknowledgement of federal support (yes).

2. Reagan MR, Mishima Y, Glavey S, Zhang Y, Manier S, Lu ZN, Memarzadeh M, Zhang Y, Sacco A, Aljawai Y, Tai Y-T, Ready JE, Shi J, Kaplan DL, Roccaro AM, Ghobrial IM. 2014. Investigating osteogenic differentiation in Multiple Myeloma using a novel 3D bone marrow niche model. *Blood*;124(222):3250-3259.
Acknowledgement of federal support (yes).

3. Reagan MR, Rosen CJ and Ghobrial, IM. Indirect and Direct Roles of Osteoblasts in Multiple Myeloma. Review in Preparation for submission to *Bone.*

Other publications, conference papers, and presentations.

Oral Presentations/Abstracts:

Invited Speaker and Honorarium Recipient, Center for Clinical & Translational Research, Maine Medical Center Research Institute, May 2014.

Modeling Multiple Myeloma in a Tissue-Engineered Bone Marrow Niche. IBMS: Herbert Fleisch Workshop. March, 2014. Brugge, Belgium.

Nanoparticle Design For Bone-Specific Chemotherapy and Microenvironmental Targeting In Multiple Myeloma. ASH Conference Dec. 10, 2013. New Orleans, Louisiana.

Multiple Myeloma bone marrow derived mesenchymal stem cells (MSCs) show decreased osteogenesis in part due to decreased expression of microRNA hsa-mir-199a-3p, miR-15a-5p and miR-16-5p. IBMS-Cancer and Bone Society Conference, November 7-10, 2013. Miami, Florida.

Poster Presentations/Abstracts (First Authorship):

Modeling Multiple Myeloma in a Tissue-Engineered Bone Marrow Niche. IBMS: Herbert Fleisch Workshop. March, 2014. Brugge, Belgium.

MicroRNA-Dependent Modulation Of Osteogenesis In a 3D In Vitro Bone Marrow Model System Of Multiple Myeloma. ASH Conference Dec. 8, 2013. New Orleans, Louisiana.

Multiple Myeloma bone marrow derived mesenchymal stem cells (MSCs) show decreased osteogenesis in part due to decreased expression of microRNA hsa-mir-199a-3p, miR-15a-5p and miR-16-5p. To be presented at IBMS-CIBD Conference, November 7-10th 2013. Miami, Florida.

Novel Target Identification: Multiple Myeloma bone marrow derived mesenchymal stem cells (MSCs)

how decreased osteogenesis in part due to decreased expression of microRNA hsa-mir-199a-3p. Dana-Farber Cancer Institute Post-Doctoral Retreat, September 20, 2013. Cambridge, Massachusetts.

- **Technologies or techniques**
  The 3D model culture technique has been published and at the request of researchers at the Garvan Institute in Sydney, Australia, samples of silk scaffolds have been sent to Dr. Michelle McDonald and Dr. Peter Croucher there. We will help them use these scaffolds to model dormancy of myeloma cells in the bone marrow niche and are committed to helping any other researcher who would like to try to use the model by sending some sample scaffolds or teaching them to make their own and helping them troubleshoot any issues.

- **Inventions, patent applications, and/or licenses**
  None to report.

- **Other Products**
  Cell lines are being developed that have GFP and Luciferase expression in a Vk*Myc cell line. Protocols for genotyping and profiling Osteo-transgene mice will be made available once that research is complete, and all protocols for the 3D model have been published in *Blood*. Data has been uploaded to the GEO database that describes the microRNA expression differences in healthy donor vs myeloma patient donor MSCs.

Participants & Other Collaborating Organizations

Name:	Michaela Reagan
Project Role:	PI
Researcher Identifier (e.g. ORCID ID):	
Nearest person month worked:	12
Contribution to Project:	Dr. Reagan has performed and oversaw all work in this project.
Funding Support:	This award.

- **Has there been a change in the active other support of the PD/PI(s) or senior/key personnel since the last reporting period?**
  - No/Nothing to Report.
- **What other organizations were involved as partners?**
  - **Organization Name:** Tufts University
  - **Location of Organization:** Medford, MA, USA
  - **Partner's contribution to the projec**t
    - **Financial support**: None
    - **In-kind support:** Silk Scaffolds. Tufts Biomedical Engineering Dept staff, Mrs. Carmen Preda, worked

  - **Organization Name:** Maine Medical Center Research Institute
  - **Location of Organization:** Scarborough, ME, USA
  - **Partner's contribution to the projec**t
    - **Financial support**: None
    - **In-kind:** Advice, consultation, collaboration on Ocn-Cre/DTR mouse work.

Key Research Accomplishments: Data and Results

Although key data have been shown in the attached manuscripts, there was also substantial data not shown in the manuscripts or important to highlight here.

As part of Task 1, we validated first that we could culture MSCs with Myeloma cells. *In vitro* we found that MSCs significantly increased proliferation of myeloma cells using cell counting at days 0 and day 6 (Figure 1).

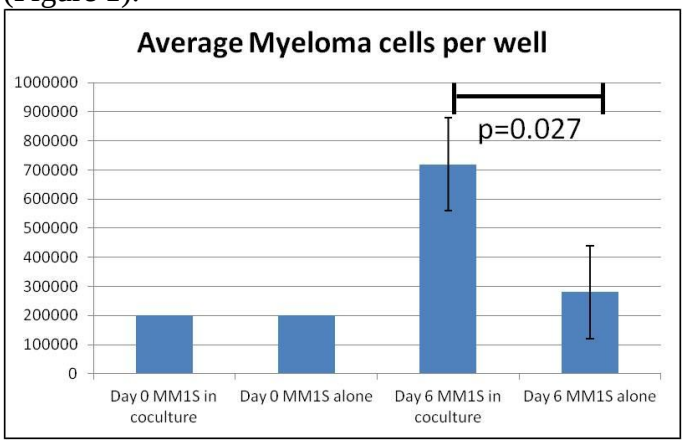

Figure 1: MSC induced proliferation of myeloma MM1S tumor cells

We also verified this finding by looking at the tumor cells under a fluorescent microscope with representative images, as shown in Figure 2 below, from 3 different wells.

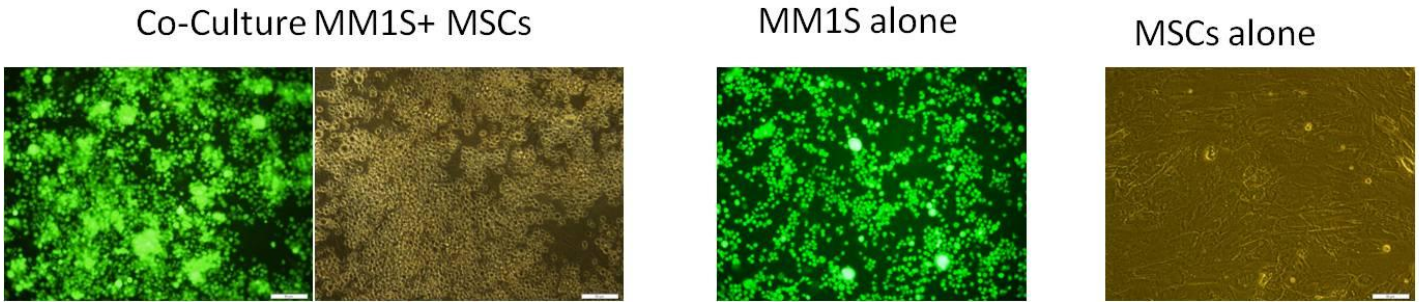

Figure 2: Increased MM1S proliferation and adhesion of MM1S to stroma and increased clumping over stroma. Concurrently, observed inhibited stromal growth, which was quantified by cell counting using nuclear staining (Hoescht), which was put into the Blood manuscript.

One of the major challenges of the long-term culture of myeloma cells with MSCs on the 3D model was cell labeling. The first dye we used to stain the MSCs for the experiment was the cell tracker dye “DiD”. Unfortunately, this dye’s fluorescent signal became diminished over time, with each cell replication, to the point that we were not able to produce very good images of the MSCs on the scaffolds by week 4, as shown in Figure 3 below. Our next step was to use a TurboRed (RFP)-containing plasmid packaged into a lentivirus to infect the cells and increase the signal. This allowed us to flow sort the cells from the scaffolds, and this is the data we used for further work and presented in the Blood manuscript.

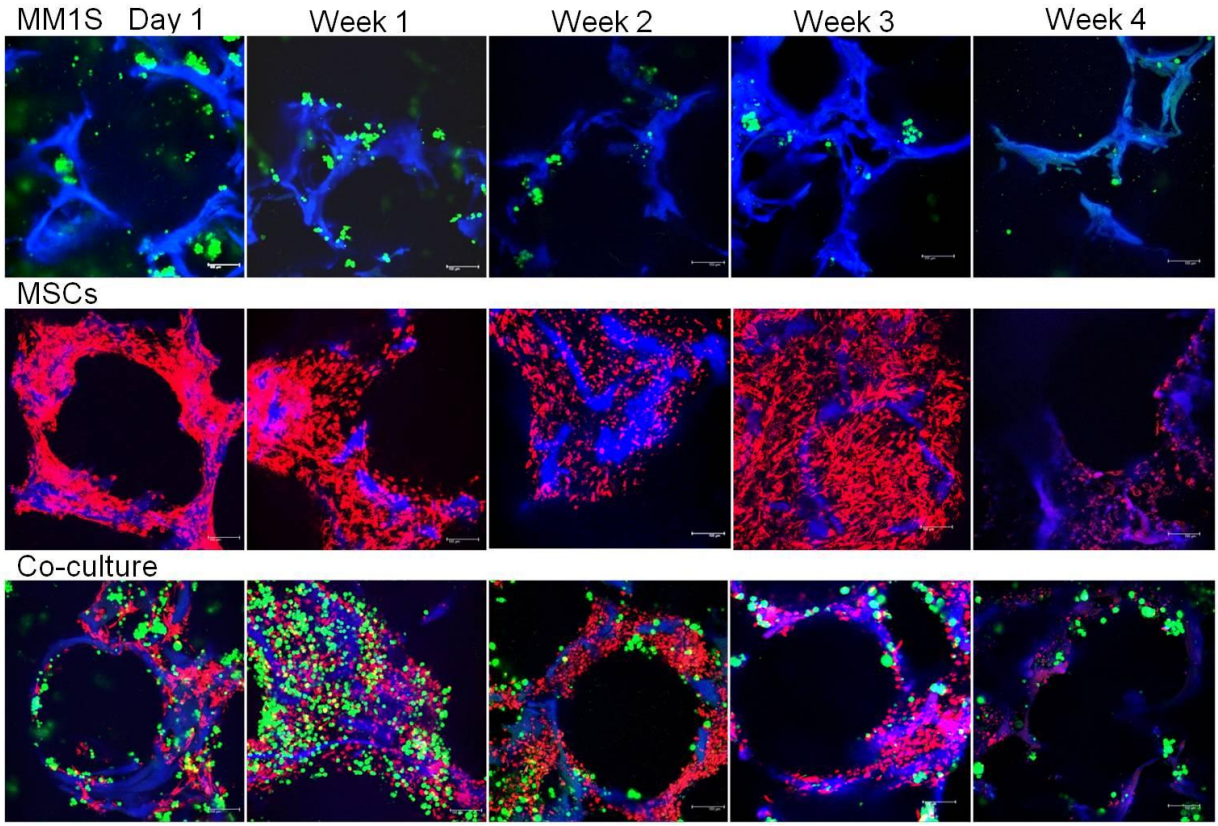

Figure 3: Silk Scaffolds imaged on confocal microscope from Day 1, and weeks 1,2,3 &4. MSCs are labeled red with DiD and myeloma cells are green and expressing GFP and luciferase. We determined the cell tracker dye (lipophilic DiD) would not be an acceptable labeling mechanism for MSCs over the long-term due to reduced signal over time.

We also initially attempted to simply use mechanical disruption of the 3D cultures to remove the myeloma cells from the scaffolds for Task 1, but we found that this would not help us to separate the cells because this process also washed away the MSCs that were on the scaffolds. This is shown in Figure 4. We then used FACS (Fluorescently-activated cell sorting) to separate the myeloma cells and the MSCs based on the different spectral properties of the cells. An example of this is shown in Figure 5.

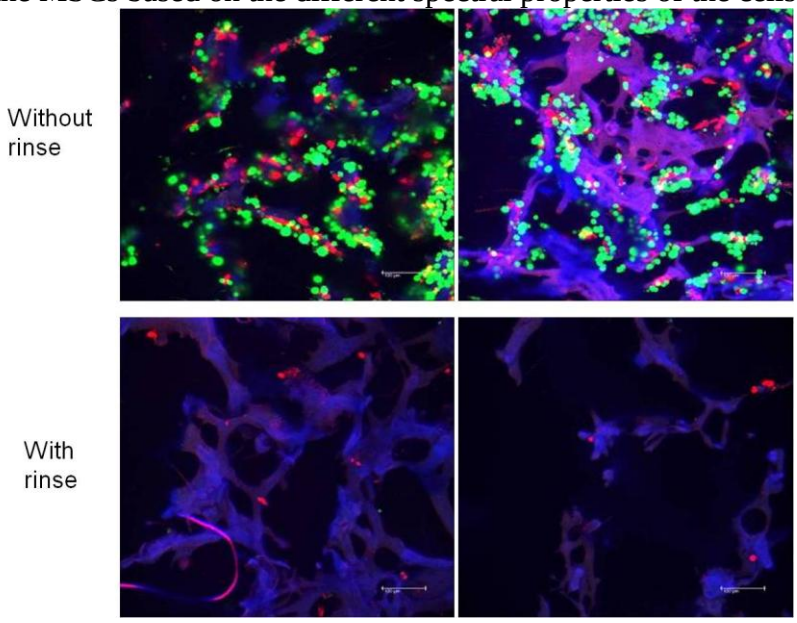

Figure 4: Silk Scaffolds (Purple) shown with MSCs (red) and with MM1S cells (green). Although the mechanical rinsing of scaffolds was able to remove almost all of the MM1S cells, the MSCs were also removed from the scaffold, making this an unreliable method for removing MM1S cells from scaffolds. From this, we decided to use rinsing, trypsiniation, and then FACS to separate the two cell types for further miRNA and mRNA analysis.

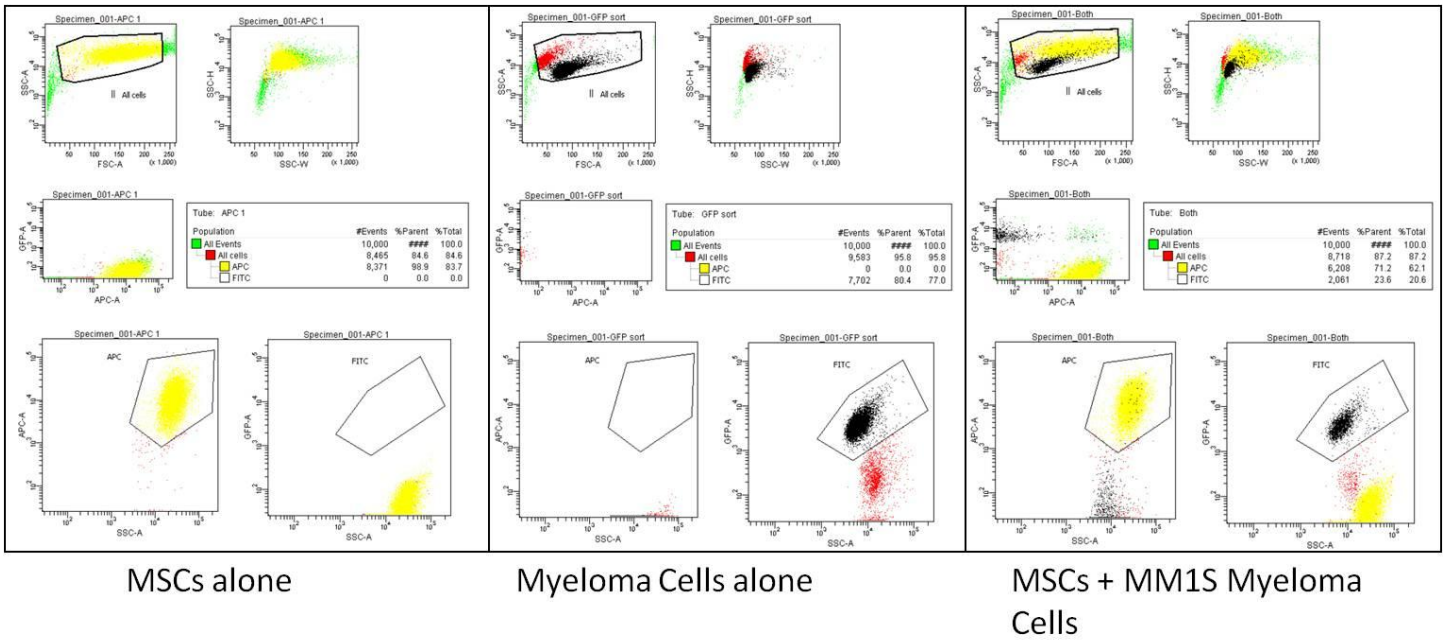

MSCs alone | Myeloma Cells alone | MSCs + MM1S Myeloma Cells

Figure 5: FACS (Fluorescently-activated cell sorting) of cells from scaffolds: MSCs alone, Myeloma cells alone or Myeloma plus MSCs. This method was then used for the rest of the analysis to isolate cells from scaffolds.

microRNAs were analyzed from patient samples (healthy vs myeloma stroma) and from the 3D Model stromal cells sorted from scaffolds (monocultured vs cultured with myeloma cells in osteogenic medium for 2 weeks) and all miRNA nanostring data was uploaded to the GEO database under accession number GSE60423. MicroRNAs identified as significantly different between ND-MSCs and MM-MSCs in patients (Figure 6A) and in the 3D model (Figure 6B) were summarized in Table 1 below and further investigated using miRNA mimics or miRNA inhibitors.

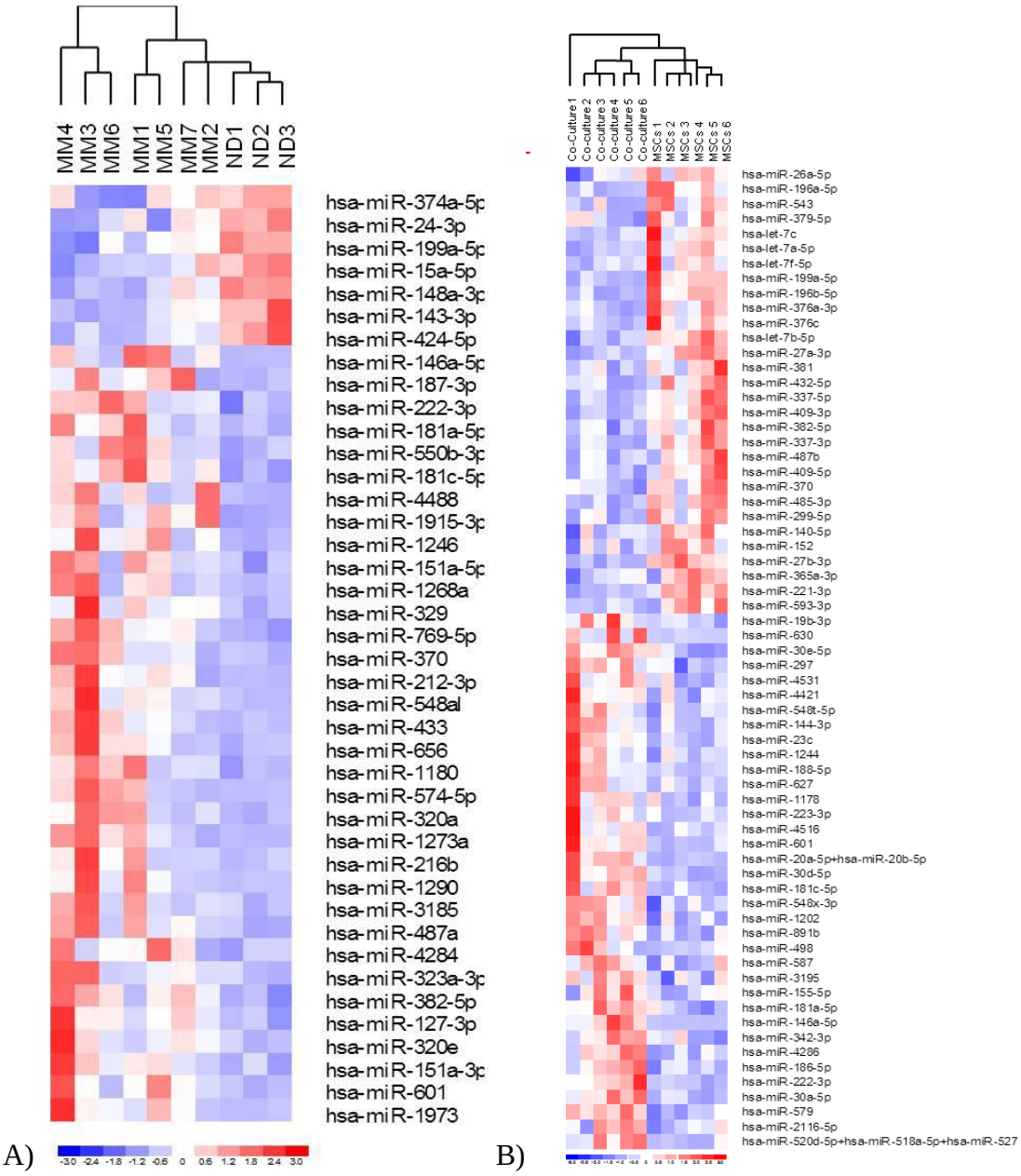

Figure 6: microRNA nanostring data from patient samples (A, left) and 3D model (B, right). MSCs were collected, lysed in Trizol, and processed for microRNAs using Qiagen's microRNA easy mini kit. microRNAs were then quantified using a nanodrop and expression of 800 microRNAs was analyzed using a Nanostring microRNA panel.

Table 1: **MicroRNAs altered in MSCs by Myeloma**. Six microRNAs were found to be similarly upregulated (5 miRs) or downregulated (1 miRs) in the 3D system (MSCs co-cultured with GFP^{+}MM1S vs. MSCs alone, after 2 weeks in co-culture in osteogenic, no-dexamethasone media) and in patient vs. normal samples (MM patient MSCs vs. normal donor MSCs)**.** Fold changes, fc≥1.5, p<0.05, n≥3, 2-tailed T-test, average expression>25 nanoString counts.

miRNA Name	Fold Change, 3D Model (MSCs in co-culture with MM1S vs Alone)	p-value, 3D Model (MSCs in co-culture with MM1S vs Alone)	Fold Change, MM vs ND MSCs	p-value, MM vs ND MSCs
hsa-miR-199a-5p	**-2.019**	**0.00086974**	**-1.917**	**0.00115665**
hsa-miR-181a-5p	**1.771**	**0.00362835**	**3.190**	**0.02106839**
hsa-miR-181c-5p	**2.135**	**0.00276756**	**3.078**	**0.00192591**
hsa-miR-222-3p	**2.152**	**0.00332040**	**1.821**	**0.01680615**
hsa-miR-601	**2.546**	**0.00738047**	**3.637**	**0.02449335**
hsa-miR-146a-5p	**17.175**	**0.00405939**	**15.353**	**0.02622689**

Those microRNAs that were increased in MM conditions (Table 1, bottom 5 microRNAs) were analyzed using inhibitors. However, the inhibitors did not seem to affect functional osteogenesis of MSCs (shown below in Figure 7, 2 of 4 different MM patient MSCs used). In contrast, the mimics used to increase levels of hsa-miR-199a were able to significantly increase the osteogenic differentiation of MSCs (shown in the Blood manuscript and below in Figure 8).

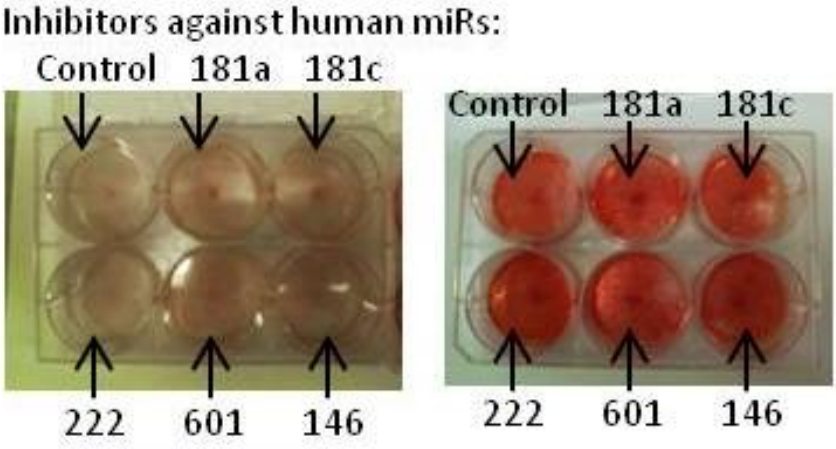

Figure 7: Inhibition of microRNAs identified as overexpressed in MM-MSCs (refer to Table 1) from 3D model and clinical samples was not able to show any functional change in osteogenic differentiation in MSCs and was not further pursued. Of note, the MSC donor on the right seemed to have high baseline osteogenic potential compared to most MM-MSC samples, perhaps due to treatments the patient was on. These microRNAs may be very important in explaining other differences between normal MSCs and MM-MSCs and should be further investigated for the clinical implications of their altered expression in MM patients, as the effects may not be related to osteogenic alterations.

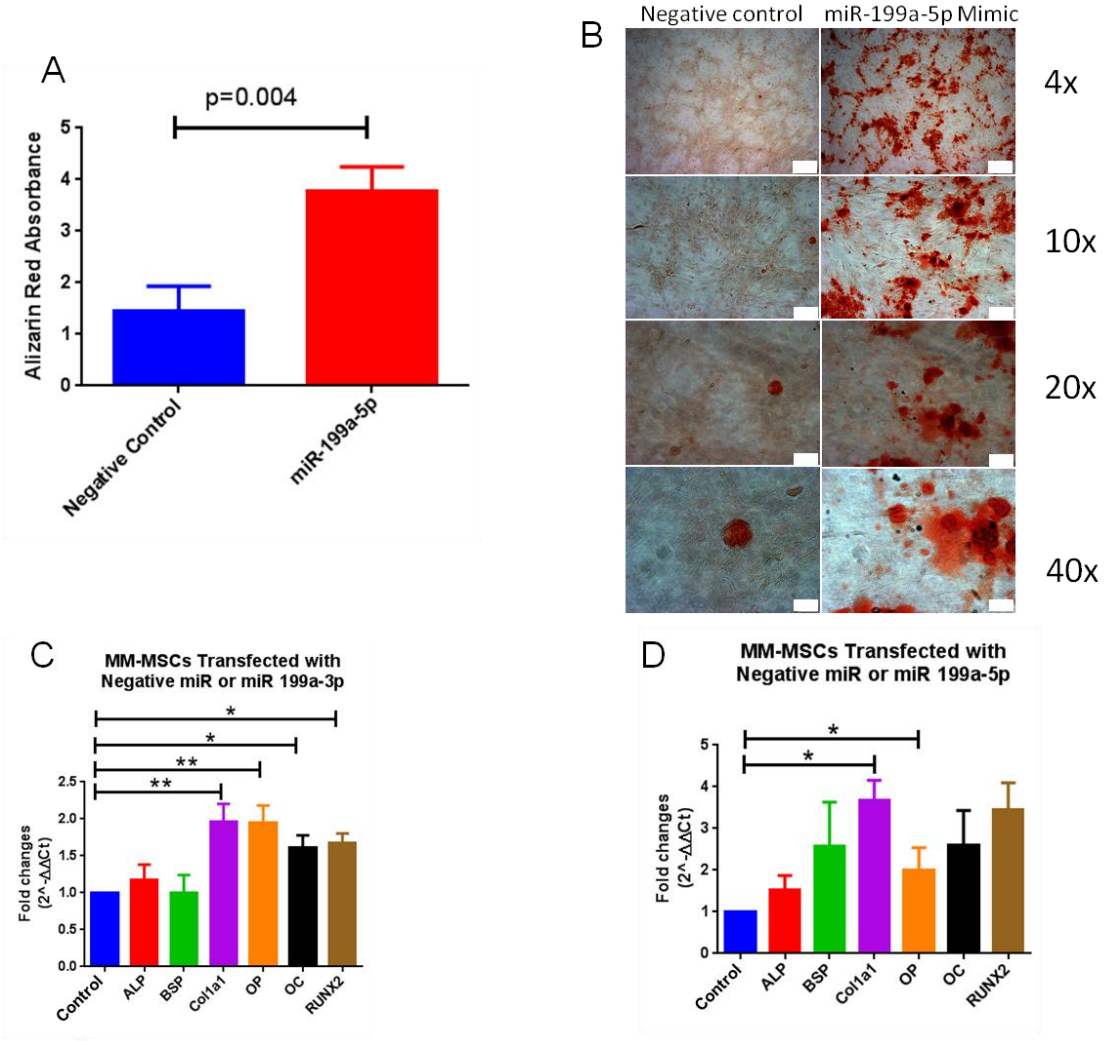

Figure 8: Osteogenic Induction by microRNA 199a-5p. A) Quantification of Alizarin Red Staining of MSCs treated with negative control microRNA or miR-199a-5p mimic. B) Representative images of fixed samples of MSCs differentiated with Negative control microRNA mimics or miR-199a-5p mimics. C) qRT-PCR quantification of gene expression of osteoblast lineage mRNAs in MM-MSCs treated with miR-199a-3p or miR-199a-5p (D). Alkaline phosphatase (ALP), integrin-binding sialoprotein (BSP), collagen type I alpha 1 (Col1a1), osteopontin (OP), osteocalcin (OC), and runt-related transcription factor 2 (RUNX2).

As part of Task 1g, we also examined the differences between primary samples in terms of mRNA expression using a Nanostring panel of 230 cancer-associated genes in MM-MSCs and ND-MSCs (Figure 9). Of interest was the increased expression of certain cell cycle kinase inhibitors CDKN2A (cyclin-dependent kinase inhibitor 2A) and CDKN1A (cyclin-dependent kinase inhibitor 1A) in MM samples. The elevated expression of these genes may partially explain why we see inhibited proliferation of MM-MSCs and may be a novel target in the attempt to stimulate these cells to overcome senescence in myeloma patients and begin to differentiate into osteoblasts again. This hypothesis has not been further investigated as of yet.

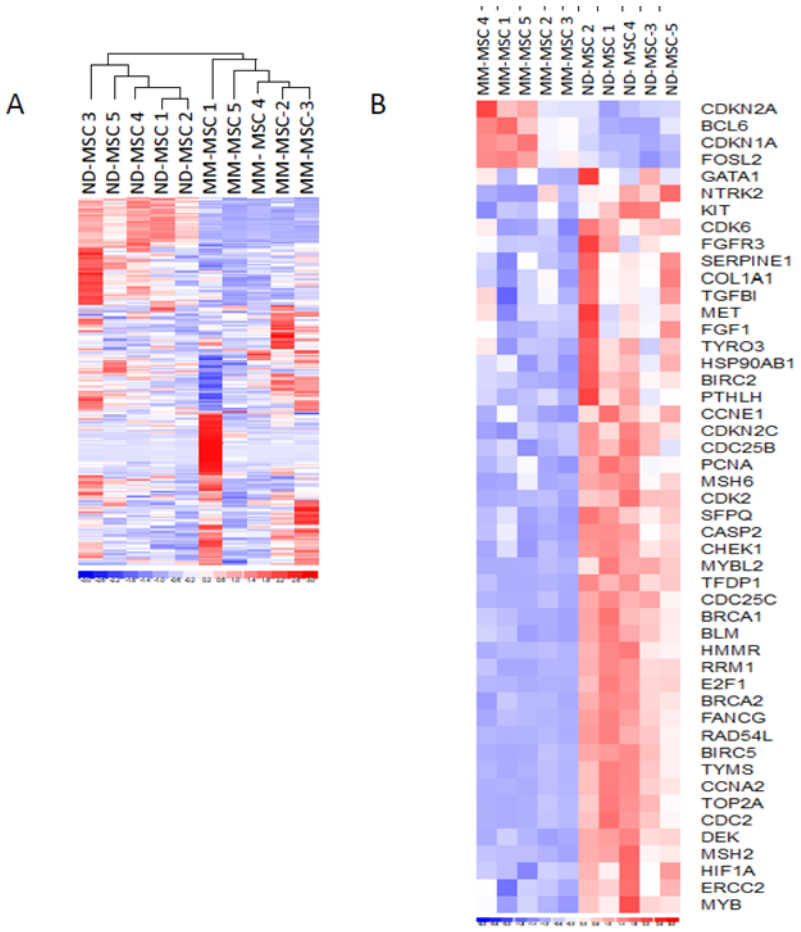

Figure 9: mRNA profiling of MM vs ND-MSCs. (a) Unsupervised clustering distinguishes MM- and ND-MSCs (passage 2) based on 230 cancer-related mRNAs (Nanostring analysis). (b) Of these, 49 mRNAs were significantly different ($p<0.05$, ≥1.3 fold change, MM- vs ND-MSCs).

Also as part of Task 1g.iv, we explored bortezomib, due to prior reports of anabolic action, and found that *in vitro* treatment of MSCs, and in vivo whole body treatment of mice, was able to induce osteogenic differentiation (Figure 10). This data was then used to build upon, validate *in vivo*, and used to further a collaboration with MIT on bone-targeting nanoparticles for myeloma, which was published in PNAS 2014. This work with bortezomib-bone homing nanoparticles would not have been done without the methods and skills used and learned for the 3D model work that this grant supported.

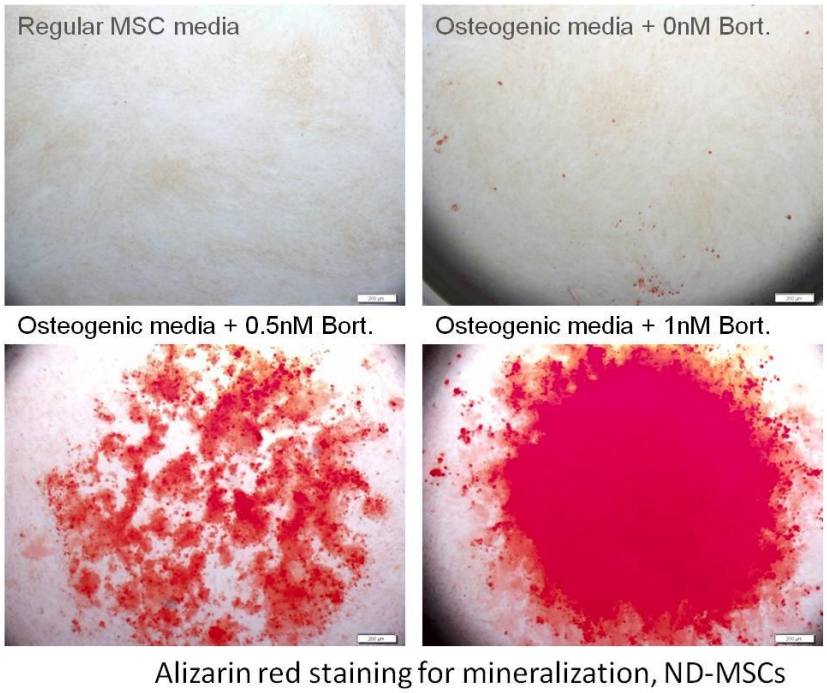

Figure 10: Alizarin Red staining after 1 wk of differentiation demonstrates ability for bortezomib to increase osteogenic differentiation of bone marrow-derived MSCs. Bortezomib treatment in early stages may prove be a novel tool to increase bone formation in MM patients and protect against osteolysis.

We have also cultured primary patient myeloma cells on the silk scaffolds (Figure 11) seeded with MSCs and we find that MM patient cells (CD138 bead selected) prefer to grow on MSCs rather than on naked silk scaffolds, similar to our findings of MM cell lines on scaffolds. Due to the nature of patient-to-patient tumor cell heterogeneity, we have decided, for our studies, to use myeloma cell lines for analysis of miRNA changes in MSCs, but future directions could use this 3D Model to make patient-specific bone marrow niche mimics for personalized drug or miRNA screens or drug resistance analysis.

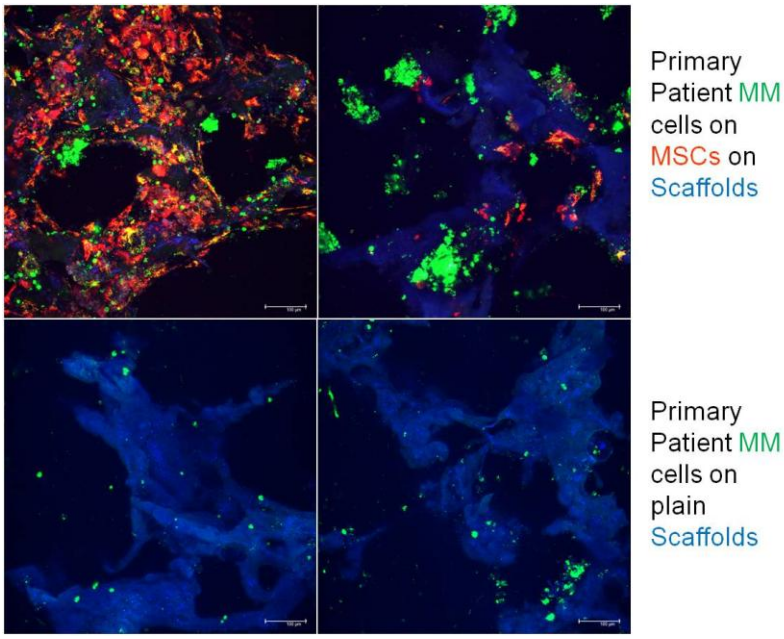

Figure 11: Confocal Imaging at Day 4 of Primary Patient MM cells (green) on scaffolds seeded with MSCs(red/orange) or on scaffolds alone (blue). MM cells show preference for growing on MSCs compared to the blank scaffolds.

As part of Task 2, we are working on the osteogenic transgene mice Ocn-Cre/DTR (which have a knock-out of osteoblast cells) and have found that, during a 2 week treatment of the mice with diphtheria toxic to kill osteoblasts, mice are significantly smaller than their normal counterparts (Figure 12) and show alterations in their bone marrow hematopoetic cellular components. Specifically, we saw an increase in the numbers of T-cells in the bone marrow immediately after the 2 week diphtheria toxic treatment period (Figure 13), as well as some other interesting immune changes that we are currently pursuing more deeply.

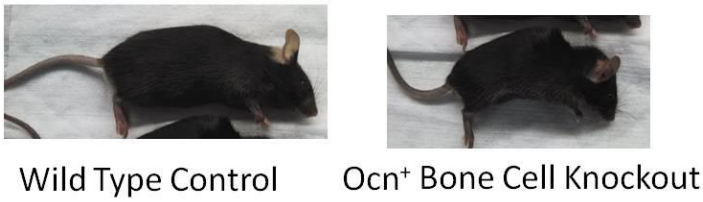

Figure 12: Representative Images of Osteocalcin-Cre +/-;DTR+/- bone knockout mouse (left) compared to wildtype show decreased weight and smaller total volumes in KO mice, as well as a more hunched in posture.

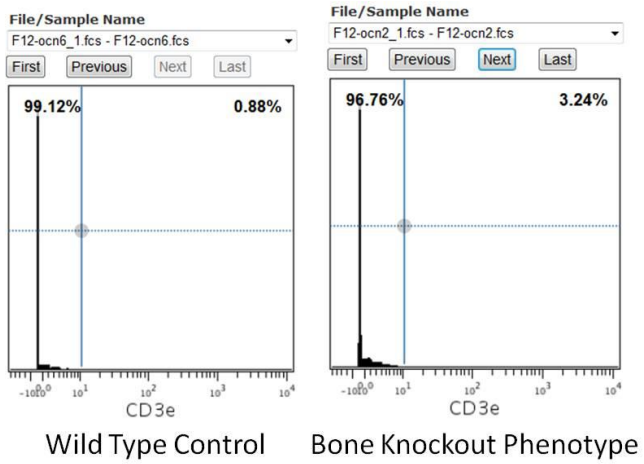

Figure 13: Representative CyTof bone marrow analysis of T-cell populations in Wild Type control mice (left) and Ocn+ Bone Cell Knockout mice (right)

We are now collaborating with many labs on this project, including the lab of Dr. Cliff Rosen in the Maine Medical Center Research Institute (MMCRI). Working with Dr. Rosen, I will continue this work at the end of my post-doc position in September 2015 and will begin as a PI of my own lab at MMCRI. This grant has played a large role in propelling my research and allowing for my transition to the Associate Professor Level in Maine.

Data produced from this grant can be found in the 2 publications in Appendix I. These are:

1. Swami A & Reagan MR*, Basto P, Mishima Y, Kamaly N, Glavey S, Zhang S, Moschetta M, Seevaratnam D; Zhang Y, Liu J, Memarzadeh T, Wu J, Manier S, Shi J, Bertrand N, Lu ZN, Nagano K, Baron R, Sacco A, Roccaro AM, Farokhzad OC, Ghobrial IM. 2014. Engineered Nanomedicine for Myeloma and Bone Microenvironment Targeting. *PNAS;*111(28):10287-922014. **Co-first authorship.*

2. Reagan MR, Mishima Y, Glavey S, Zhang Y, Manier S, Lu ZN, Memarzadeh M, Zhang Y, Sacco A, Aljawai Y, Tai Y-T, Ready JE, Shi J, Kaplan DL, Roccaro AM, Ghobrial IM. Investigating osteogenic differentiation in Multiple Myeloma using a novel 3D bone marrow niche model. *Blood 2014*.

Developed the *in vitro* 3D Model of osteoprogenitors and multiple myeloma cells

Examined the roles of microRNAs in osteogenesis and identified some novel miRs to target for the inhibition of osteolysis.

Developed *in vivo* model of inhibited osteogenesis using OcnCre;DTRmut transgenic mice
Began evaluation of how this model responds to Vk*Myc multiple myeloma cells

Built on work described to study the potential for targeting the bone marrow, rather than the MM cells directly, to have an anti-cancer effect on multiple myeloma, as published in Blood, Sept 2014, shown below. Developed a collaboration around this work that led to a PNAS paper showing efficacy of bortezomib on the bone microenvironment (increased strength, size) and subsequent inhibition of tumor burden.

Conclusions

Our new preclinical bone cancer model has the capacity to support long-term culture and imaging for expansion of primary myeloma cells; high-throughput drug screening; vessel formation; and osteogenesis in the presence of cancer. Our 3D model uses silk protein-based scaffolds that allow for active cell attachment and adherence to scaffolds, rather than a passive encapsulation in 3D hydrogel cultures. In addition, the tissue-engineering approach represents a more controllable model compared to culturing whole patient bone biopsies[6], as it allows for user-designed introduction of cells of interest, increasing the reproducibility, adaptability, and scalability of the model. The system was used to identify miR-199a as partially responsible for decreased osteogenesis observed in Myeloma patient osteoprogenitors. Although the exact composition and interaction of mRNAs inhibited by miR-199a appears complex, it is clear that miR-199a represents the first abnormally expressed miRNAs in bone cancer patients that may be a therapeutic strategy for enhancing bone formation.

Reportable Outcomes
Publications, Abstracts and Presentations

Peer-Reviewed Scientific Journals:

Swami A & Reagan MR*, Basto P, Mishima Y, Kamaly N, Glavey S, Zhang S, Moschetta M, Seevaratnam D; Zhang Y, Liu J, Memarzadeh T, Wu J, Manier S, Shi J, Bertrand N, Lu ZN, Nagano K, Baron R, Sacco A, Roccaro AM, Farokhzad OC, Ghobrial IM. 2014. Engineered Nanomedicine for Myeloma and Bone Microenvironment Targeting. *PNAS;*111(28):10287-922014. **Co-first authorship.*

Reagan MR, Mishima Y, Glavey S, Zhang Y, Manier S, Lu ZN, Memarzadeh M, Zhang Y, Sacco A, Aljawai Y, Tai Y-T, Ready JE, Shi J, Kaplan DL, Roccaro AM, Ghobrial IM. Investigating osteogenic differentiation in Multiple Myeloma using a novel 3D bone marrow niche model. *Blood 2014*.

Oral Presentations/Abstracts:

Invited Speaker and Honorarium Recipient, Center for Clinical & Translational Research, Maine Medical Center Research Institute, May 2014.

Modeling Multiple Myeloma in a Tissue-Engineered Bone Marrow Niche. IBMS: Herbert Fleisch Workshop. March, 2014. Brugge, Belgium.

Nanoparticle Design For Bone-Specific Chemotherapy and Microenvironmental Targeting In Multiple Myeloma. ASH Conference Dec. 10, 2013. New Orleans, Louisiana.

Multiple Myeloma bone marrow derived mesenchymal stem cells (MSCs) show decreased osteogenesis in part due to decreased expression of microRNA hsa-mir-199a-3p, miR-15a-5p and miR-16-5p. IBMS-Cancer and Bone Society Conference, November 7-10, 2013. Miami, Florida.

Poster Presentations/Abstracts (First Authorship):

Modeling Multiple Myeloma in a Tissue-Engineered Bone Marrow Niche. IBMS: Herbert Fleisch Workshop. March, 2014. Brugge, Belgium.

MicroRNA-Dependent Modulation Of Osteogenesis In a 3D In Vitro Bone Marrow Model System Of Multiple Myeloma. ASH Conference Dec. 8, 2013. New Orleans, Louisiana.

Multiple Myeloma bone marrow derived mesenchymal stem cells (MSCs) show decreased osteogenesis in part due to decreased expression of microRNA hsa-mir-199a-3p, miR-15a-5p and miR-16-5p. To be presented at IBMS-CIBD Conference, November 7-10th 2013. Miami, Florida.

Novel Target Identification: Multiple Myeloma bone marrow derived mesenchymal stem cells (MSCs) how decreased osteogenesis in part due to decreased expression of microRNA hsa-mir-199a-3p. Dana-Farber Cancer Institute Post-Doctoral Retreat, September 20, 2013. Cambridge, Massachusetts.

Opportunities for Training and Professional Development

Honors and Conference/Committee Participation based on or involving this work:

Abstract Submission, Dana-Farber Cancer Institute Post-Doctoral Retreat. September 2014.

Application to Maine Medical Center, Portland Maine, for position as assistant professor.

CURE (Continuing Umbrella of Research Experiences) Mentor, Summer 2014.

Invited Speaker, Maine Medical Center Research Institute, June 2014.

Guest Speaker, Boston University High School Summer Education Program, Calculus Class July 2014.

Scientific Committee Member of joint ECTS (European Calcified Tissue Society)- CABS (Cancer and Bone Society)-IBMS Conference in Rotterdam, Netherlands. April 2015.

Conference Session Chair: IBMS Herbert Fleisch Workshop, Brugge, Belgium 2014 and Cancer and Bone Society Meeting, Miami, FL 2013.

IBMS Young Investigator Committee Member (2012-2014), Committee Co-chair (2013-2015).

Herbert Fleisch Workshop Abstract Travel Award 2014.

Best Poster Award, Dana-Farber Cancer Institute Post-Doctoral Retreat. Cambridge, MA. 9/30/2013.

References:

Azab, A. K., Quang, P., Azab, F., Pitsillides, C., Thompson, B., Chonghaile, T., … Ghobrial, I. M. (2012). P-selectin glycoprotein ligand regulates the interaction of multiple myeloma cells with the bone marrow microenvironment. *Blood*, *119*(6), 1468–78. doi:10.1182/blood-2011-07-368050

Fuhler, G. M., Baanstra, M., Chesik, D., Somasundaram, R., Seckinger, A., Hose, D., … Bos, N. A. (2010). Bone marrow stromal cell interaction reduces syndecan-1 expression and induces kinomic changes in myeloma cells. *Experimental Cell Research*, *316*(11), 1816–28. doi:10.1016/j.yexcr.2010.03.013

Markovina, S., Callander, N. S., O'Connor, S. L., Xu, G., Shi, Y., Leith, C. P., … Miyamoto, S. (2010). Bone marrow stromal cells from multiple myeloma patients uniquely induce bortezomib resistant NF-kappaB activity in myeloma cells. *Molecular Cancer*, *9*, 176. doi:10.1186/1476-4598-9-176

Reagan, M. R., & Ghobrial, I. M. (2012). Multiple Myeloma-Mesenchymal Stem Cells: Characterization, Origin, and Tumor-Promoting Effects. *Clinical Cancer Research : An Official Journal of the American Association for Cancer Research*, *18*(2), 342–9. doi:10.1158/1078-0432.CCR-11-2212

Roodman, G. D. (2004). Mechanisms of bone metastasis. *The New England Journal of Medicine, 350*(16), 1655–64. doi:10.1056/NEJMra030831

Yaccoby, S., Wezeman, M. J., Zangari, M., Walker, R., Cottler-Fox, M., Gaddy, D., … Epstein, J. (2006). Inhibitory effects of osteoblasts and increased bone formation on myeloma in novel culture systems and a myelomatous mouse model. *Haematologica, 91*(2), 192–9. Retrieved from http://www.pubmedcentral.nih.gov/articlerender.fcgi?artid=1592551&tool=pmcentrez&rendertype=abstract

Appendix I: Full Journal articles (2)

1. Swami A & Reagan MR*, Basto P, Mishima Y, Kamaly N, Glavey S, Zhang S, Moschetta M, Seevaratnam D; Zhang Y, Liu J, Memarzadeh T, Wu J, Manier S, Shi J, Bertrand N, Lu ZN, Nagano K, Baron R, Sacco A, Roccaro AM, Farokhzad OC, Ghobrial IM. 2014. Engineered Nanomedicine for Myeloma and Bone Microenvironment Targeting. *PNAS;*111(28):10287-922014. **Co-first authorship.*

2. Reagan MR, Mishima Y, Glavey S, Zhang Y, Manier S, Lu ZN, Memarzadeh M, Zhang Y, Sacco A, Aljawai Y, Tai Y-T, Ready JE, Shi J, Kaplan DL, Roccaro AM, Ghobrial IM. Investigating osteogenic differentiation in Multiple Myeloma using a novel 3D bone marrow niche model. *Blood 2014*.

Engineered nanomedicine for myeloma and bone microenvironment targeting

Archana Swami[a,1], Michaela R. Reagan[b,1], Pamela Basto[c], Yuji Mishima[b], Nazila Kamaly[a], Siobhan Glavey[b], Sufeng Zhang[c], Michele Moschetta[b], Dushanth Seevaratnam[a], Yong Zhang[b], Jinhe Liu[a], Masoumeh Memarzadeh[b], Jun Wu[a], Salomon Manier[b], Jinjun Shi[a], Nicolas Bertrand[c], Zhi Ning Lu[b], Kenichi Nagano[d], Roland Baron[d], Antonio Sacco[b], Aldo M. Roccaro[b], Omid C. Farokhzad[a,e,2], and Irene M. Ghobrial[b,2]

[a]Laboratory of Nanomedicine and Biomaterials, Department of Anesthesiology, Brigham and Women's Hospital, Harvard Medical School, Boston, MA 02115; [b]Department of Medical Oncology, Dana-Farber Cancer Institute, Harvard Medical School, Boston, MA 02115; [c]The David H. Koch Institute for Integrative Cancer Research, Massachusetts Institute of Technology, Cambridge, MA 02139; [d]Department of Oral Medicine, Infection and Immunity, Harvard School of Dental Medicine, Harvard Medical School, Boston, MA 02115; and [e]King Abdulaziz University, Jeddah, Saudi Arabia

Edited by Robert Langer, Massachusetts Institute of Technology, Cambridge, MA, and approved May 30, 2014 (received for review January 21, 2014)

Bone is a favorable microenvironment for tumor growth and a frequent destination for metastatic cancer cells. Targeting cancers within the bone marrow remains a crucial oncologic challenge due to issues of drug availability and microenvironment-induced resistance. Herein, we engineered bone-homing polymeric nanoparticles (NPs) for spatiotemporally controlled delivery of therapeutics to bone, which diminish off-target effects and increase local drug concentrations. The NPs consist of poly(D,L-lactic-co-glycolic acid) (PLGA), polyethylene glycol (PEG), and bisphosphonate (or alendronate, a targeting ligand). The engineered NPs were formulated by blending varying ratios of the synthesized polymers: PLGA-*b*-PEG and alendronate-conjugated polymer PLGA-*b*-PEG-Ald, which ensured long circulation and targeting capabilities, respectively. The bone-binding ability of Ald-PEG-PLGA NPs was investigated by hydroxyapatite binding assays and ex vivo imaging of adherence to bone fragments. In vivo biodistribution of fluorescently labeled NPs showed higher retention, accumulation, and bone homing of targeted Ald-PEG-PLGA NPs, compared with nontargeted PEG-PLGA NPs. A library of bortezomib-loaded NPs (bone-targeted Ald-Bort-NPs and nontargeted Bort-NPs) were developed and screened for optimal physiochemical properties, drug loading, and release profiles. Ald-Bort-NPs were tested for efficacy in mouse models of multiple myeloma (MM). Results demonstrated significantly enhanced survival and decreased tumor burden in mice pretreated with Ald-Bort-NPs versus Ald-Empty-NPs (no drug) or the free drug. We also observed that bortezomib, as a pretreatment regimen, modified the bone microenvironment and enhanced bone strength and volume. Our findings suggest that NP-based anticancer therapies with bone-targeting specificity comprise a clinically relevant method of drug delivery that can inhibit tumor progression in MM.

targeting nanomedicine | alendronate-PLGA-PEG | bone metastasis | bisphosphonate

The incidence of bone metastasis is common in 60–80% of cancer patients (1). During bone metastasis, cancer cells induce a sequence of changes in the microenvironment such as secreting cytokines to increase the activity of osteoclasts via the parathyroid hormone-related protein (PTHrP), receptor activator of nuclear factor-κB ligand (RANKL), and interleukin-6 (IL-6), resulting in increased bone resorption and secretion of growth factors from the bone matrix (2). This creates a "vicious cycle" of bone metastasis, where bone marrow becomes packed with cancer cells that develop resistance to conventional chemotherapy, and leads to devastating consequences of bone fractures, pain, hypercalcaemia, and spinal cord and nerve compression syndromes (2, 3). Multiple myeloma (MM) is a plasma cell cancer that proliferates primarily in bone marrow and causes osteolytic lesions (1). Antiresorption agents, such as bisphosphonates, may alleviate bone pain, but they are ineffective at inducing bone healing or osteogenesis in MM patients (4).Bortezomib is a proteasome inhibitor that has shown marked antitumor effects in patients with MM. Proteasome inhibitors, such as bortezomib, are also effective at increasing bone formation, both preclinically and clinically (5–9). However, the major drawback of bortezomib use in early stages of MM development is its toxicity, specifically, peripheral neuropathy (5). Therefore, we aimed to develop a method to deliver bortezomib with decreased off-target side effects by using bone-specific, bortezomib-loaded nanoparticles (NPs). The NP system was based on biodegradable, biocompatible, and Food and Drug Administration (FDA)-approved components, which are both clinically and translationally relevant. NPs derived from poly(D,L-lactic-co-glycolic acid) (PLGA), a controlled release polymer system, are an excellent choice because their safety in the clinic is well established (10, 11). Polyethylene glycol (PEG)-functionalized

Significance

Limited treatment options exist for cancer within the bone, as demonstrated by the inevitable, pernicious course of metastatic breast, prostate, and blood cancers. The difficulty of eliminating bone-residing cancer necessitates novel, alternative treatments to manipulate the tumor cells and their microenvironment, with minimal off-target effects. To this end, we engineered bone-homing, stealth nanoparticles to deliver anticancer, bone-stimulatory drugs, and demonstrated their utility with bortezomib (a model drug) and multiple myeloma (a model cancer). To test our hypothesis that increasing bone volume and strength inhibits tumor growth, mice were treated with these nanoparticles before being injected with cancer cells. Results demonstrated significantly slower myeloma growth and prolonged survival. Our research demonstrates the potential of bone-homing nanomedicine as an efficacious cancer treatment mechanism.

Author contributions: A. Swami, M.R.R., O.C.F., and I.M.G. designed research; A. Swami, M.R.R., P.B., Y.M., N.K., S.G., S.Z., M. Moschetta, D.S., Y.Z., J.L., M. Memarzadeh, J.W., S.M., J.S., N.B., Z.N.L., K.N., R.B., A. Sacco, and A.M.R. performed research; A. Swami, M.R.R., R.B., A.M.R., O.C.F., and I.M.G. analyzed data; and A. Swami, M.R.R., P.B., N.K., O.C.F., and I.M.G. wrote the paper.

Conflict of interest statement: I.M.G. discloses her Advisory Board Membership with Novartis, Onyx, and BMS. O.C.F. discloses his financial interest in BIND Therapeutics, Selecta Biosciences, and Blend Therapeutics, three biotechnology companies developing nanoparticle technologies for medical applications. BIND, Selecta, and Blend did not support the aforementioned research, and currently these companies have no rights to any technology or intellectual property developed as part of this research.

This article is a PNAS Direct Submission.

Freely available online through the PNAS open access option.

[1]A.S. and M.R.R. contributed equally to this work.

[2]To whom correspondence may be addressed. Email: ofarokhzad@zeus.bwh.harvard.edu or irene_ghobrial@dfci.harvard.edu.

This article contains supporting information online at www.pnas.org/lookup/suppl/doi:10.1073/pnas.1401337111/-/DCSupplemental.

PLGA NPs are especially desirable as PEGylated polymeric NPs have significantly reduced systemic clearance compared with similar particles without PEG (12, 13). A number of FDA-approved drugs in clinical practice use PEG for improved pharmaceutical properties such as enhanced circulation in vivo (12, 13). To target NPs to bone [rich in the mineral hydroxyapatite (HA)], the calcium ion-chelating molecules of bisphosphonates represent a promising class of ligands (14). Bisphosphonates, upon systemic administration, are found to deposit in bone tissue, preferentially at the high bone turnover sites, such as the metastatic bone lesions, with minimal nonspecific accumulation (14) and were used herein to deliver NPs to the bone.

A few systems explored for MM treatment have been tested in vitro including the following: (*i*) snake venom and silica NPs (15); (*ii*) thymoquinone and PLGA-based particles (16); (*iii*) curcumin and poly(oxyethylene) cholesteryl ether (PEG-Chol) NPs (17), polyethylenimine-based NPs for RNAi in MM (18), paclitaxel-Fe_3O_4 NPs (19), and liposomes (20). However, none of the above-mentioned systems have aimed to manipulate the bone marrow microenvironment rather than the myeloma cells directly (21). To date, there are no reports of using bone-targeted, controlled release, polymeric NPs with stealth properties for MM therapy. In this study, we designed NPs bearing three main components: (*i*) a targeting element that can selectively bind to bone mineral; (*ii*) a layer of stealth (PEG) to minimize immune recognition and enhance circulation; and (*iii*) a biodegradable polymeric material, forming an inner core, that can deliver therapeutics and/or diagnostics in a controlled manner. In this study, the physicochemical properties of a range of NPs was investigated (including NP size, charge, targeting ligand density, drug loading, and drug release kinetics) and an optimal formulation with ideal properties and maximal drug encapsulation was used for in vivo efficacy studies. We fine-tuned the NP targeting ligand density to optimize its bone-binding ability and further investigated its application for targeting myeloma in the bone microenvironment. We believe our NP system has the potential to increase drug availability by improving pharmacokinetics and biodistribution that can provide bone microenvironment specificity, which may increase the therapeutic window and most certainly decrease the off-target effects (12, 13).

Results and Discussion

Design, Synthesis, and Characterization of Alendronate-PEG-PLGA NPs. The design and synthesis of alendronate-PEG-PLGA (Ald-PP), bone-targeted NPs engineered with fine-tuned Ald density on their surface, and nontargeted PEG-PLGA (PP) NPs, are shown in Fig. 1 *A* and *B* and Fig. S1. The physicochemical characteristics and bortezomib drug load of the NPs (Fig. 1 *C* and *D*) were optimized by analyzing a library of NPs formulated (Fig. S2) with varying parameters such as the following: formulation technique, polymer molecular weight, polymer concentration, ratio of organic to aqueous phase, formulation condition, and initial drug feed (Fig. 1*D* and Fig. S2 *C*–*E*). The lead candidate NPs synthesized by single-emulsion method of formulation had optimal sizes in the range of 150–200 nm and nearly neutral to slightly negative ζ potentials (Fig. 1 *C* and *D*, and Fig. S2*C*), and were further standardized to enhance their drug load. To obtain optimal binding to the bone mineral along with maximum stealth properties, we blended varying ratios of the polymers: PLGA-*b*-PEG-Ald (Fig. S1) and PLGA-*b*-PEG for NP formulation (Fig. 1 *A*, *B*, *E*, and *F*). Different ratios of blended polymers altered the Ald content of NPs. We analyzed the stability and size of these NPs in the presence of ions and serum conditions, and the results demonstrated time-dependent increase in NP size, when the content of PLGA-*b*-PEG-Ald polymer in the NPs was higher than 20% (Fig. 1*F*). Thus, it is important to optimize the Ald content of NPs for effective bone binding with maintenance of stealth properties, which ensures enhanced bone homing of NPs, in vivo.

Encapsulation and Release of Bortezomib from NPs. The ability of the NPs to encapsulate high loads of drug and subsequently release the drug in a controlled manner was significantly affected by PLGA molecular weight and content in the NPs, in addition to the formulation techniques and conditions, as investigated by using HPLC. In the case of NPs formulated by the solvent dispersion method, the hydrodynamic diameter (dynamic light

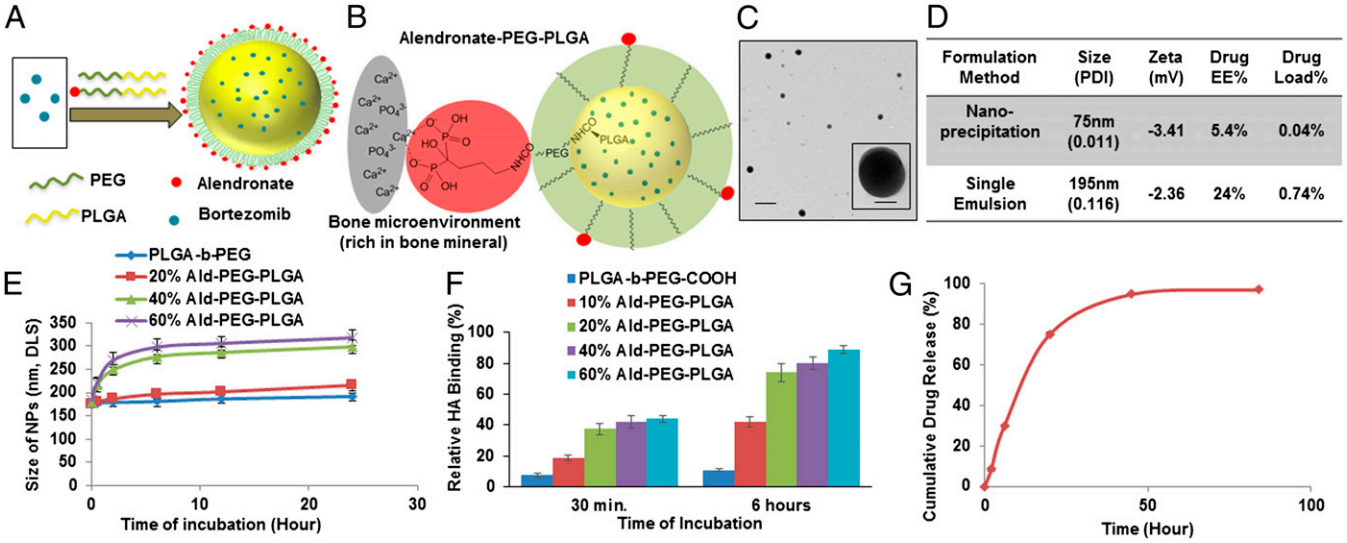

Fig. 1. Design, engineering, and characterization of NPs for bone targeting. (*A*) Schematic illustration of alendronate-conjugated PEG-PLGA (Ald-PP) NPs synthesized by blending polymers (PLGA-*b*-PEG-Ald and PLGA-*b*-PEG) in varying ratios and encapsulating the drug bortezomib. (*B*) Schematic representation of the mechanism of affinity of Ald-PP NPs with bone mineral (gray, bone mineral; red, Ald; green, PEG; yellow, PLGA). (*C*) Representative TEM image of Ald-PP NPs (single emulsion), negatively stained, imaged at 80.0 kV. (Scale bars: 500 nm; *Inset*, 100 nm.) (*D*) Physiochemical characteristics of Ald-PP NPs. (*E*) Size of the Ald-PP NPs (single emulsion) with varying content of polymer PLGA-*b*-PEG-Ald, in presence of serum, with time. (*F*) Quantitative evaluation of HA binding of NPs (single emulsion) with varying content of PLGA-*b*-PEG-Ald polymer. PLGA-*b*-PEG (-COOH terminated) polymeric NPs were used as control. (*G*) Release kinetics of encapsulated drug bortezomib from the Ald-PP NPs (single emulsion), in physiological ionic and temperature conditions.

scattering) was small (80–100 nm), with lower encapsulation efficiency (5–8%) along with lower drug loading (0.04–0.09%). In the case of the single-emulsion NPs with optimal polymer weight (M_r, 45 kDa) and formulation conditions, the NP drug load was enhanced 16- to 20-fold and the release kinetics showed sustained drug release (Fig. 1 *D* and *G*, and Fig. S2 *B*, *D*, and *E*). This can be attributed to the dispersion of the encapsulated drug from the PLGA core of NP by diffusion and polymer degradation. The NPs protect the drug from the external environment, and increase its blood circulation time, thereby increasing the drug content at the target site.

In Vitro Bone Targeting of NPs. Bone microenvironment is rich in HA, particularly the sites of metastatic lesions, where the bone turnover is high, and to investigate the bone affinity of the Ald-PP NPs (single emulsion), we performed the HA binding assay (Fig. 1*F*), in comparison with nontargeted PP NPs (Fig. 2*A*). The Ald-PP NP solution on incubation with HA in any form (NPs, microparticles, or bone chips) showed immediate binding (Figs. 1*F* and 2 *B*–*D*). The results demonstrated a significant rise in the HA binding of NPs as the content of PLGA-*b*-PEG-Ald polymer in the NPs was increased from 0% to 20%. This trend plateaued on further increase of PLGA-*b*-PEG-Ald polymer content in NPs to 40% or 60% (Fig. 1*F*). Thus, optimized, targeted Ald-PP NPs with effective HA binding had 20% PLGA-*b*-PEG-Ald polymer, for all studies thereafter. The HA affinity of targeted NPs was also confirmed by the following: transmission electron microscopy (TEM) using HA in NP form (Fig. 2*B*); scanning electron microscopy (SEM) using HA generated from simulated body fluid (Fig. 2*C*); and fluorescence microscopy using bone fragments (mice skull bone, ex vivo) with fluorescently labeled NPs (Fig. 2*D*). Nontargeted PP NPs did not show any specificity or binding to HA, in any form (Fig. 2 *B*–*D*). These results confirmed the impact of the design of our engineered targeted NPs in bone mineral binding and the differential binding of targeted NPs facilitated the next in vivo experiments.

In Vivo Biodistribution Studies of NPs. The bone-homing ability of targeted Ald-PP NPs (single emulsion) was investigated by conducting biodistribution studies using fluorescently labeled NPs (PLGA-Alexa$_{647}$) tracked with an in vivo imaging system (IVIS) in mice (Fig. 2 *E* and *F*), after i.p. injection. At 24 h, mice injected with targeted NPs showed increased retention in areas of the spleen, femur, spin, skull, and lymph nodes (Fig. 2*E*). The higher retention of targeted NPs compared with nontargeted NPs was confirmed by quantifying the total radiance efficiency of the mice body image (Fig. 2 *G* and *H*). For further examination of the retention and bone-homing ability of targeted NPs, the dissected femur and spine of the mice were sectioned, counterstained with DAPI, and imaged with a fluorescence microscope. Quantification of the NP in bone sections, as measured by the fluorescence (Alexa$_{647}$), revealed 9.6-fold increased accumulation of targeted NPs compared with nontargeted NPs (Fig. 2 *F* and *H*, and Fig. S3). Thus, in vivo biodistribution and histology studies complement the in vitro and ex vivo bone-binding results, which highlight the potential of our engineered NPs for targeting bone.

In Vitro Uptake and Efficacy Studies of NPs in Myeloma Cells. Cellular uptake and accumulation of fluorescently labeled Ald-PP and PP NPs (single emulsion) were quantified using flow cytometry, and demonstrated uptake by peripheral blood mononuclear cells (PBMCs), and to a greater extent by myeloma cells (MM1S) (Fig. 3*A*) with no observable cytotoxic effects. These NPs were also visualized in MM1S cells as demonstrated by using fluorescence microscopy after 24 h of in vitro culture with NPs (Fig. 3*B*). Bortezomib-loaded PP NPs (Bort-NPs) were then assessed for their ability to induce apoptosis and inhibit MM growth in vitro. Apoptosis analysis assessed by Annexin-V/propidium iodide (PI)

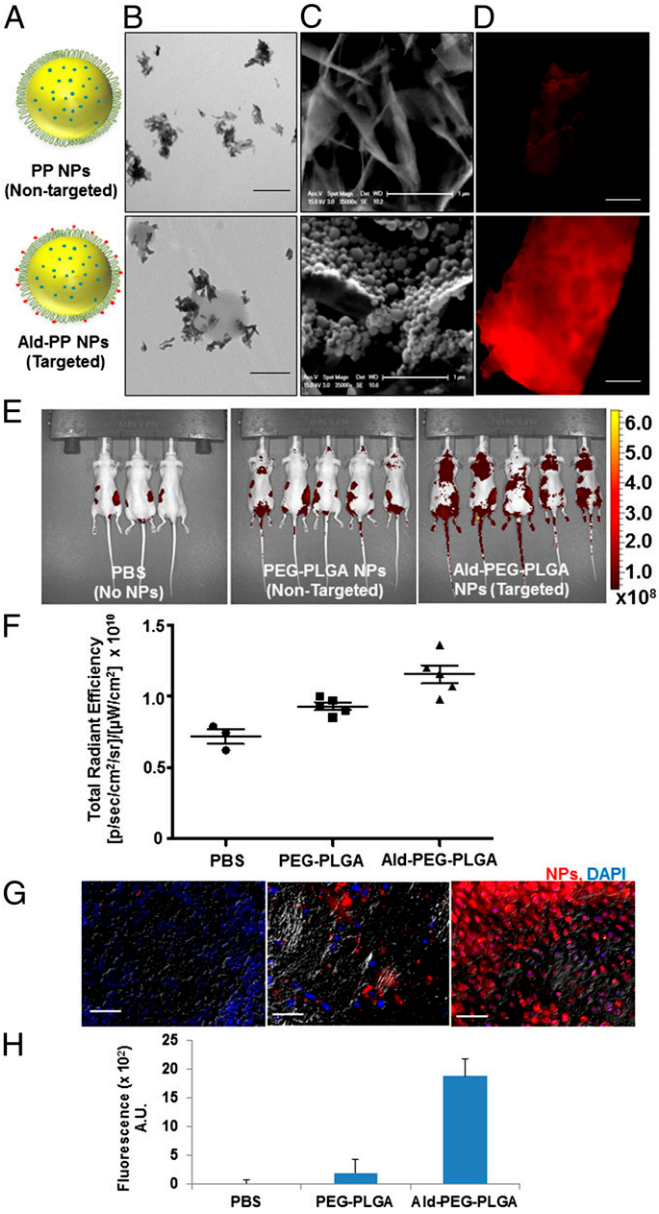

Fig. 2. Bone-targeting ability of Ald-PP NPs (single emulsion). (*A*) Schematic illustration of bone-targeted Ald-PP NPs and nontargeted PP NPs. (*B*) Representative TEM image of Ald-PP (*Lower*) NPs surface interactions with HA rods, which is not observed in case of nontargeted PP NPs (*Upper*). (Scale bar: 500 nm.) (*C*) Representative SEM image of interaction of NPs (targeted Ald-PP: *Lower*; nontargeted PP: *Upper*) with crystalized HA (scale bar: 1 μm) after incubation with NP solution and washing. (*D*) Representative fluorescence image of bone fragment after incubation with fluorescently labeled NP solution (targeted Ald-PP: *Lower*; nontargeted PP: *Upper*) (ex vivo), and washing. (Scale bar: 500 μm.) (*E*) Whole-body mice imaging (IVIS), where targeted NP (*Right*) clearance is compared with nontargeted NPs (*Center*) and PBS (*Left*) (24-h time point, i.p. injection). Scale represents luminescence signal from Alexa$_{647}$-labeled NPs, representing NP biodistribution. (*F*) Total fluorescence quantified in the region of interest of IVIS images from *E*. (*G*) Representative images of bone histology in merged channels (405: DAPI; 647: NPs; and bright field) for PBS (*Left*), nontargeted NPs (*Center*), and targeted NPs (*Right*). (Scale bar: 100 μm.) (*H*) Quantification of NP homing as measured from the bone (femur and spine) histology by fluorescence intensity (average) quantification in the 647 channel in multiple sections of bone, covering entire region representatively, in different mice (n = 3).

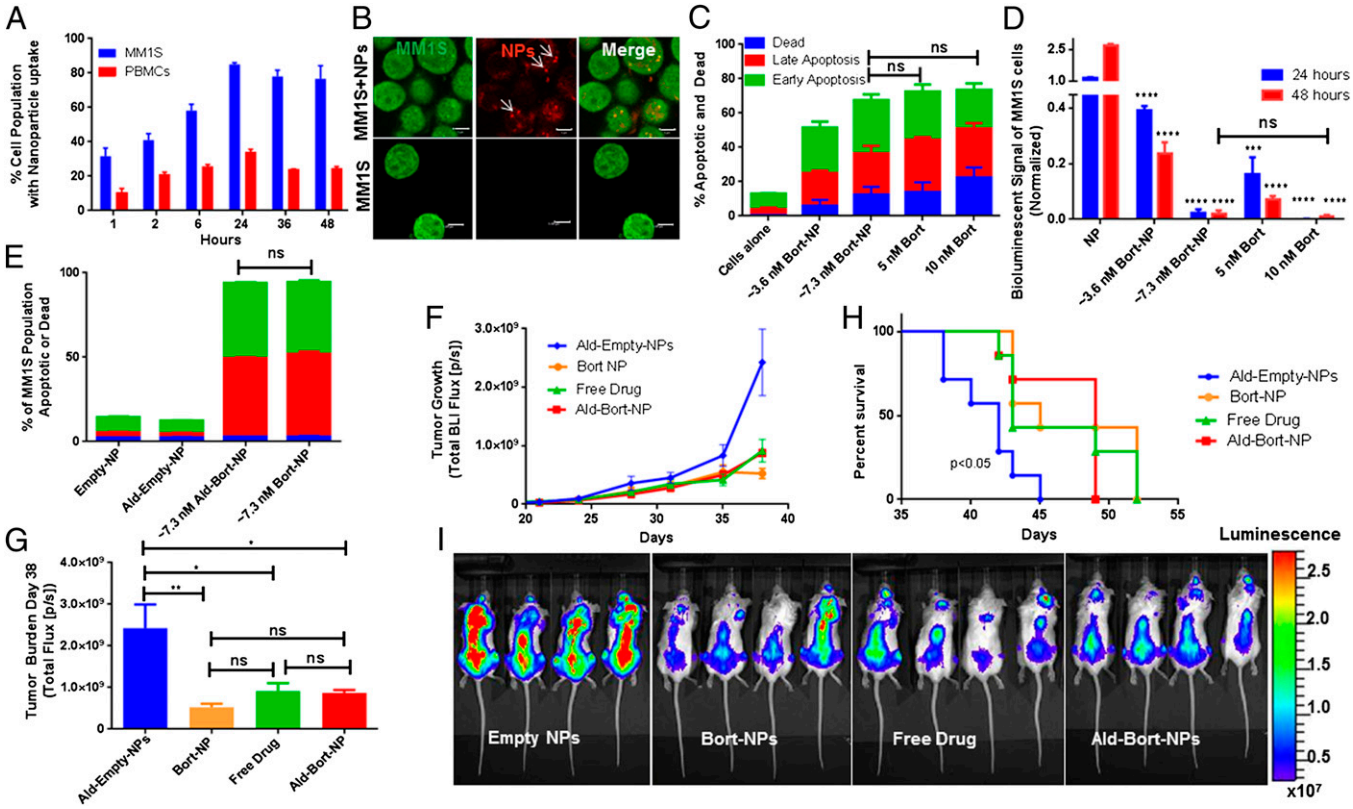

Fig. 3. In vitro and in vivo efficacy of NPs (single emulsion). (*A*) Cellular uptake of NPs during coculture with myeloma (MM1S) cells and peripheral blood mononuclear cells (PBMCs). (*B*) $Alexa_{647}$-labeled NPs imaged in GFP^+ MM1S cells using fluorescence confocal imaging. Bort-NPs induced apoptosis and death in MM1S cells (24 h) (scale bar: 5 μm) (*C*) as measured by Annexin-V/PI flow cytometry; and (*D*) bioluminescent signal quantification of GFP^+Luc^+ MM1S cells (24, 48 h). In *C* and *D*, cells were treated with effective bortezomib concentrations of ∼3.6 or ∼7.3 nM (Bort-NPs) or free drug (5 or 10 nM). *T* tests evaluating efficacy of treatments vs. NP controls at same time point show equivalent efficacy of 7.3 nM Bort-NPs and 10 nM Free Drug. (*E*) Annexin-V/PI flow cytometry of GFP^+ MM1S cells treated with Empty-NPs, Ald-Empty-NPs, ∼3.6 nM Ald-Bort-NPs, and ∼7.3 nM Bort-NPs after 24 h. The stacked bars represent means ± SEM. (*F–I*) Mice injected with GFP^+Luc^+ MM1S cells, treated with Ald-Empty-NPs, Bort-NPs, Free Drug, and Ald-Bort-NPs twice a week, starting at day 21 after tumor cell injection ($n = 7$). (*F*) BLI flux measuring tumor burden in mice from day 21 to 38. (*G*) Quantification of BLI at day 38. (*H*) Survival data for mice treated with Bort-NPs, Ald-Bort-NPs, Free Drug, or NP controls. (*I*) Representative BLI images of mice at day 38 from the four groups. Scale represents luminescence signal from Luc^+ MM1S cells, quantifying tumor burden.

staining and flow cytometry showed similar induction of apoptosis of MM1S cells at 24 h using bortezomib-loaded NPs or free drug (Fig. 3*C*). Bioluminescent quantification of cell numbers also demonstrated similar in vitro bortezomib efficacies when delivered in NPs or as a free drug, with no significant difference found between 7.3 nM Bort-NPs and 10 nM free drug at 48 h. All treatments significantly decreased MM1S cell numbers at all time points. These results illustrate the ability for NPs to effectively deliver bortezomib to inhibit myeloma growth in vitro (Fig. 3*D*). The addition of Ald did not change the efficacy of Bort-NPs in inducing apoptosis, and both drug-free PP and Ald-PP NPs were nontoxic, as expected (Fig. 3*E*) (10, 11).

NPs Inhibit MM Growth in Vivo. In the next set of experiments, we used a MM1S xenograft osteolytic bone disease model (22) where GFP^+Luc^+ MM1S cells were injected into the tail vein of SCID-beige mice, treated with NPs and controls, and measured for tumor burden using bioluminescent imaging (BLI) and survival. MM1S tumor burden was significantly decreased by Ald-Bort-NPs, Bort-NPs (Ald free), and Free Drug compared with Ald-Empty-NPs (no-drug Ald-PP NPs) at day 38 (Fig. 3 *F* and *G*). These data indicate that Ald-Bort-NPs and Bort-NPs were able to reduce tumor burden to the same extent as Free Drug. There was also a significant increase in the survival for mice treated with Ald-Bort-NPs, Bort-NPs, and Free Drug, compared with Ald-Empty-NPs (Fig. 3 *H* and *I*). This evidence demonstrates that bortezomib delivery with NPs works as well as conventional, free drug delivery, in the mice model.

In the treatment study of established myeloma, we believe cancer inhibition was not observed with the use of NPs because, in mice, much of the disease develops outside of the bone marrow niche (circulating and lodged in extramedullary/nonbone locations), which is one of the major differences between mouse myeloma models and the clinical presentation, making inhibition by bortezomib equally efficacious when delivered by any of the compared methods. Conversely, in patients, MM growth is more bone-restricted and treatment with bone-targeting NPs could potentially show increased efficacy vs. free drug or non–bone-targeted NPs by increasing the therapeutic window specifically in the location of the highest MM cell concentration. Furthermore, although we are unable to model peripheral neuropathy in mice due to inherent neurological differences in mice and humans, bone-targeted NPs may potentially improve patient outcomes by decreasing neuropathy from off-target effects of bortezomib.

Bortezomib Increases Osteogenic Differentiation in Vitro and in Vivo. After validating the ability for bortezomib to increase osteogenic differentiation of bone marrow-derived mesenchymal stromal cells (MSCs) in vitro (Fig. S4), we assessed the effects of bortezomib in vivo. Mice were pretreated with Ald-Empty-NPs, Free Drug, or Ald-Bort-NPs for 3 wk, thrice a week, and euthanized thereafter. Bones were analyzed with micro-computed tomography (micro-CT) analysis of femur and tibia, and static bone histomorphometry of the tibia. We observed significantly increased bone trabecular volume, as demonstrated in Von Kossa-stained tibia slides (Fig. 4*A*),

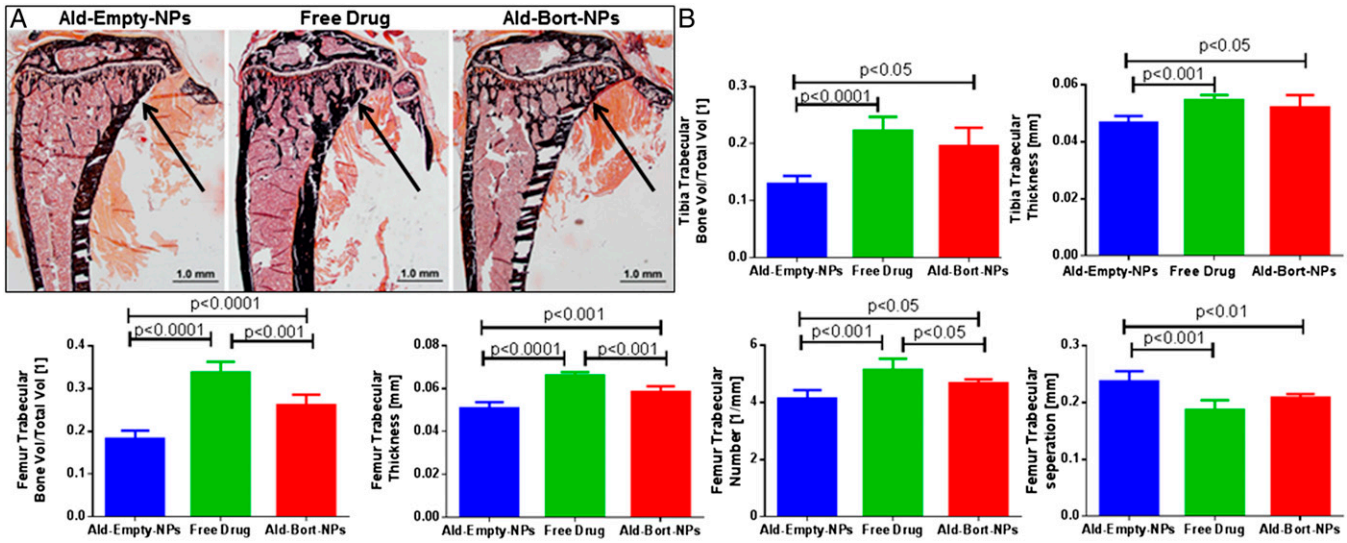

Fig. 4. In vivo effects of bortezomib NPs (single emulsion) on bones. Mice were pretreated for 3 wk, with Ald-Empty-NPs, Free Drug, or Ald-Bort-NPs. Static bone histomorphometry and micro-CT done on these samples show an increase in bone formation markers for the bortezomib-treated groups. (*A*) Representative images from static histomorphomety from each group shown by Von Kossa staining. Trabecular bone volume was increased in Free Drug and Ald-Bort-NP groups compared with that of Ald-Empty-NP group, as indicated by arrows. (*B*) Micro-CT analysis demonstrated significantly higher bone in Ald-Bort-NPs and Free Drug compared with that of Ald-Empty-NPs in terms of the following: tibia trabecular bone volume per total volume, tibia trabecular thickness, femur trabecular bone volume per total volume, femur trabecular thickness, femur trabecular number, and femur trabecular separation.

and quantified with micro-CT in the tibia and femur and histomorphometry of the proximal tibia (Fig. 4*B*). Histomorphometric analysis also demonstrated significant increases in osteoid thickness and decreases in several bone resorption parameters in mice treated with either Ald-Bort-NPs or Free Bortezomib, vs. Ald-Empty-NPs (Table S1), with both changes (increased osteoblastic activity and decreased osteoclastic activity) contributing to the increased bone volume. Significantly higher bone metrics were also observed in Ald-Bort-NPs and Free Drug compared with Ald-Empty NPs using micro-CT quantification, in terms of tibia trabecular bone volume per total volume, tibia trabecular thickness, and femur trabecular bone volume per total volume, femur trabecular thickness, femur trabecular number, and femur trabecular separation (Fig. 4*B*). This evidence demonstrates the ability for both free bortezomib and bortezomib-loaded NPs to increase volume of bone, and number of trabeculae, in vivo over a 3-wk pretreatment period. We next investigated the consequences of these treatments on the growth of MM.

Pretreatment with Bone-Targeted, Bortezomib NPs Inhibits Myeloma Growth. To examine whether modulating the bone marrow niche before metastasis occurs can prevent/delay disease progression, mice were pretreated with Ald-Bort-NPs, Ald-Empty-NPs, or Free Drug for 3 wk, thrice a week. This allowed for the modulation of the bone microenvironment before the arrival of cancer cells. They were then injected with $GFP^{+}Luc^{+}$ MM1S cells into the tail vein and assessed for tumor progression. Of great importance was our observation that pretreatment with Ald-Bort-NP significantly inhibited myeloma growth as observed with significantly lower BLI signal compared with the Free Drug and Ald-Empty-NP groups ($P < 0.05$) (Fig. 5 *A* and *C*). Survival time was also significantly increased in the Ald-Bort-NP group with median survival of 41 d,

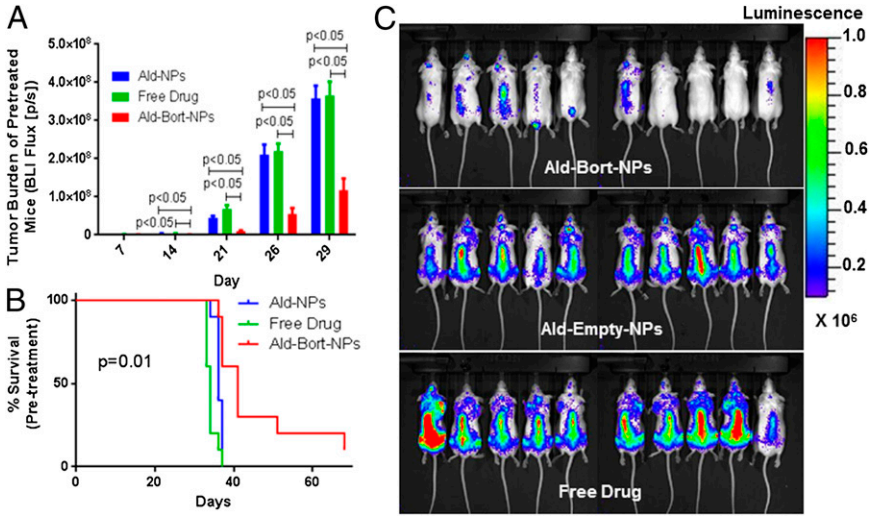

Fig. 5. Pretreatment with Ald-Bort-NPs inhibits myeloma growth better than free drug. (*A*–*C*) Mice were pretreated for 3 wk with Ald-Empty-NPs, Free Drug, or Ald-Bort-NPs and then injected with GFP^{+} Luc^{+} MM1S cells. (*A*) BLI flux from mice was significantly lower in Ald-Bort-NPs compared with that of Ald-Empty-NPs or Free Drug groups at every day of imaging. (*B*) Survival was also significantly increased in the Ald-Bort-NP–pretreated mice ($P = 0.01$). (*C*) Day 29 images of BLI signal from mice illustrates the reduction of tumor burden in mice pretreated with Ald-Bort-NPs ($n = 10$).

compared with just 34 or 36 d in the Free Drug group, and Ald-Empty-NP groups, respectively (Fig. 5*B*). In a second in vivo study (Fig. S5), we confirmed that pretreatment with bone-homing bortezomib NPs improved survival compared with pretreatment with nontargeted bortezomib NPs. Both treatments significantly improved survival compared with empty-NPs, further confirming that bortezomib NP drug delivery creates a less hospitable bone microenvironment for cancer cells. These results suggests that Ald-Bort-NPs may have the ability to alter the microenvironment to prevent myeloma growth via mechanisms other than increasing in bone volume, trabecular number, or osteoid thickness, and should be explored for their ability to inhibit other bone-metastatic cancers.

Conclusion

In summary, we developed, biodegradable polymeric NPs capable of targeting bone and delivering the payload in a spatiotemporally controlled manner. These NPs were shown to enhance bone homing due to long circulation and bone mineral-targeting capabilities. The bone-targeted NPs with sustained release polymer technology delivered bortezomib to bone marrow microenvironment specifically, to produce the antimyeloma effects similar to a free drug. However, the major drawback of using a free drug, bortezomib, is peripheral neuropathy (5), and the use of our NPs would be hugely beneficial by enabling bone-specific drug delivery, which should drastically decrease these side effects in patients. It is also well known that MM resistance is due to cell dormancy within the bone marrow, and the clonal nature of MM, which is driven by a wide range of interactions, constantly evolving mutations, and heterogeneous abnormalities. However, targeting the microenvironment, on the other hand, translates well to all patients, regardless of the driver mutation. Thus, our NPs, which are specifically designed to home to the bone marrow, release the drug to target both the cancer and the microenvironmental cells. Furthermore, the design of our engineered NP has far-reaching advantages of flexibility of NP design, scalability, biocompatibility and biodegradability, long circulation, sustained drug release, bone-homing property, and fine-tuned components for clinical translation. In the future, this platform could be used in many other cancer models to deliver many different anticancer agents. The results of the present work demonstrate the tremendous potential of the bone-targeted Ald-PP NPs in the pretreatment strategy for modifying the bone microenvironment with suitable drugs to prevent cancer progression and lesion formation, providing a promising nanomedicine approach for MM therapy.

Materials and Methods

(See *SI Materials and Methods* for details.) To optimize NP formulation with suitable physicochemical characteristics, with varying ratios of target ligand (Ald) to PEG density on NP surface, and to maximize the drug load, we prepared a library of NPs, using different polymer molecular weights, blending different ratios of synthesized polymers (Figs. S1 and S2) (23), using different formulation techniques, and varying the conditions of formulations. The affinity of Ald-conjugated NPs (Ald-PP) toward bone mineral (HA) was investigated in comparison with nontargeted (PP) NPs. We studied the in vivo biodistribution of $Alexa_{647}$-labeled Ald-PP NPs with whole-mouse imaging. NPs were injected i.p. and after imaging (1, 24 h), the mouse bones were dissected, sectioned, and imaged for investigation of bone homing of labeled NPs (Fig. S3). We investigated the in vitro efficacy of Bort-NPs by measuring apoptosis via flow cytometry, and bioluminescence assay, where empty NPs, and free bortezomib were the controls (24). The in vivo efficacy studies used female Nod/SCID beige mice in treatment or pretreatment regimes. For treatment studies, mice injected with Luc^+/GFP^+ MM1S cells were randomly divided into four groups ($n = 7$). After injecting cancer cells, on day 21 mice were injected (i.p.) twice a week with 0.5 mg/kg bortezomib (or with an equivalent amount of Ald-Empty-NPs): Ald-Empty-NPs, Free Drug (bortezomib), Ald-Bort-NPs, and nontargeted Bort-NPs, and were imaged twice a week. In the case of NP pretreatment regime, female Nod/SCID beige mice were randomized into three groups ($n = 10$) and injected (i.p.) thrice a week for 3 wk, with 0.3 mg/kg bortezomib or with an equivalent amount of Ald-Empty-NPs. The pretreatment groups were as follows: Ald-Bort-NPs, Free Drug, and Ald-Empty-NPs in study 1 and Ald-Bort-NPs, Ald-Empty-NPs, and Nontargeted Bort-NPs in study 2. After 3 wk, the mice were injected with Luc^+GFP^+ MM1S cell. BLI was performed weekly on these mice and survival was assessed. Additionally, an ex vivo micro-CT analysis and static histomorphometry (25) of mouse bones (femur, tibia, and fibula) were performed after a 3-wk pretreatment period to validate bortezomib-induced increase in osteogenesis. See *SI Materials and Methods, Statistical Analysis* for the details of the statistical analysis.

ACKNOWLEDGMENTS. This work was supported by Department of Defense Grant W81XWH-05-1-0390; National Institutes of Health Grants R00 CA160350, R01 FD003743, R01 CA154648, and CA151884; Movember–Prostate Cancer Foundation Challenge Award; National Research Foundation of Korea K1A1A2048701; and the David Koch–Prostate Cancer Foundation Award in Nanotherapeutics. N.B. acknowledges Canadian Institutes of Health Research.

1. Roodman GD (2009) Pathogenesis of myeloma bone disease. *Leukemia* 23(3):435–441.
2. Reagan MR, Ghobrial IM (2012) Multiple myeloma mesenchymal stem cells: Characterization, origin, and tumor-promoting effects. *Clin Cancer Res* 18(2):342–349.
3. Coleman RE (2001) Metastatic bone disease: Clinical features, pathophysiology and treatment strategies. *Cancer Treat Rev* 27(3):165–176.
4. Garrett IR, et al. (2003) Selective inhibitors of the osteoblast proteasome stimulate bone formation in vivo and in vitro. *J Clin Invest* 111(11):1771–1782.
5. Ozaki S, et al. (2007) Therapy with bortezomib plus dexamethasone induces osteoblast activation in responsive patients with multiple myeloma. *Int J Hematol* 86(2): 180–185.
6. Giuliani N, et al. (2007) The proteasome inhibitor bortezomib affects osteoblast differentiation in vitro and in vivo in multiple myeloma patients. *Blood* 110(1):334–338.
7. Heider U, et al. (2006) Bortezomib increases osteoblast activity in myeloma patients irrespective of response to treatment. *Eur J Haematol* 77(3):233–238.
8. Zangari M, et al. (2005) Response to bortezomib is associated to osteoblastic activation in patients with multiple myeloma. *Br J Haematol* 131(1):71–73.
9. Terpos E, et al. (2010) Increased bone mineral density in a subset of patients with relapsed multiple myeloma who received the combination of bortezomib, dexamethasone and zoledronic acid. *Ann Oncol* 21(7):1561–1562.
10. Hrkach J, et al. (2012) Preclinical development and clinical translation of a PSMA-targeted docetaxel nanoparticle with a differentiated pharmacological profile. *Sci Transl Med* 4(128):128ra39.
11. Kamaly N, Xiao Z, Valencia PM, Radovic-Moreno AF, Farokhzad OC (2012) Targeted polymeric therapeutic nanoparticles: Design, development and clinical translation. *Chem Soc Rev* 41(7):2971–3010.
12. Swami A, et al. (2012) *Multifunctional Nanoparticles for Drug Delivery Applications*, eds Svenson S, Prud'homme RK (Springer, Boston), pp 9–29.
13. Zhang X-Q, et al. (2012) Interactions of nanomaterials and biological systems: Implications to personalized nanomedicine. *Adv Drug Deliv Rev* 64(13):1363–1384.
14. Zhang S, Gangal G, Uludağ H (2007) "Magic bullets" for bone diseases: Progress in rational design of bone-seeking medicinal agents. *Chem Soc Rev* 36(3):507–531.
15. Sayed D, Al-Sadoon MK, Badr G (2012) Silica nanoparticles sensitize human multiple myeloma cells to snake (*Walterinnesia aegyptia*) venom-induced apoptosis and growth arrest. *Oxid Med Cell Longev* 2012:386286.
16. Ravindran J, et al. (2010) Thymoquinone poly (lactide-co-glycolide) nanoparticles exhibit enhanced anti-proliferative, anti-inflammatory, and chemosensitization potential. *Biochem Pharmacol* 79(11):1640–1647.
17. Sou K, Oyajobi B, Goins B, Phillips WT, Tsuchida E (2009) Characterization and cytotoxicity of self-organized assemblies of curcumin and amphiphatic poly(ethylene glycol). *J Biomed Nanotechnol* 5(2):202–208.
18. Taylor CA, et al. (2012) Modulation of eIF5A expression using SNS01 nanoparticles inhibits NF-κB activity and tumor growth in murine models of multiple myeloma. *Mol Ther* 20(7):1305–1314.
19. Yang C, et al. (2013) Paclitaxel-Fe_3O_4 nanoparticles inhibit growth of CD138(–) CD34 (–) tumor stem-like cells in multiple myeloma-bearing mice. *Int J Nanomedicine* 8: 1439–1449.
20. Maillard S, et al. (2005) Innovative drug delivery nanosystems improve the anti-tumor activity in vitro and in vivo of anti-estrogens in human breast cancer and multiple myeloma. *J Steroid Biochem Mol Biol* 94(1-3):111–121.
21. Cirstea D, et al. (2010) Dual inhibition of akt/mammalian target of rapamycin pathway by nanoparticle albumin-bound-rapamycin and perifosine induces antitumor activity in multiple myeloma. *Mol Cancer Ther* 9(4):963–975.
22. Azab AK, et al. (2009) CXCR4 inhibitor AMD3100 disrupts the interaction of multiple myeloma cells with the bone marrow microenvironment and enhances their sensitivity to therapy. *Blood* 113(18):4341–4351.
23. Pridgen EM, et al. (2013) Transepithelial transport of fc-targeted nanoparticles by the neonatal fc receptor for oral delivery. *Sci Transl Med* 5(213):213ra167.
24. Leleu X, et al. (2007) The Akt pathway regulates survival and homing in Waldenstrom macroglobulinemia. *Blood* 110(13):4417–4426.
25. Dempster DW, et al. (2013) Standardized nomenclature, symbols, and units for bone histomorphometry: A 2012 update of the report of the ASBMR Histomorphometry Nomenclature Committee. *J Bone Miner Res* 28(1):2–17.

Supporting Information

Swami et al. 10.1073/pnas.1401337111

SI Materials and Methods

Formulation and Characterization of Targeted (Alendronate-PEG-PLGA) Nanoparticles. To optimize nanoparticle (NP) formulation with suitable physicochemical characteristics, with varying ratios of target ligand [alendronate (Ald)] to polyethylene glycol (PEG) density on NP surface, and to maximize the drug load, we prepared a library of NPs. The NP library was designed using different polymer molecular weights, blending different polymer ratios, using different formulation techniques such as nanoprecipitation and emulsions, and varying the conditions of formulations. We further maximized the drug load by optimizing the initial drug feed. The NPs were purified and concentrated. To formulate the NPs by blending polymers, we synthesized carboxylate-functionalized copolymer poly(D,L-lactic-co-glycolic acid) (PLGA)-*b*-PEG by amide conjugation of COOH-PEG-NH_2 to PLGA-COOH. The synthesis is described in detail elsewhere (1). We also synthesized and characterized PLGA-*b*-PEG-Ald by multistep synthesis as described in Fig. S1. Furthermore, we evaluated the release kinetics of bortezomib from the NPs (single emulsion), at 37 °C, in PBS (1×) for varying time periods as analyzed by using HPLC. At all time points, the buffer was replaced to maintain the sink conditions. The affinity of Ald-conjugated NPs [Ald-PEG-PLGA (Ald-PP)] toward bone mineral [hydroxyapatite (HA)] was investigated in comparison with nontargeted (PP) NPs. Transmission electron microscopy (TEM) was used to analyze the interaction of targeted (Ald-PP) NPs to HA in the form of NP solution (targeted vs. nontargeted). The binding of targeted NPs to biomimetic HA crystals was analyzed under high-resolution scanning electron microscopy (SEM). Specific binding of Ald-PP NPs (PLGA-$Alexa_{647}$ labeled) to ex vivo bone fragments was also investigated by imaging under fluorescence microscope. In the next set of experiments, we studied the in vivo biodistribution, where $Alexa_{647}$-labeled Ald-PP NPs were used with whole-mouse imaging. NPs were injected i.p. and imaging was done at 1- and 24-h time points. Each mouse had >30 point source selections [excitation (ex): 675 nm; emission (em): 720 nm]. Thereafter, the mouse bones were dissected, sectioned, and imaged for investigation of bone homing of labeled NPs.

In Vitro and in Vivo Efficacy of Ald-PP NPs. Fluorescent-labeled NPs (PLGA-$Alexa_{647}$, single emulsion) were incubated with peripheral blood mononuclear cells (PBMCs) or MM1S cells and analyzed with flow cytometry for NP uptake (24 h). Furthermore, we investigated the in vitro efficacy of Bort-NPs (0.1 mg/mL, 0.04–0.09 wt/wt% drug load) by measuring apoptosis via flow cytometry, where MM1S cells were exposed to ∼0.9, ∼3.6, or ∼7.3 nM effective bortezomib concentrations (24 h). Controls consisted of an equivalent mass of empty NPs, and 10 nM free bortezomib (2). The same treatments were also studied by bioluminescence assay at 24 and 48 h. The in vivo efficacy studies used female Nod/SCID beige mice in treatment or pretreatment regimes. For treatment studies, mice injected with Luc^+/GFP^+ MM1S cells were randomly divided into four groups (n = 7). After injecting cancer cells, on day 21 mice were treated with the following: Ald-Empty-NPs, Free Drug (bortezomib), Ald-Bort-NPs, and Nontargeted Bort-NPs, and were imaged twice a week until day 38. Mice were injected (i.p.) twice a week with 0.5 mg/kg bortezomib or with an equivalent amount of Ald-Empty-NPs. In the case of NP pretreatment regime, female Nod/SCID beige mice were randomized into three groups (n = 10) and injected (i.p.) thrice a week for 3 wk, with 0.3 mg/kg bortezomib or with an equivalent amount of Ald-Empty-NPs. The pretreatment groups were as follows: Ald-Bort-NPs, Free Drug, and Ald-Empty-NPs in study 1 and Ald-Bort-NPs, Ald-Empty-NPs, and Nontargeted Bort-NPs in study 2. After 3 wk, the mice were injected with Luc^+GFP^+ MM1S cell. Bioluminescent imaging (BLI) was performed weekly on these mice, and survival was assessed. Additionally, an ex vivo micro-computed tomography (micro-CT) analysis and static histomorphometry (3) of mouse bones (femur, tibia, and fibula) were performed after 3-wk pretreatment period to validate bortezomib-induced increase in osteogenesis.

Statistical Analysis. Prism 5.0 or 6.02 software was used to compute all statistical calculations. BLI and $Alexa_{647}$ signal was compared between groups using Student's t tests with correction for multiple comparisons made and statistical significance determined using the Holm–Sidak method with $\alpha = 0.05$. ANOVA with Dunnet's or Tukey's post hoc multiple-comparison tests were used with $P < 0.05$ considered significant for analysis of data with more than one comparison. Survival statistics were determined using the log-rank (Mantel–Cox) test or the Gehan–Breslow–Wilcoxon test. Data are plotted as means ± SEM, unless otherwise stated.

Materials. The polymer poly(D,L-lactic-co-glycolic acid) (50/50) with terminal carboxylate groups (PLGA, inherent viscosity, 0.55–0.74 dL/g in hexafluoroisopropanol; M_r, 45 kDa) was obtained from Lactel Absorbable Polymers. NH_2-PEG-COOH (M_r, 5 kDa) and *t*BOC-NH_2-PEG-COOH (M_r, 5 kDa) were purchased from Laysan Bio. All reagents were analytical grade or above and used as received, unless otherwise stated. Alexa cadaverine dyes (647 and 405) were purchased from Invitrogen. The sodium alendronate, *N*-hydroxysuccinimide (NHS), ethyl-3-(3-dimethylaminopropyl) carbodiimide (EDC), HA, and any other chemicals were purchased from Sigma-Aldrich.

Cell Culture. The human multiple myeloma cell line MM1S was purchased from ATCC and engineered to express GFP and firefly luciferase (Luc^+/GFP^+ MM1S cells) as previously described (4) and cultured in 500 μg/mL geneticin (Invitrogen) for selection. PBMCs were obtained from healthy subjects by Ficoll-Hypaque density separation as recommended by the manufacturer (StemCell Technologies). Cells were cultured at 37 °C in RPMI 1640 containing 10% (vol/vol) FBS (Sigma-Aldrich), 2 mM L-glutamine, 100 U/mL penicillin, and 100 μg/mL streptomycin (Gibco). Primary human BM-derived mesenchymal stromal cells (MSCs) obtained from normal healthy subjects (ND-MSCs) were isolated and cultured as previously described (5) in expansion media of DMEM (Invitrogen), 20% (vol/vol) FBS (Invitrogen), 100 U/mL penicillin, and 10 μg/mL streptomycin (Invitrogen). Clinical samples were collected from patients from Brigham and Women's Hospital; approval for these studies was obtained from the appropriate institutional review boards. Informed consent was obtained in accordance with the Declaration of Helsinki.

NP Formulation and Characterization. To optimize NP formulation with suitable physicochemical characteristics, and to vary the target ligand density on NP surface along with maximization of NP drug load, we prepared a library of NPs. The NP library was designed using different polymer molecular weight, blending different polymer ratios, using different formulation techniques such as nanoprecipitation and emulsions, and varying the conditions of formulations. We further maximized the drug load by optimizing the initial drug feed. In the solvent dispersion method

of formulation, a blend of polymers PLGA-*b*-PEG-COOH and PLGA-*b*-PEG-Ald (10 mg/mL, in acetonitrile) was mixed with bortezomib (Selleck; 100 μM, in DMSO, 0.5% by weight of polymer). The polymer–drug mixture was added dropwise to a large excess of water [1:10 organic to aqueous (vol/vol)], at a constant stirring (600 rpm, Corning MP9I), to give a final NP concentration of 1 mg/mL. NPs were stirred for another 4 h to harden the NPs and remove excess organic solvents. The NPs were filtered, concentrated, and purified from the organic solvent, unencapsulated drug, and excess polymer. The NPs were washed (PBS) three times using an Amicon centrifugation filtration membrane with a molecular mass cutoff of 100 kDa.

In the case of the single-emulsion formulation method, the polymer blend of PLGA-*b*-PEG-COOH and PLGA-*b*-PEG-Ald (5 mg/mL, in chloroform) was mixed with bortezomib (1 mM, DMSO, 3% weight of polymer), and emulsified with an aqueous phase [1:12 organic to aqueous phase (vol/vol)] using a probe sonicator. The emulsions were stabilized by adding polyvinyl alcohol (0.2%) to the aqueous phase. The sonication conditions of output power and duration significantly affected the size and drug load of NPs. We standardized the sonication conditions to using an output power of 45 W for 3 min (5-s pulse with 1-s stop time) for maximal drug load and optimal NP size. The NP emulsions were then diluted to 10 mL of water and stirred at room temperature for 6 h. The NPs were purified and concentrated as described above.

The hydrodynamic diameter and surface charge (ζ potential; in millivolts) of NPs were determined by quasi-elastic laser light scattering using a ZetaPALS dynamic light scattering (DLS) detector (Brookhaven Instruments) in 20 mM isotonic 4-(2-hydroxyethyl)piperazine-1-ethanesulfonic acid (Hepes) buffer saline, pH 7.4, at room temperature (RT). Experiments were performed in triplicate.

TEM images of NPs and NP interaction with calcium phosphate nanocrystals were obtained using JEOL 2011 instrument at an accelerated voltage of 80 kV. The sample was prepared by depositing 10 μL of NP suspension (0.1 mg/mL) onto a 300-mesh carbon-coated copper grid. The samples were blotted away after 5- to 10-min incubation, air-dried, and allowed it to further dry in vacuum. The grids were counterstained with 1% uranyl formate to enhance the contrast. Representative images are shown from experiments in triplicate.

Synthesis and Characterization of Polymers: PLGA-*b*-PEG-COOH, PLGA-*b*-PEG-Ald, PLGA-Alexa$_{647}$, and PLGA-Alexa$_{405}$. Carboxylate-functionalized copolymer PLGA-*b*-PEG was synthesized by amide conjugation of COOH-PEG-NH_2 to PLGA-NHS according to ref. 1. In brief, 50:50 poly(D,L-lactic-co-glycolic acid) (0.55–0.74 dL/g) (100 mg, 0.0023 mmol) was dissolved in 1 mL of dry dichloromethane (DCM); to this was added EDC (4.41 mg, 0.023 mmol) in dry DCM (0.5 mL), and the reaction was stirred for 10 min followed by addition of NHS (2.65 mg, 0.023) in dry DCM (0.5 mL). The reaction was stirred at RT for 60 min. The PLGA-NHS–activated polymer was precipitated with 20 mL of cold 1:1 MeOH/Et_2O mixture and centrifuged at 2,700 × *g* for 10 min to remove residual EDC/NHS. The washing and centrifugation steps were repeated twice, and the polymer was then dried under vacuum for 90 min to remove residual solvents. After drying, PLGA-NHS was dissolved in DCM (1 mL) followed by the addition of NH_2-PEG$_{(5kDa)}$-COOH (13.33 mg, 0.0028 mmol) dissolved in dry chloroform (0.5 mL), in dry chloroform, followed by the addition of *N*,*N*-diisopropylethylamine (DIEA) (3.62 mg, 0.028 mmol), and the reaction was stirred for 12 h at RT. The copolymer was then precipitated by dropwise addition into cold diethylether/methanol (15:35 mL) and centrifuged (3,000 × *g* for 5 min). The supernatant was decanted, and the pellet redissolved in $CHCl_3$ (1 mL), precipitated, and washed further (three times) and dried under vacuum to yield PLGA-b-PEG-COOH (yield 85%). Polymer characterization: ^{1}H NMR (400 MHz, $CDCl_3$): δ 5.22 (m, [-OC$\underline{H}$(CH_3)CONH-]), 4.82 [m, (-OC$\underline{H}_2$COO-)], 3.63 [s, (-C$\underline{H}_2$C$\underline{H}_2$O-)], 1.58 (d, [-OCH(C$\underline{H}_3$)CONH-]) ppm.

To synthesize NH_2-PEG-*b*-Ald, *t*BOC-PEG-NHS was stirred with Ald (free acid form) in DMSO, at 1:1 molar ratio, for 6 h at RT. The reaction mixture was concentrated under vacuum and added to cold diethyl ether. After 1 h, at −20 °C, the product, *t*BOC-PEG-Ald, thus obtained, was filtered and dried under vacuum. Subsequently, *t*BOC-PEG-Ald (anhydrous dichloromethane) was stirred at RT for 1 h, with tin (IV) chloride (5 mmol) under anhydrous conditions, for BOC- deprotection, and the product was dried under vacuum. NH_2-PEG-Ald was purified as described above. Polymer characterization: ^{1}H NMR (400 MHz, DMSO-d6): δ NH_2-PEG-Ald: 3.63 [s, (-O-C$\underline{H}_2$C$\underline{H}_2$)], 2.98 (m, Ald: -CCH$_2$CH$_2$C$\underline{H}_2$NHCOCH$_2$-), 1.92 (m, Ald: -CC$\underline{H}_2$C$\underline{H}_2$CH$_2$NHCO-) ppm.

PLGA-*b*-PEG-Ald was synthesized by conjugation of NH_2-PEG-Ald to PLGA-COOH by using EDC and NHS to activate PLGA-COOH, as described above (yield, 70%). Polymer characterization: ^{1}H NMR (400 MHz, DMSO-d6): δ PLGA-*b*-PEG-Ald: 5.20 (m, [-OC$\underline{H}$(CH_3)COO-]), 4.89 [m, (-OC$\underline{H}_2$COO-)], 3.50 [s, (-C$\underline{H}_2$C$\underline{H}_2$O-)], 3.02 (m, Ald: -CCH$_2$CH$_2$C$\underline{H}_2$NHCOCH$_2$-), 1.89 (m, Ald: -CC$\underline{H}_2$C$\underline{H}_2$CH$_2$NHCO-), 1.47 (-OCH(C$\underline{H}_3$)CONH-) ppm.

To synthesize PLGA-Alexa$_{647}$ or PLGA-Alexa$_{405}$, 50:50 poly (DL-lactide-coglycolide) (0.55–0.74 dL/g) (100 mg, 0.0023 mmol) was dissolved in 1 mL of dry DCM; to this was added EDC (4.41 mg, 0.023 mmol) in dry DCM (0.5 mL), and the reaction was stirred for 10 min followed by addition of NHS (2.65 mg, 0.023) in dry DCM (0.5 mL). The reaction was stirred at RT for 60 min. The PLGA-NHS–activated polymer was precipitated with 20 mL of cold diethylether/methanol (1:1) mixture and centrifuged at 2,700 × *g* for 10 min to remove residual EDC/NHS. The washing and centrifugation steps were repeated twice, and the polymer was then dried under vacuum for 90 min to remove residual solvents. After drying, PLGA-NHS was dissolved in DCM (1 mL) followed by the addition of Alexa$_{647}$ cadaverine or Alexa$_{405}$ cadaverine (0.0028 mmol) dissolved in dry DCM (0.5 mL), followed by the addition of DIEA (3.62 mg, 0.028 mmol), and the reaction was stirred for 12 h at RT. The polymer was then precipitated with 20 mL of cold 1:1 MeOH/Et_2O mixture and centrifuged at 2,700 × *g* for 10 min. The washing was repeated twice more, and the product dried under vacuum (to obtain a blue polymer compound). The supernatant was decanted, and the pellet was redissolved in $CHCl_3$, precipitated, washed further (three times), and dried under vacuum to yield fluorescently labeled PLGA (yield, 90%). Polymer characterization: 1H NMR (400 MHz, $CDCl_3$): δ PLGA peaks: 5.21 (m, [-OCH(CH_3)CONH-]), 4.83 [m, (-OCH$_2$COO-)], 1.59 (d, [-OCH(CH_3)CONH-]) ppm.

Phosphate Assay. The ratio of Ald to polymers in the Ald-PP NPs (single emulsion) was determined using a phosphate assay. The PLGA-*b*-PEG-Ald NPs (10 μL of 10 mg/mL NPs in water) were mixed with 60 μL of concentrated H_2SO_4 and 10 μL of H_2O_2 in glass tubes, and heated for 10 min at 200 °C. Thereafter, 690 μL of $Na_2S_2O_5$ (3 mg/mL) was added to the tubes, and the samples were incubated at 100 °C for 5 min. This was followed by adding 200 μL of $(NH_4)_6Mo_7O_{24}{\cdot}4H_2O$ (20 mg/mL) and 20 μL of ascorbic acid (100 mg/mL) to the glass tubes and incubation for another 10 min at 100 °C. The absorbance of the sample solutions was determined at 820 nm and was used to determine phosphate concentrations of the samples. The calibration curves were based on known concentrations of Na_2HPO_4 as standards. PP NPs were used as negative controls (6). Experiments were performed in triplicate.

Drug Encapsulation and Release Kinetics. To evaluate the release kinetics of bortezomib from the NPs, a NP (single-emulsion) solution (1 mg/mL, in PBS) was incubated at 37 °C, in triplicates

for varying time periods. NPs were made as described encapsulating small molecule therapeutics, such as bortezomib. In the case of the small molecular drugs, such as chemotherapeutic drugs, the NP solution (1 mg/mL, in PBS), were placed in a dialysis bag with suitable molecular weight cutoff range based on the drug used (e.g., molecular mass cutoff, 3,400 Da for bortezomib). At each time point, the NPs were collected from the dialysis bag, dissolved in organic solvent (acetonitrile), and analyzed using HPLC. At all time points, the buffer was replaced to maintain the sink conditions. Experiments were performed in triplicate.

In Vitro Bone Targeting (HA Binding and Bone Affinity). The affinity of Ald-conjugated PEG-PLGA NPs (Ald-PP, single emulsion) toward bone mineral and bone fragments (ex vivo) was investigated in comparison with nontargeted PEG-PLGA (PP, single emulsion) NPs. Fluorescent labeled NPs (PLGA-Alexa$_{647}$) stable in physiological salt concentration and temperature, at pH 7.4, were incubated with HA (HA microparticles) in microfuge tubes and stirred (Sanyo Orbital Incubator) for varying lengths of time (5, 30 min, 2, 4, 6, 12, and 24 h). At the end of incubation time, the HA microparticles and the NPs bound to them settled down, when the microfuge tubes were spun at 85 × *g* for 5 min. The binding affinity of targeted NPs (fluorescent labeled) was determined by measuring the decrease in the relative concentration (by measuring the fluorescence) of targeted Ald-PP NPs in the supernatant compared with that of nontargeted PP NPs. Experiment was performed in triplicate.

Interactions of Ald-PP NPs to bone mineral (HA NPs) was further clearly confirmed at the nanoscale by TEM imaging of HA in the form of NP rods in solution phase when incubated with polymeric NP solutions (targeted vs. nontargeted). The sample solution was loaded on TEM grids, air-dried, and counterstained with 0.5% uranyl formate, as described above in the NP characterization section. Representative images are shown from experiments in triplicate.

The binding of Ald-PP NPs to biomimetic calcium phosphate (HA) was further investigated by SEM. The biomimetic calcium phosphate crystals were generated by simulated body fluid (5× concentration) on a solid surface (1 × 0.5 cm glass). The crystals were incubated with NPs in aqueous solution (1 mL of 0.5 mg/mL concentration) for 3 min with constant stirring on an orbital shaker, washed three times with deionized water (1 mL), dried overnight under vacuum, and coated with gold to visualize under high-resolution SEM with backscattering electron detector. Representative images are shown from experiments in triplicate.

Specific binding of Ald-PP NPs (PLGA-Alexa$_{647}$ labeled) to ex vivo bone fragment (skull, mice, 2 mm × 2 mm) compared with that of PP NPs was investigated by imaging under fluorescent microscope. Bone fragments were incubated with NP solution (0.1 mg/mL) for 30 min in physiological salt, pH, and temperature conditions, with constant stirring at 100 rpm (Lab Industries Inc. Labquake Shaker CAT No. 400-110), and after incubation, the bone pieces were washed three times with PBS, air dried in dark, and imaged again. Representative images are shown from experiments in triplicate.

Alizarin Red Staining of Bortezomib-Induced Osteogenesis. Osteogenic media (OM) consisting of αMEM supplemented with 10% (vol/vol) FBS, 100 U/mL penicillin, 10 μg/mL streptomycin (Invitrogen), 2 mM L-glutamine (Invitrogen), 0.05 mM ascorbic acid, 100 nM dexamethasone, and 10 mM β-glycerophosphate, was used. MSCs were seeded into 96-well plates grown to 95% confluence, allowed to proliferate in one of the following culture media for 1 wk, and stained for mineralization using Alizarin red: (*i*) regular MSC expansion media, (*ii*) OM, (*iii*) OM plus 0.5 mM Bort, (*iv*) OM plus 1 mM Bort. Media was then removed and cells were fixed with 4% (wt/vol) paraformaldehyde for 5 min, washed with deionized water, stained with Alizarin Red solution (Sigma) [2% (wt/vol), pH 4.2] for 10 min, washed again with deionized water, and imaged. Bright-field images were taken with an Olympus CKX41 microscope and an Olympus DP72 camera and a dry 4× objective. Representative images are shown from experiments in triplicate.

Cellular Uptake. Fluorescently labeled NPs (PLGA-Alexa$_{647}$ or PLGA-Alexa$_{405}$) (single emulsion) were incubated with PBMCs or MM1S cells, and analyzed with flow cytometry on a FACsCanto II (BD) for NP uptake. Total cell populations were identified based on forward-scatter (FSC) and side-scatter (SSC) gates and, if needed, fluorescently labeling (DiO$^+$ PBMCs, GFP$^+$ MM1S cells), and the fraction of these that contained NPs were identified by Alexa$_{647}$ positivity. All gates were identical within individual experiments. Cells were seeded in 1 mL of media in 24-well plates, 0.25 × 10^6 cells per well, incubated with 200 μg of NP solution (PBS), and sorted in FACS buffer [PBS plus 5% (vol/vol) FBS] immediately after sampling.

Fluorescent and Two-Photon Microscopy. To image cellular uptake of NPs labeled with the fluorescent dye Alexa$_{647}$ (Invitrogen), GFP$^+$ MM1S cells were incubated with labeled NPs (PLGA-Alexa$_{647}$) (single emulsion) for 24 h, washed repeatedly, and imaged using GFP and Cy5.5 filter cubes in a Nikon inverted TE2000 microscope (100× Plan-Apochromat Phase, N.A. 1.4, oil-immersion objective) with a Hamamatsu Orca ER digital CCD camera. Images were collected using Leica software where the GFP signal was colored green and Alexa$_{647}$ signal was colored red. To image Alexa$_{405}$-labeled NPs, GFP$^+$ MM1S cells were incubated with labeled NPs for 24 h, washed repeatedly, and imaged using a two-photon Zeiss 710 confocal system Coherent Chameleon Vision II laser (wavelength range, 680–1,040 nm). Samples were excited with 800 nm, 14% power with a 63× W-Plan Apochromatic, N.A. 1.0, objective on an upright Axio Examiner Z1 stand. GFP signal from cells was detected in NDD2 using a BP filter (500–550 nm), and Alexa$_{405}$ signal was detected in NDD3 using a short-pass filter (485). Images were collected using eight line sum averages with GFP signal colored green and Alexa$_{405}$ colored red, and processed using Zeiss software (Zen 2009).

Apoptosis Flow Cytometry Assays. MM1S cells were grown in 1 mL of media in 24-well plates, 0.25 × 10^6 cells per well, and treated with NPs [0.1 mg/mL, 0.04–0.07% (wt/wt) drug loading, single emulsion], with an effective drug concentration of low (~0.9 nM), medium (~3.6 nM), or high (~7.3 nM) doses of bortezomib. As a control, an equivalent amount of empty (no drug) NPs, and 5 and 10 nM free bortezomib were used. At 24 h, Annexin V–FITC and propidium iodide staining were used to detect and quantify apoptosis by flow cytometry (BD FACSCanto II HTS) following manufacturer's instructions, as previously described (2).

In Vitro Bioluminescence Assays. MM1S cells were seeded at 50,000 cells per well in opaque 96-well plates in 100 μL of media. Cells were treated with NP (0.1 mg/mL concentration, single emulsion) loaded with bortezomib [0.04–0.07% (wt/wt)] in an effective drug concentration range of low (~0.9 nM), medium (~3.6 nM), or high (~7.3 nM) doses of NPs for 12, 24, and 48 h. D-Luciferin substrate (7.5 mg/mL, 5 μL per well) was added to wells 5 min before measurement on a BMG LABTech PHERAstar plate reader with PHERAstar software, version 1.60, using an open emission filter.

In Vivo Biodistribution Studies. Athymic nude mice and BALB/c at 6 wk were purchased from Charles River for biodistribution studies. Alexa$_{647}$-labeled Ald-conjugated NPs (single emulsion) were synthesized with 5% of the total polymer as PLGA-

Alexa$_{647}$, and characterized for stability before injection. Mice were fed Non-Fluorescent Diet 48 h before injection and kept on the diet for the remainder of the study. For whole-mouse imaging, 1 mg of Alexa$_{647}$-labeled NPs in PBS was injected i.p. for in vivo imaging system (IVIS) FLIT imaging (Caliper Life Sciences) in the Koch Institute Whole Animal Imaging Core, and time points examined were 1 and 24 h. Each mouse had >30 point source selections (ex: 675 nm; em: 720 nm). All quantitative imaging analysis was conducted using Living Image 4.2 software.

NP Treatment of Multiple Myeloma in Vivo. Approval for all animal studies was obtained from the Dana-Farber Cancer Institute and Massachusetts Institute of Technology Institutional Animal Care and Use Committee offices and institutional review boards. Female Nod/SCID beige mice, 6–7 wk old (Charles River Laboratories), were injected with 4×10^6 Luc$^+$/GFP$^+$ MM1S cells per mouse via the tail vein. Using $n = 7$ mice per group, mice were randomly divided into the following groups: group 1, no bortezomib Ald-PP NPs; group 2, Free Drug (bortezomib in PBS); group 3, Ald-PP NPs loaded with bortezomib; group 4, PP NPs loaded with bortezomib. Mice were injected i.p. with 0.5 mg/kg bortezomib twice a week or with an equivalent amount of no drug NPs (group 1). BLI was performed weekly until signal was detected (day 21), and the mice were then injected with the drug treatments and imaged twice a week. Specifically, mice were imaged at 0, 7, 14, 21, 24, 28, 31, 35, and 38 d. Mice were killed via CO_2 inhalation at endpoints described or, for survival studies, mice when they had hindlimb paralysis, cachexia, weight loss of >15%, or become moribund.

NP Pretreatment of Multiple Myeloma in Vivo. Female NOD/SCID beige mice, 6–7 wk old (Taconic), were randomized into three groups ($n = 7$) and pretreated for 3 wk as follows: group 1, Ald-Bort-NPs; group 2, Free Drug; group 3, Ald-Empty-NPs. Mice were injected i.p. thrice a week with 0.3 mg/kg bortezomib or with an equivalent amount of no drug NPs (group 3). Then mice were injected with 4×10^6 Luc$^+$GFP$^+$ MM1S cell per mouse via the tail vein. BLI was performed on $n = 10$ mice per group weekly until signal was detected and then imaged twice a week at days 7, 14, 21, 24, and 29 until mice began to succumb to the disease and were then observed for survival. In another study, mice were randomized into three groups ($n = 10$) and pretreated for 3 wk as follows: group 1, Ald-Bort-NPs (targeted); group 2, Bort-NPs (nontargeted); group 3, Ald-Empty-NPs. Mice were injected i.p. three times a week with 0.3 mg/kg bortezomib or with an equivalent amount of no-drug NPs (group 3) and monitored for survival.

Detection of Tumor Progression by Bioluminescence Imaging. Mice were injected with 75 mg/kg luciferin (Caliper Life Sciences), followed by whole-body real-time bioluminescence imaging (Xenogen IVIS imaging system; Caliper Life Sciences) 5 min after injection. BLI signal was collected for 15 s, 1 and 5 min using the following settings: Emission Filter Open on an IVIS 1327 camera; binning (HR), 4; field of view, 25; flux stop, 1. Total flux (photons per second) was calculated based on 4 × 8-cm regions of interest of dorsal images.

Bone Histomorphometry. Tibiae from the mice were dissected and fixed. After fixation, tibiae were dehydrated and embedded in methyl methacrylate without demineralization. Undecalcified 4-μm-thick sections were taken, and Von Kossa staining was performed. Consecutive sections were stained by tartrate-resistant acid phosphatase and toluidine blue to quantitate structure and cellular parameters by bone histomorphometry. Bone histomorphometry was performed at secondary spongiosa 200 μm below the growth plate using the Osteomeasure system (OsteoMetrics), and the results were expressed according to the standardized nomenclature (3).

Ex Vivo Micro-CT Analysis of Bones from NP Pretreatment. Micro-CT of leg bones (femur, tibia, and fibula) from pretreated mice were dissected from killed mice after the 3-wk pretreatment period to validate bortezomib-induced increase in osteogenesis. Femurs stored in 4% (wt/vol) paraformaldehyde solution were analyzed on a Scanco Medical MicroCT 35 system with an isotropic voxel size of 7 μm. Scans were conducted with an X-ray tube potential of 70 kVP, an X-ray intensity of 0.145 mA, and an integration time of 600 ms per tomographic projection.

1. Pridgen EM, et al. (2013) Transepithelial transport of fc-targeted nanoparticles by the neonatal fc receptor for oral delivery. *Sci Transl Med* 5(213):213ra167.
2. Leleu X, et al. (2007) The Akt pathway regulates survival and homing in Waldenstrom macroglobulinemia. *Blood* 110(13):4417–4426.
3. Dempster DW, et al. (2013) Standardized nomenclature, symbols, and units for bone histomorphometry: A 2012 update of the report of the ASBMR Histomorphometry Nomenclature Committee. *J Bone Miner Res* 28(1):2–17.
4. Azab AK, et al. (2009) CXCR4 inhibitor AMD3100 disrupts the interaction of multiple myeloma cells with the bone marrow microenvironment and enhances their sensitivity to therapy. *Blood* 113(18):4341–4351.
5. Roccaro AM, et al. (2013) BM mesenchymal stromal cell-derived exosomes facilitate multiple myeloma progression. *J Clin Invest* 123(4):1542–1555.
6. Zhang S, Wright JEI, Bansal G, Cho P, Uludag H (2005) Cleavage of disulfide-linked fetuin-bisphosphonate conjugates with three physiological thiols. *Biomacromolecules* 6(5):2800–2808.

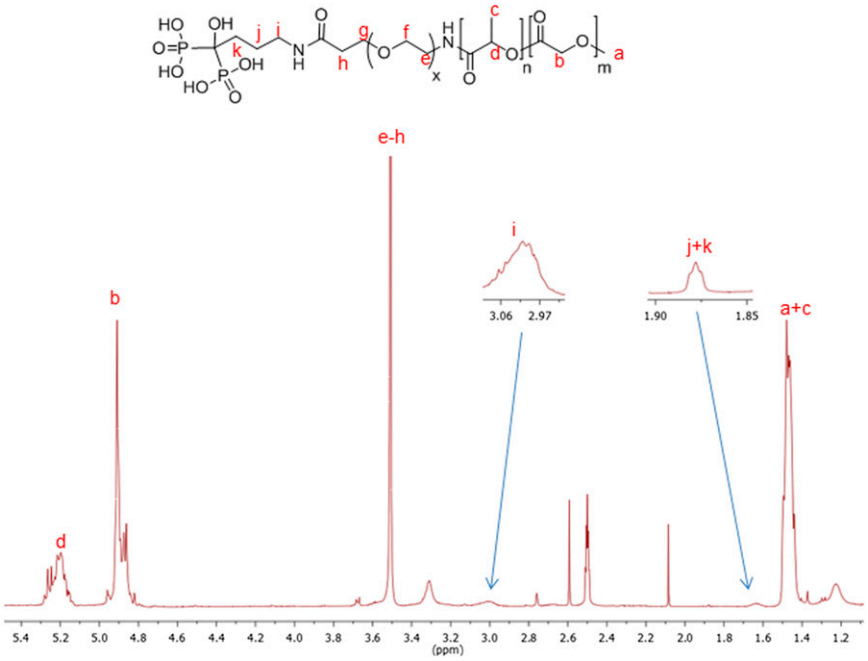

Fig. S1. Scheme of PLGA-*b*-PEG-Ald and associated 1H NMR.

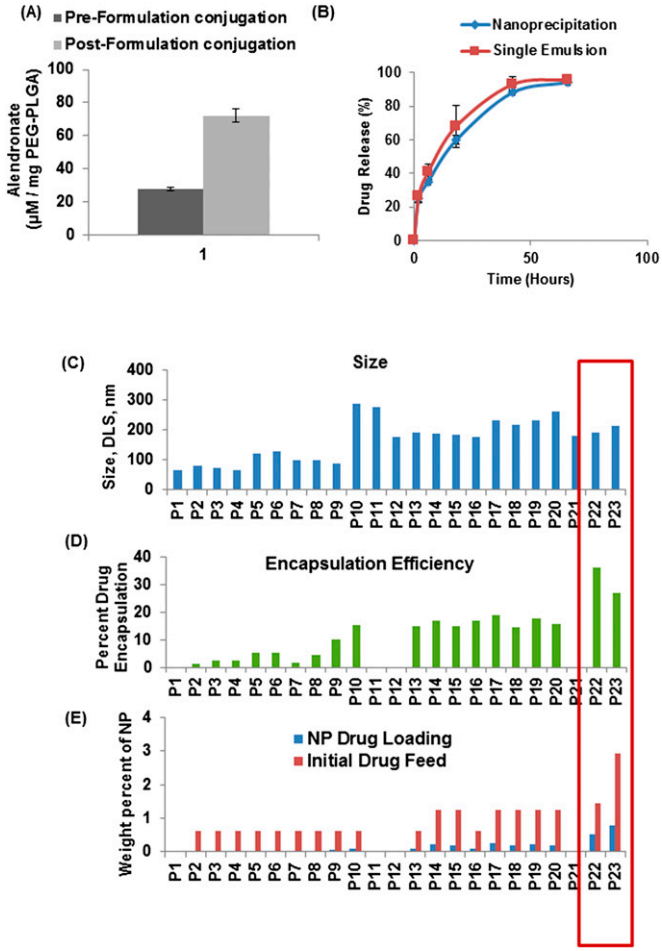

Fig. S2. (*A*) The content of Ald in Ald-PP NPs using phosphate assay. The Ald was incorporated in the NPs in two different ways: preformulation and postformulation conjugation. In preformulation conjugation, the Ald-conjugated polymer (PLGA-*b*-PEG-Ald) was blended with the PLGA-*b*-PEG polymer to formulate Ald-PEG-PLGA NPs, and in postformulation conjugation, the Ald was conjugated to the HOOC- groups on the surface of the formulated PEG-PLGA NPs made by polymer blends (PLGA-b-PEG-COOH; PLGA-b-PEG-OMe). The preformulation method of incorporating Ald to the NPs was chosen for all of the experiments performed in the study, as it gives a precise control over Ald density on NP surface with minimal batch-to-batch variability. (*B*) Release kinetics of bortezomib for NPs presented as percentage of the total drug encapsulated. (*C*) Size (hydrodynamic diameter, dynamic light scattering (DLS)], (*D*) drug encapsulation efficiency (percentage), (*E*) initial drug feed and drug loading (percentage) of a library of NPs. The NP library was synthesized using different formulation technique such as nanoprecipitation (P1–P9), double emulsion (P10–P11), and single emulsion (P12–P23). Formulation conditions such as organic to aqueous phase ratio (vol/vol), concentration of polymer in organic phase, initial feed of drug, and polymer molecular weights were varied. The optimized NPs (P22, P23) with optimal size (~190 nm), nearly neutral surface charge, maximal drug encapsulation efficiency (25–30%), and maximal drug load (0.75%) were formulated by single emulsion as described in *Materials and Methods*.

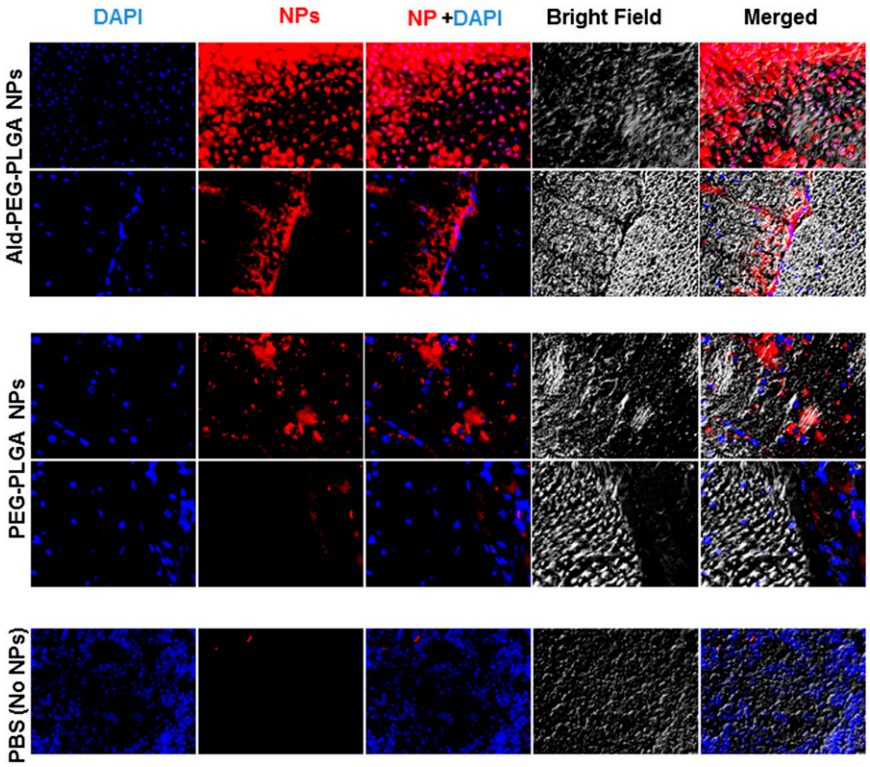

Fig. S3. Representative images of bone histology images in fluorescent channel 405 (DAPI, nuclear material), 647 (NPs, PLGA-Alexa647), bright field, and merged; for targeted (Ald-PP) NPs (*Top*), nontargeted (PP) NPs (*Middle*), and control (*Bottom*). (Scale bar: 100 μm.)

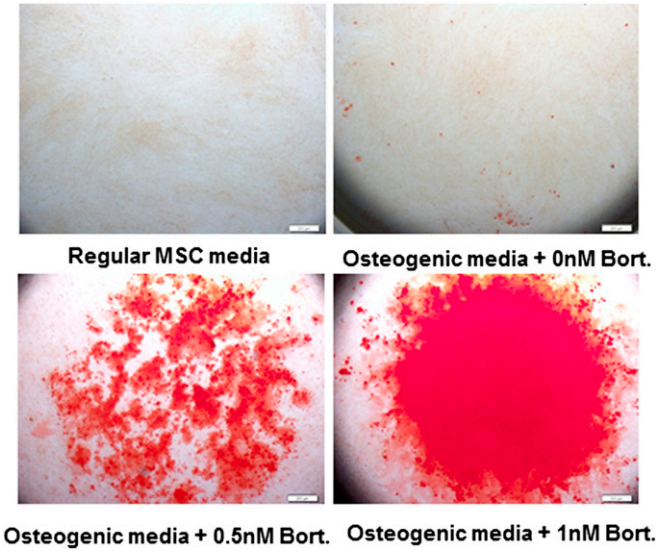

Fig. S4. Alizarin Red staining after 1 wk of differentiation demonstrate ability for bortezomib to increase osteogenic differentiation of bone marrow-derived mesenchymal stem cells.

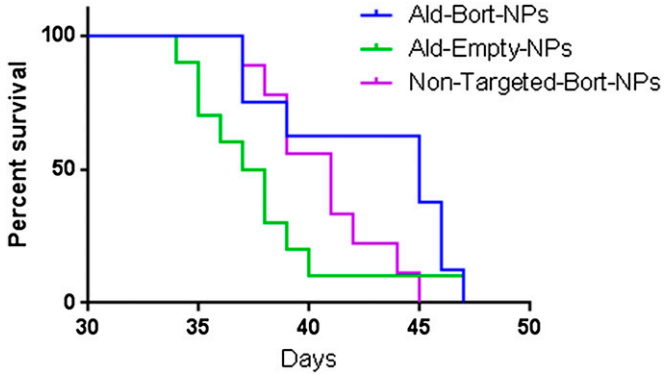

Fig. S5. Pretreatment with Ald-Bort-NPs inhibits myeloma growth. Mice were pretreated for 3 wk with Ald-Bort-NPs (targeted, blue line), Ald-Empty-NPs (without bortezomib) (green line), and Bort-NPs (nontargeted, purple line). They were then injected with $GFP^{+}Luc^{+}$ MM1S cells and monitored for survival. Survival improved in the mice pretreated with targeted-bortezomib vs. non-targeted-bortezomib NPs, and both treatments significantly increased survival for mice vs. empty nanoparticle treatment (Gehan–Breslow–Wilcoxon test, $P = 0.02$).

Table S1. Histomorphometry data of mouse bones after 3 wk of pretreatment

				Statistical analysis		
Parameters	Ald-Empty-NP ($n = 6$)	Free drug (FD) ($n = 5$)	Ald-Bort-NPs ($n = 6$)	One-way ANOVA	FD vs. Ald-Empty-NP	Ald-Bort-NPs vs. Ald-Empty-NPs
BV/TV, %	8.59 ± 3.63	14.78 ± 6.18	13.16 ± 6.48	NS	NS	NS
Tb.Th, μm	37.09 ± 8.89	46.92 ± 7.17	42.72 ± 9.78	NS	NS	NS
Tb.N, /mm	2.29 ± 0.75	3.06 ± 0.77	2.94 ± 0.89	NS	NS	NS
Tb.Sp, μm	430.5 ± 121.5	295.5 ± 85.2	324.5 ± 115.8	NS	NS	NS
N.Ob/B.Pm, /mm	6.46 ± 2.35	6.95 ± 1.59	7.23 ± 2.21	NS	NS	NS
Ob.S/B.Pm, %	9.86 ± 3.91	11.06 ± 2.97	11.14 ± 3.41	NS	NS	NS
OS/BS, %	3.35 ± 2.18	3.84 ± 1.59	4.17 ± 1.76	NS	NS	NS
O.Th, μm	3.27 ± 1.50	4.89 ± 0.78*	5.06 ± 0.63*	$P < 0.05$	$P < 0.05$	$P < 0.05$
N.Oc/B.Pm, /mm	1.22 ± 0.31	0.82 ± 0.20*	1.01 ± 0.15	$P < 0.05$	$P < 0.05$	NS
Oc.S/B.Pm, %	3.68 ± 0.67	2.81 ± 0.90	3.32 ± 0.53	NS	NS	NS
ES/BS, %	4.67 ± 0.98	3.12 ± 0.71*	4.15 ± 0.65	$P < 0.05$	$P < 0.05$	NS

Data are mean ± SD. BV/TV, bone volume/total volume; Tb.N, trabecular number; Tb.Sp, trabecular separation; Tb.Th, trabecular thickness. Osteoblastic parameters: N.Ob/B.Pm, osteoblast number; Ob.S/B.Pm, osteoblast surface per bone perimeter; OS/BS, osteoid surface; O.Th, osteoid thickness. Osteoclastic parameters: ES/BS, eroded surface per bone surface; N.Oc/B.Pm, osteoclast number; Oc.S/B.Pm, osteoclast surface. *$P < 0.05$ compared with ET-NP, one-way ANOVA and the Dunnet's post hoc test.

From www.bloodjournal.org by guest on January 2, 2015. For personal use only.

Regular Article

LYMPHOID NEOPLASIA

Investigating osteogenic differentiation in multiple myeloma using a novel 3D bone marrow niche model

Michaela R. Reagan,[1] Yuji Mishima,[1] Siobhan V. Glavey,[1] Yong Zhang,[1] Salomon Manier,[1] Zhi Ning Lu,[1] Masoumeh Memarzadeh,[1] Yu Zhang,[1] Antonio Sacco,[1] Yosra Aljawai,[1] Jiantao Shi,[2] Yu-Tzu Tai,[1] John E. Ready,[1,3] David L. Kaplan,[4] Aldo M. Roccaro,[1] and Irene M. Ghobrial[1]

[1]Department of Medical Oncology, Dana-Farber Cancer Institute, Harvard Medical School, Boston, MA; [2]Department of Biostatistics, Harvard School of Public Health, Boston, MA; [3]Brigham and Women's Hospital, Boston, MA; and [4]Department of Biomedical Engineering, Tufts University, Medford MA

Key Points

- 3D bone marrow niche model recapitulates in vivo interactions of tumor and bone cells in a more biologically relevant system than in 2D.
- Differential expression levels of miRs in MSCs provide novel insights into mechanisms of regulation of osteoblasts in multiple myeloma.

Clonal proliferation of plasma cells within the bone marrow (BM) affects local cells, such as mesenchymal stromal cells (MSCs), leading to osteolysis and fatality in multiple myeloma (MM). Consequently, there is an urgent need to find better mechanisms of inhibiting myeloma growth and osteolytic lesion development. To meet this need and accelerate clinical translation, better models of myeloma within the BM are required. Herein we have developed a clinically relevant, three-dimensional (3D) myeloma BM coculture model that mimics bone cell/cancer cell interactions within the bone microenvironment. The coculture model and clinical samples were used to investigate myeloma growth, osteogenesis inhibition, and myeloma-induced abnormalities in MM-MSCs. This platform demonstrated myeloma support of capillarylike assembly of endothelial cells and cell adhesion–mediated drug resistance (CAM-DR). Also, distinct normal donor (ND)- and MM-MSC miRNA (miR) signatures were identified and used to uncover osteogenic miRs of interest for osteoblast differentiation. More broadly, our 3D platform provides a simple, clinically relevant tool to model cancer growth within the bone—useful for investigating skeletal cancer biology, screening compounds, and exploring osteogenesis. Our identification and efficacy validation of novel bone anabolic miRs in MM opens more opportunities for novel approaches to cancer therapy via stromal miR modulation. (*Blood*. 2014;124(22):3250-3259)

Introduction

Increasing evidence demonstrates that matrix stiffness, geometry, chemistry, and spatial dimensionality, along with neighboring cells and soluble factors, regulate cellular behavior and tissue formation.[1] However, current in vitro multiple myeloma (MM) research is conducted on 2D in vitro culture plates, highlighting the need for more realistic 3D in vitro models of myeloma growth.[2] Many 3-dimensional (3D) culture and coculture systems have been described for MM and have validated the importance and relevancy of using 3D rather than 2D culture systems to more accurately model myeloma growth. Some of these models have used hydrogels (made from permutations of collagen, fibronectin, and Matrigel[3,4]), which are, as with our model, advantageous as simple, controllable, and reproducible 3D culture microenvironments useful for studying pharmaceuticals or biological pathways. However, our system transcends these properties to comprise a model representative of a mineralized bone microenvironment using bone marrow (BM)-derived mesenchymal stromal cells (MSCs) that are stimulated to undergo osteogenic differentiation on the strong, porous silk scaffolds, which does not occur on softer substrates. This is a critical component to a 3D model of myeloma and bone, because myeloma cells respond differently to undifferentiated MSCs compared with MSCs differentiated into osteoblasts and osteocytes.[5] On the other end of the spectrum are the models that use 100% biologically relevant patient-derived, whole-bone cores,[6] taken directly from patients, which have the advantage of providing a hard, mineralized, bony matrix but that lack the reproducibility, adaptability, scalability, controllability, and simplicity that characterize our tissue-engineered bone (TE-bone) model. Although this is beneficial for small-scale, individualized patient analyses, patient samples vary widely in results and responses in terms of myeloma growth and drug response, making large drug screens or biological pathway analyses impossible. Moreover, the 3D bioreactor system necessary for patient-bone core culture makes the system much more time- and cost-consuming than 3D TE-bone, which can be completely user-defined in terms of size, shape, porosity, and other parameters, and can be produced as hundreds of identical samples. Silk scaffolds, the platform of our TE-bone, can also be modified in terms of pore size, dimensions, Young's modulus, degradation speed, and seeded cellular components. Finally, our TE-bone can be used in vitro or in vivo, monitored using live, nondestructive optical imaging, and processed using flow cytometric

Submitted February 24, 2014; accepted August 25, 2014. Prepublished online as *Blood* First Edition paper, September 9, 2014; DOI 10.1182/blood-2014-02-558007.

The online version of the article contains a data supplement.

The publication costs of this article were defrayed in part by page charge payment. Therefore, and solely to indicate this fact, this article is hereby marked "advertisement" in accordance with 18 USC section 1734.

© 2014 by The American Society of Hematology

From www.bloodjournal.org by guest on January 2, 2015. For personal use only.

techniques for analysis of cellular populations. Herein we use this novel disease model to demonstrate real-time inhibition of osteogenic differentiation in response to myeloma cells.

Osteolytic cancers such as MM develop via forward-feedback mechanisms with local MSCs in the BM, leading to devastating skeletal consequences (ie, pain, hypercalcemia, osteolysis, and fracture) and accelerated tumor growth.[7] MM cells insidiously overtake normal bone homeostasis to decrease osteoblastic activity and increase osteoclastic activity by altering local microenvironment cells.[8] MM patient–derived MSCs (MM-MSCs) exhibit decreased proliferation and osteogenesis and an inability to repair osteolytic damage, and they display great patient-to-patient heterogeneity in their ability to undergo differentiation and induce changes in MM cells.[8-10] The tumor BM microenvironment also supports tumor growth,[11] induces chemoresistance, and selects for tumor-initiating clones.[12] Therefore, a realistic model of the abnormal BM seen in MM patients would greatly benefit translational research scientists.

In myeloma patients, bone lesions with concomitant bone fractures and osteoporosis often persist despite bisphosphonate or bortezomib administration, tumor cell ablation, or disease remission.[13,14] This is partially explained by functional and gene expression differences between MM-MSCs and normal donor (ND)-MSCs.[8,15-18] However, mechanisms governing ineffectual MM-MSC osteogenesis remain unclear, and the roles of microRNAs (miRs) in this process are unknown. This highlights our need for stroma-specific targets and therapies, which can be identified only with more realistic 3D bone cancer models.

Our 3D in vitro BM model recapitulates interactions among tumor cells, stroma cells (MSCs), and endothelial cells, and the osteogenic process in normal and myeloma conditions. Our purpose was to examine dynamic cell-to-cell interactions between tumor cells and supportive cells, to determine the inhibitory effects of MM cells on osteogenesis and to develop a robust preclinical model to accelerate the rate of discovery and development of efficacious cancer treatments.

Methods

Study approval

Approval for these studies was obtained from the Dana-Farber Cancer Institute or Brigham and Women's Institutional Review Boards. Informed consent was obtained from all patients and healthy volunteers in accordance with the Declaration of Helsinki.

TE-bone

Porous, aqueous 8% (wt/wt) silk fibroin scaffolds were made following the silk processing steps previously described[19] but were specifically designed with pores of 500 to 600 μm and cut into cylinders (5-mm × 3-mm height). Scaffolds were autoclaved for sterilization and soaked in media containing 10% fetal bovine serum 1 day before seeding. 1×10^6 MSCs were seeded onto scaffolds in regular MSC culture media and grown for 1 day, and then changed to osteogenic media. Osteogenic media consisted of α modified Eagle medium (αMEM) supplemented with 10% FBS, 100 U/mL penicillin, 10 μg/mL streptomycin (Invitrogen), 2 mmol/L L-glutamine (Invitrogen), 0.05 mM ascorbic acid, 100 nM dexamethasone, and 10 mM β-glycerophosphate. When cultured with MM1S (or without but used as controls for coculture studies), dexamethasone was excluded from the media.

Cell culture

The human multiple myeloma cell line MM1S was purchased from ATCC (American Type Culture Collection), engineered to express green fluorescent protein (GFP) and firefly luciferase (Luc^+/GFP^+ MM1S cells) as previously described,[20] and was cultured in 500 μg/mL geneticin (Invitrogen) for selection. OPM2 MM cells were labeled with red fluorescent protein (RFP) and firefly luciferase and provided by Dr Andrew Kung, Columbia University. Primary human BM–derived MSCs obtained from normal healthy subjects (ND-MSCs) or MM patients (MM-MSCs) were isolated and cultured as previously described[21] in expansion media of Dulbecco's modified Eagle medium (DMEM)+20% FBS and used at passages 2 to 4. Clinical samples were collected from patients or healthy donors from the Dana-Farber Cancer Institute and Brigham and Women's Hospital. Primary patient samples were isolated from MM patient BM aspirates using MACS technology (Miltenyi Biotec) with beads for CD138 as recommended by the manufacturer, and the negative fraction was seeded to flasks and grown as previously described to isolate BM-MSCs.[21] For imaging assays, MSCs were labeled with either the Celltracker dye DiD (Invitrogen) or calcein for live-cell imaging (Invitrogen), or they were stably transfected with the TurboRFP gene (Thermo Scientific) subcloned into pCW307 lentivirus vector (Addgene). Primary patient myeloma cells and MSCs were cocultured in "50-50" medium: a base of 50-50 F12-DMEM (Invitrogen) supplemented with 10% FBS, 100 U/mL penicillin, 10 μg/mL streptomycin (Invitrogen), and 2 mmol/L L-glutamine (Invitrogen). RFP-labeled HUVECS (RFP-HUVECS) were purchased from Angioproteomie and expanded in Endothelial Medium (EGM-2 BulletKit media; Lonza). All experiments were performed at 37°C, 5% CO_2 in normoxia.

3D scaffold coculture

Fluorescent (TurboRFP or DiD^+) MSCs were seeded onto scaffolds as described.[19] 1×10^6 MSCs were seeded in MSC growth media 1 day before seeding with 1×10^6 GFP^+MM1S cells. GFP^+MM1S cells alone, MSCs alone, or cocultures of $MSCs^+$ GFP^+MM1S cells were cultured on 3D silk scaffolds in dexamethasone-free osteogenic media for the duration of the coculture experiments. Cells were monitored using confocal microscopy and isolated using fluorescent-activated cell sorting (FACS) or were fixed for histology. Primary patient MM cells were labeled with the lipophilic CellTracker dye (DiI, Invitrogen) and seeded onto scaffolds (0.5×10^6/scaffold) that had been preseeded (1 day prior) with MSCs (1×10^6) labeled with a different cell-tracker dye (DiD; Invitrogen), and cultured at 37°C, 5% CO_2. For endothelial cocultures, RFP-HUVECs were cultured with or without GFP^+MM1S cells in HUVEC media and imaged using confocal microscopy over 1 month.

Drug resistance

For 3D assays, scaffolds with MSCs, GFP^+MM1S cells, or cocultures were cultured on scaffolds in 50-50 media with or without 5 nM bortezomib (Selleck). Bortezomib was diluted in dimethylsulfoxide and stored at −20°C until use, and was then diluted in culture medium immediately before use. Scaffolds were seeded with 0.5×10^6 MSCs per scaffold and 0.5×10^6 GFP^+Luc^+MM1S cells per scaffold the following day, and 50-50 media with or without bortezomib was added immediately before use and changed twice per week. For 2D assays, 0.5×10^4 GFP^+Luc^+ MM1S cells were seeded into 96-well plates with or without a confluent layer of ND-MSCs and cultured with or without media containing 5 nM bortezomib. Cells were quantified using bioluminescence imaging (BLI) and imaged with confocal microscopy.

Fluorescent microscopy

For imaging of MSCs on scaffolds, cells were labeled for live-dead staining with calcein or the LIVE/DEAD Fixable Red Dead Cell Stain Kit (Invitrogen) following the manufacturer's instructions. For cocultures of GFP^+MM1S and MSCs, scaffolds were nondestructively imaged weekly, using 24-well glass-bottomed dishes (1.5 mm; MatTek) with a Leica SP5X Laser Scanning Confocal Microscope using Leica LAS acquisition software. Scaffolds were imaged with 10× dry, 20× water immersion, or 63X Plan Apo objectives using 488 nm Argon, 405 nm UV diode, or white light lasers (470-670 nm). Photomultiplier tubes collected fluorescence signal from autofluorescent scaffolds (405 nm/420-440 nm), GFP^+MM1S (488 nm/500-520 nm), calcein (493/509-525), DiI (552/563-573 nm), DiD (647/660-685nm), DiR (750/775-825), TurboRFP-MSCs (553/564-616 nm), and RFP-HUVECs (555/576-619 nm), which were given pseudocolors as described. Z-stack

From www.bloodjournal.org by guest on January 2, 2015. For personal use only.

images were acquired and processed using LeicaLite or LeicaLAS software to create single maximum projection 3D-like images or videos. Non-confocal fluorescent microscopy was performed using an Olympus CKX41 microscope with appropriate filter cubes and an Olympus DP72 Camera and dry ×10 or ×20 objectives.

Bioluminescence imaging quantification

GFP^+Luc^+MM1S cells or scaffolds seeded with GFP^+Luc^+MM1S cells were measured for bioluminescent signal after placement into opaque, white 96-well plates with 100 μL of media and 5 μL sterile firefly D-luciferin (7.5 mg/mL) (Caliper). After incubation for 5 minutes at 37°C, the signal from MM1S cells was measured on a FLUOstar Optima plate reader.

Histology, immunohistochemistry, and alizarin red staining

Scaffolds were fixed in 4% paraformaldehyde (PFA) overnight at 4°C, paraffin-embedded, sectioned onto glass slides, and stained with alizarin red, hematoxylin and eosin (H&E), or anti-human CD138 immunohistochemistry (primary antibody,#M7228; Dako) by the Dana-Farber Cancer Institute Specialized Histopathology Core. Immunohistochemistry was run at a 1:50 dilution and stained on Leica's Bond-III autostainer using a Leica Bond Polymer Refine Detection kit. Slides were antigen-retrieved using Epitope Retrieval I (Leica) for 30 minutes. For alizarin red staining, MSCs differentiated in osteogenic media (or osteogenic dexamethasone-free media in studies with GFP^+MM1S) were fixed for 15 minutes in 1% formaldehyde, rinsed with water, stained with Alizarin Red Solution (Sigma-Aldrich) (2% wt/vol, 4.2 pH) for 10 minutes, rinsed 3 times with water, and then imaged. Staining was quantified by dissolving Alizarin Red Solution stain from wells in 6-well plates in 1 mL of decalcification solution (Cal-EX Decalcifier; Fisher Scientific) and reading absorbance of the solution at 405 nm (200 μL per well, 96-well plates in a FLUOstar Optima plate reader).

Scanning electron microscopy and micro–computed tomography

Scanning electron microscopy images of scaffolds were taken on a Nikon Eclipse 80i microscope with a DSFi1 Nikon Color Camera with NIS Elements AR Software. Scanning electron microscopy was done using a JEOL scanning electron microscope with gold sputter coating on scaffolds after fixation in 4% PFA. Microcomputed tomography (μCT) imaging was performed on scaffolds fixed overnight in 4% PFA and transferred to 70% ethanol in 1.5 mL Eppendorf tubes on a Siemens Inveon multimodality machine (positron emission tomography–single-photon emission tomography–μCT) at the Dana-Farber Cancer Institute Lurie Imaging Facility Core.

Cell counting

MM-MSCs (n = 4 donors) and ND-MSCs (n = 4 donors) were seeded to 12-well plates (5000 stromal cells/cm^2) with or without GFP^+MM1S (1250 MM1S cells/cm^2) and cultured for 9 days in 50-50 culture media. Cells were then fixed and stained with a 10% neutral-buffered formalin, 1 μg/mL Hoechst (Invitrogen) solution for 10 minutes, and photographed (at least 3 representative fields of view/well) using brightfield and fluorescent (UV filter) microscopy with a Nikon Eclipse 80i microscope (20×), a DSFi1 Nikon Color Camera, and an NIS Elements AR Software, and then counted by a blinded investigator using the ImageJ Cell Counter plugin (v1.47). The mean number of cells/cm^2 ± standard error of the mean (SEM) was calculated and graphed.

Matrigel and fibrin-hydrogel culture

Fibrinogen (Sigma-Aldrich) and thrombin (human BioUltra recombinant, Sigma-Aldrich) were mixed to create 4-mg/mL fibrin hydrogels. Matrigel (BD Biosciences) was diluted 1:3 in phosphate-buffered saline. Both hydrogels were immediately mixed with cells (cell tracker dye DiR^+MSCs, RFP^+HUVECs, GFP^+MM1S cells, or a combination) before seeding into 96-well plates (20 000 cells/well in 100 μL) and were cultured and imaged with fluorescent confocal microscopy over 12 days.

mRNA and miR isolation and qRT-PCR

miRNAs and mRNAs were isolated from cells using the miRNeasy isolation mini-kit (Qiagen), quantified, and tested for quality and contamination using a Nanodrop machine (ThermoScientific),[21] and then subjected to quality control minimum standards of 260/230 > 2 and 260/280 > 1.8 before further use for quantitative reverse-transcriptase polymerase chain reaction (qRT-PCR) or nanoString analysis. For qRT-PCR, sample mRNA was reverse-transcribed into cDNA for either miR using the High Capacity cDNA Reverse Transcription Kit (Invitrogen) or for mRNA using SuperScript III First-String SuperMix (Invitrogen), according to the manufacturer's instructions. qRT-PCR was performed using SYBR Master Mix (SA Bioscience). Analysis was done using the $2^{-\Delta\Delta Ct}$ method, normalized to RNU6B (miR) or glyceraldehyde 3-phosphate dehydrogenase (GAPDH) (mRNA). Primers were designed using the method at http://primerdepot.nci.nih.gov (2013), shown in supplemental Table 1 available on the *Blood* Web site. miR stem-loop sequences were defined using miRBase Sequence Database Release 20 (http://www.mirbase.org). Experiments were performed in a StepOnePlus Real-Time PCR System (Applied Biosystems, Foster City, CA) and consisted of an initial denaturation step of 10 minutes at 95°C, followed by 50 cycles of 95°C for 15 seconds and 60°C for 60 seconds. Data were analyzed with StepOne Software v2.1 (Applied Biosystems), which provides a threshold cycle value that was considered as the cycle in which the fluorescence begins to be distinguished from the background. All PCR reactions were run on an Applied Biosystems AB7500 Real Time PCR system using technical triplicates and were plotted as means of at least 3 different donors ± SEM.

mRNA and miR nanoString profiling

For miR and mRNA profiling, MSC mRNA (from normal or myeloma donors) or miRNA (from normal or myeloma donors or from MSCs after 2 weeks of culture in the 3D model alone or with GFP^+MM1S) was analyzed using the nanoString platform. Expression levels from the nanoString cancer gene reference code set (nCounter GX Human Cancer Reference Kit) containing 230 cancer-associated mRNAs were compared between ND-MSCs and MM-MSCs (5 donors each) normalized to the average of 6 housekeeping genes (*PGK1*, *TUBB*, *CLTC*, *GAPDH*, *GUSB*, and *HPRT1*), graphed as heat maps, and analyzed using dChip software (DNA-Chip Analyzer; Cheng Li and Wing Wong Labs, http://www.hsph.harvard.edu/cli/complab/dchip/ [2013]; >1.5-fold change (fc) and $P < .05$ required for significance). For miRNA expression analysis of the 3D model system, 5 normal stroma cultured alone or in coculture with MM1S myeloma cells, isolated by FACS after 2 weeks of coculture, were analyzed and compared with clinical samples, (3 ND-MSC and 7 MM-MSC samples analyzed at passage 2). Primary samples (normal donor or myeloma patient) and 3D model samples (coculture vs alone) were both analyzed for stromal cell expression of 800 miRNAs using the nanoString miR analysis platform (nCounter human miRNA Expression Assay) following the manufacturer's protocol. Briefly, default settings for quality control on miR samples were used to assure high-quality miR and accuracy of the experimental process for 4 parameters (imaging, binding density, positive control linearity, and control limit of detection). A total of 100 ng of mRNA and miR was used as input into the sample preparation reaction for the nanoString nCounter assay. The miRNAs were all then normalized to the top 100 miRs per sample (by averaging the expression of the top 100 miR per sample, and then dividing all miR by this number), filtered for miRs with an average of >25 counts (cutoff in nanoString units of expression to establish real expression) and considered significant for $P < .05$ using dChip software analysis, following the manufacturer's instructions and previously reported literature.[22] An abundance of specific target molecules was quantified robotically on the nCounter Digital Analyzer by counting the individual fluorescent barcodes and assessing the target molecules on the sample cartridge with a charge-coupled device camera as reported previously.[22] For each assay, a high-density scan setting encompassing 600 fields of view was used. miRs reaching a minimum threshold of 25 counts, fc of >1.5, and significance of $P < .05$ were identified as significant and were further investigated in miR mimic assays.

From www.bloodjournal.org by guest on January 2, 2015. For personal use only.

miR transfection

MM-MSCs were transfected with miR-199a-3p and miR-199a-5p miR *mir*Vana mimics (Ambion) and a negative control (*mir*Vana negative control mimic #1) or miRCURY (Exiqon) inhibitors for miR-181a-5p, miR181c-5p, miR-222-3p, miR-601, miR-146a-5p, and miRCURY negative control, following the manufacturer's instructions. MSCs were cultured until they were 80% confluent and were then transfected with a final concentration of 30 nM of each miR mimic or 50 nM of each miRCURY Inhibitor for 24 hours using Lipofectamine 2000 (Invitrogen). Alizarin Red Solution staining and qRT-PCR were performed on samples after 10 days of culture in osteogenic (dexamethasone-free) media. Efficiency of transfection was validated by qRT-PCR for detection of miR levels at 24 hours and 10 days as previously described.[21]

Pathway enrichment analysis

The targets of miR-199a-5p were predicted by TargetScan[23] and retrieved from online (http://www.targetscan.org/). We used pathways derived from 3 databases—BioCarta, KEGG, and Reactome—which were downloaded from MSigDB.[24] Hypergeometric testing was used to assess the enrichment of pathways. The enrichment *P* values were adjusted to account for multiple testing, resulting in a false discovery rate for each pathway,[25] and pathways were identified using a false discovery rate cutoff of 10%.

Statistics

Statistical analysis was performed using GraphPad/Prism Version 6.02 or Microsoft Excel. *P* values are based on Student's *t* tests (2-tailed) for 2-way comparisons, or analysis of variance (ANOVA) for multiple hypothesis testing using post hoc Dunnett (2-way ANOVA) or Fisher least significant difference (LSD) (1-way ANOVA) multiple comparison testing. Sample variance was determined using an F-Test, and normality was determined using a Normal Quantile Plot to test for non-normality (Q–Q probability plot). $P < .05$ was considered significant and *P* values are provided in the figures or their captions. Statistics for heat maps were done using dChip software using $P < .05$ as significant.

Results

We first developed our TE-bone model and characterized its unique ability to represent a mineralized 3D bone matrix, not afforded by any previously described model. Silk scaffolds, which recapitulate the high-compressive strength and porous nature of the BM trabecula,[26] were seeded with ND-MSCs and differentiated into TE-bone using osteogenic media for 50 days. The TE-bone samples formed dense, calcified tissue, as demonstrated by μCT imaging (supplemental Figure 1A), scanning electron microscopy (supplemental Figure 1B), and nondestructive fluorescence confocal microscopy (Figure 1A). This 3D mineralized model served as a basis to begin studying osteogenesis in the context of myeloma.

Next we tested the ability of myeloma cells to grow in osteogenic media, which would be required in coculture. However, we found dexamethasone to be toxic to both MM1S and OPM2 cells (data not shown) and hence adapted the osteogenic media for our purposes by removing dexamethasone, an alteration that has been previously described.[27] We next tested the ability for OPM2 and MM1S cell lines to grow on the silk scaffolds and found that, although both cell types were able to adhere to ND-MSCs seeded on scaffolds, only MM1S could adhere to the silk scaffolds alone, as observed in confocal imaging (data not shown). Hence for subsequent studies we chose to use MM1S as the main myeloma cell line for this model.

We hypothesized that silk scaffolds would provide a more realistic platform to investigate endothelial cell–myeloma cell interactions in the bone marrow, so we compared coculture responses of these cells in 3D silk scaffolds and hydrogels. We cocultured fluorescent endothelial cells (RFP^+HUVECs) with GFP^+MM1S cells and observed cell-to-cell contact and interaction, as well as interesting assembly patterns unique to silk scaffold culture (Figure 1B, supplemental Figure 2A, and supplemental Video 1). Samples were imaged with confocal microscopy over 18 days and demonstrated GFP^+MM1S cell adherence to RFP^+HUVECs and incorporation into the capillary-like HUVEC structures. Myeloma cells also appeared to support the branching, tube-shaped formations of HUVECs (with observable lumens), which were not observed in HUVEC monocultures. GFP^+MM1S cells clumped and colocalized at endothelial protrusions, perhaps mimicking some of the signaling and evolution of angiogenesis within bone tumors. Interestingly, GFP^+MM1S cell association with endothelial cells in a tubelike formation may model the early stages of myeloma cell intravasation and extravasation, as well as contributions toward angiogenesis. None of these phenomena were observed in 3D fibrin hydrogel or Matrigel cultures (supplemental Figure 2B), supporting validation that the stiffer scaffold substrate more accurately recapitulates the in vivo conditions than do softer substrates.

The 3D silk scaffold model also recapitulated the ability for MSCs to protect GFP^+MM1S cells from therapeutic agents such as bortezomib over a 30-day treatment period, as quantified with bioluminescent imaging (supplemental Figure 3A) and imaged with confocal microscopy (Figure 1C). This was not achieved in 2D culture (supplemental Figure 3B), defining the 3D system as a unique environment suitable for long-term drug studies. Similarly, in vitro growth of primary MM tumor cells in 2D lacks the realistic complexity of a 3D milieu, explaining why primary patient MM cell growth was observed on MSC-seeded scaffolds over 11 days but was not possible under the same conditions in 2D culture.[28] Primary MM cells were labeled with cell-tracker dyes and imaged with confocal microscopy using calcein to assess cell viability (Figure 1D and supplemental Figures 4 and 5). They were further identified with H&E and human-CD138 stains on fixed scaffold samples to ensure plasma cell identity (supplemental Figure 6). Together, these findings indicate that our 3D BM model allows for cancer-bone modeling in a more biologically relevant system than does 2D culture or soft 3D culture.

To address the study of myeloma-induced osteogenesis inhibition, we first confirmed prior reports[8] that proliferation and osteogenesis are significantly inhibited by myeloma in clinical samples (MM-MSCs vs ND-MSCs) and in vitro 2D cocultures of ND-MSCs and myeloma cells (supplemental Figures 7 and 8). We also assessed the mRNA profile of clinical samples (ND-MSCs and MM-MSCs) by analyzing 230 mRNAs involved in cell proliferation, differentiation, migration, and other vital signaling. Unsupervised analysis demonstrated distinct clustering between ND-MSCs and MM-MSCs, confirming inherent differences between normal and myeloma stroma (supplemental Figure 9A). Forty-nine mRNAs were found to have significantly different expression between ND-MSCs and MM-MSCs ($P < .05$, 1.5-fc; supplemental Figure 9B), including the cell-cycle regulators CDKN2A (p16, previously reported[29]) and CDKN1A (p21, not previously reported), which may contribute to the decreased MM-MSC proliferation, and Collage1A1, likely contributing to decreased bone matrix formation.

We then attempted to model inhibited osteogenesis of MSCs in our 3D BM model. ND-MSCs and GFP^+MM1S were cultured alone or together on scaffolds in osteogenic media over 5 weeks. Confocal and fluorescent microscopy showed that GFP^+MM1S cells inhibited ND-MSC proliferation, migration, and tissue production in scaffolds (Figure 2A-B and supplemental Videos 2 and 3). Alizarin Red Solution and H&E staining histology of scaffolds after 5 weeks

From www.bloodjournal.org by guest on January 2, 2015. For personal use only.

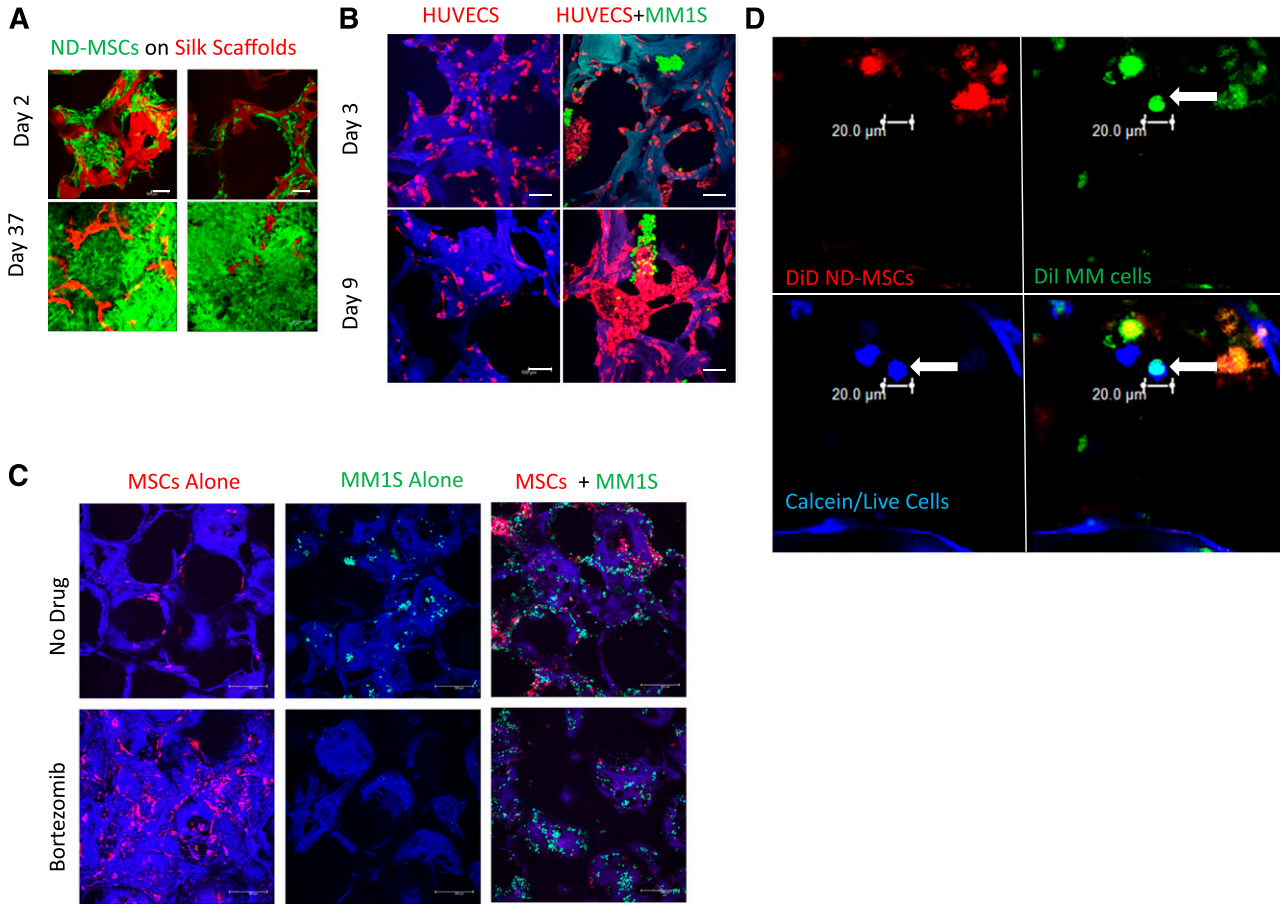

Figure 1. Development of an in vitro 3D BM niche model. (A) Confocal images of calcein-labeled ND-MSCs, passage 2, (calcein/live cells, green; silk scaffold, red) at 2 and 37 days of culture in osteogenic media. The scale bar represents 100 μm. (B) Confocal images of RFP$^+$HUVECs (red) ± GFP$^+$MM1S cells (green) on scaffolds (blue) (days 3 and 9; scale bar = 100 μm). Representative image of 3 experiments is shown here, cultured in endothelial growth media. (C) Confocal images at day 30 of culture of GFP$^+$MM1S alone (left, green), DiD-labeled MSCs alone (middle, red), and cocultures (right) in 50-50 medium with bortezomib (top, 5 nM) or without bortezomib (bottom) on autofluorescent scaffolds (blue). (Scale bar = 100 μm.) (D) Confocal images of primary patient CD138$^+$ MM cells (green with DiI) at day 7 seeded onto ND-MSCs (red with DiD). Channels show the myeloma cell (arrow) as alive (calcein$^+$, blue), DiI$^+$ (green), and DiD$^-$ (red). Overlay of green and blue appears cyan and demonstrates colocalization of calcein and DiI staining. Samples cultured in 50-50 media (n = 3); the scale bar represents 20 μm.

demonstrated cellular tissue formation and mineralization in ND-MSC samples grown alone. Conversely, a lack of mineralization, as well as poor tissue formation and decreased cell numbers, were observed in samples of ND-MSCs cocultured with MM1S cells (Figure 2C). Interestingly, by week 2 the inhibition of MSC growth was evident in confocal imaging, and this trend continued over the full 5-week period, whereas MSCs alone proliferated, filled in scaffold pores, and formed mineralized, TE-bone. In sum, this system is useful for investigating myeloma effects on 3D osteogenesis in a more realistic setting than in 2D.

We then investigated the role of miRs in the dysfunctional osteogenesis of MSCs cultured with myeloma cells. TurboRFP$^+$ ND-MSCs were cultured alone or with GFP$^+$MM1S cells in the 3D model in osteogenic media for 2 weeks, sorted and collected using FACS, and analyzed for miR changes (coculture vs monoculture) using nanoString analysis of 800 miRs. Fifty-three miRs (28 up- and 25 downregulated) showed significantly altered expression in MSCs during coculture with MM1S (Figure 3A and supplemental Table 2). To compare with clinical samples, miR profiling was also performed on BM stroma samples from normal, healthy donor or myeloma patients. These samples demonstrated 41 miRs (34 up- and 7 downregulated) with significantly altered expression in MSCs from myeloma patient donors (MM) vs normal donor MSCs (ND) (Figure 3B and supplemental Table 2). Of these, six were found to be similarly downregulated (1 miR) or upregulated (5 miRs) in the 3D coculture system in the 3D model compared with the clinical samples (Table 1). The correlation between the patient and normal samples, and the BM niche 3D model contributes additional evidence that our system can reliably recapitulate many of the in vivo effects of MM cells on MSCs and suggests miRs that may govern the inhibited osteogenesis seen in patient MSCs. All miR data can be found in the GEO database under accession number GSE60423.

Finally, we examined whether any of the 6 miRs identified in the 3D model and in the clinical samples could serve as targets for inducing osteogenesis. Inhibition of miRs overexpressed in MM-MSCs (miR-181a-5p, miR181c-5p, miR-222-3p, miR-601, miR-146a-5p) using miRCURY inhibitors did not alter the mineralization potential of MM-MSCs as assessed by Alizarin Red Solution (data not shown) and hence were not further pursued. However, increasing the expression of miR-199a-5p significantly increased mineralized matrix production, indicative of osteogenic potential, and further supported the function of miR-199a as an osteogenic-promoting miR (Figure 3C-D). Using miR mimic transfection in ND-MSCs and MM-MSCs, we increased expression of miR-199a and observed that increasing the expression of both miR-199a-5p and miR-199a-3p in MM-MSCs significantly increased expression of several common osteogenic markers previously described,[30] namely, alkaline phosphatase, integrin-binding sialoprotein, collagen type I α 1, osteopontin,

From www.bloodjournal.org by guest on January 2, 2015. For personal use only.

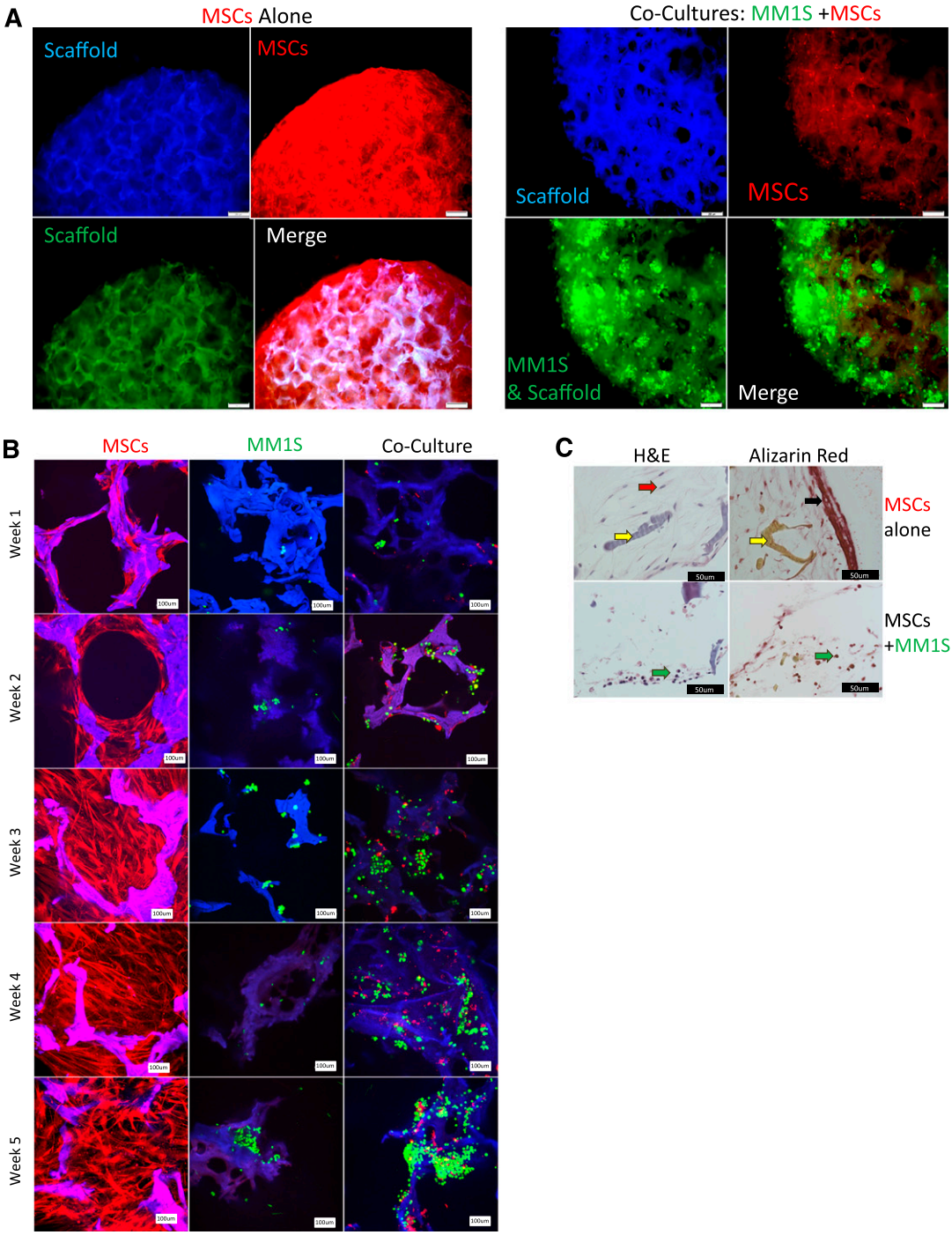

Figure 2. Inhibited osteogenesis induced by myeloma in a 3D bone model. (A) Fluorescent imaging at week 5 (TurboRFP$^+$MSCs, red; GFP$^+$MM1S, green; scaffold, blue). Overlaid channels (merge) shows increased pore infiltration, elongation, and proliferation by MSCs when grown in the absence of myeloma cells (left) compared with when grown with MM1S (right). The scale bar represents 200 μm. (B) Confocal images of TurboRFP$^+$MSCs (red) and GFP$^+$MM1S (green), alone or in coculture, on silk scaffolds (blue) from 1 to 5 weeks of culture in osteogenic media. The scale bar represents 100 μm. (C) Histologic analysis of scaffolds after 5 weeks of osteogenesis for MSCs alone (top) or in coculture with GFP$^+$MM1S (bottom) stained for mineralization (Alizarin Red, right) or hematoxylin and eosin (H&E) (left). Black arrow indicates mineralization found only in MSCs cultured alone. Yellow arrows indicate silk scaffold. Red arrow indicates stromal cells, which are found throughout the MSC alone samples and sparsely through coculture samples. Green arrows indicate MM1S plasma cells found only in coculture samples. The scale bar represents 50 μm.

osteocalcin, and runt-related transcription factor 2 (Figure 3E-F and supplemental Figure 10). Similar results were found with transfection of ND-MSCs with miR-199a-3p and 199a-5p mimics (data not shown).

To explore the potential pathways regulated by hsa-miR-199a-5p, we performed a pathway enrichment analysis of its predicted target genes. Analysis of miR-199a-5p targets revealed 19 pathways that were significantly enriched (supplemental Table 3). Interestingly, among them the ErbB signaling pathway was identified and is also reported to be involved in osteogenesis.[31,32] The MAPK signaling pathway was also identified by us, as well as by others,[33] as an miR199a-5p target pathway, and has been shown to play a role in osteogenic differentiation via the ErbB1 and ErbB2 pathways.[34] Moreover, 3 pathways centered on semaphorins were also identified

From www.bloodjournal.org by guest on January 2, 2015. For personal use only.

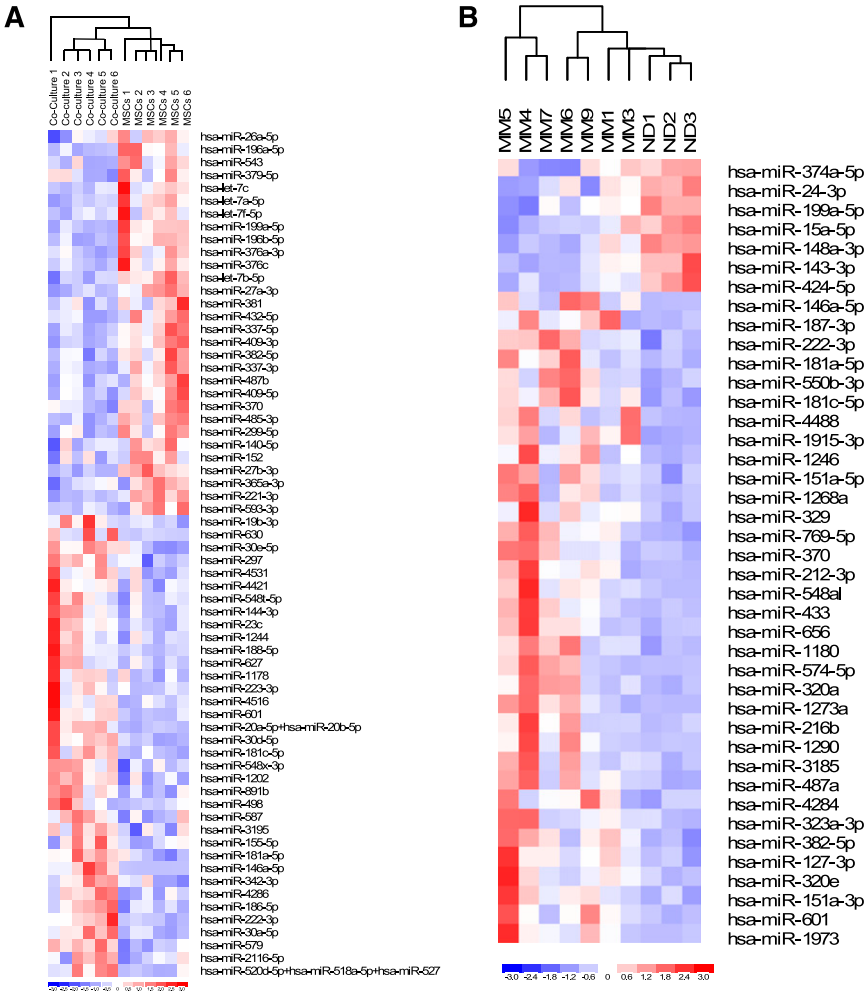

Figure 3. Alterations in MSC miRs in 3D modeling and patient vs normal data, and the resulting changes in MSCs after mimic-induced increased expression of miR-199a. (A) Heat map of the 53 mRNAs identified from nanoString analysis from the 3D model samples that are significantly different between cocultured (Co-culture) and monocultured ND-MSCs (MSCs). Filtering was done on original 800 miRs based on high expression (>25 average counts), significance between myeloma vs normal donor groups ($P < .05$), and high fc threshold (fc >1.5). (B) Heat map of 41 miRs identified from nanoString analysis that are significantly different between patient samples (myeloma [MM] and normal donor [ND] sample MSCs). Filtering was done on original 800 miRs based on high expression (>25 average counts), with significance between myeloma vs normal donor groups ($P < .05$), and high fc threshold (fc >1.5). (C) Alizarin Red staining quantification of mineralization produced by MSCs transfected with negative control mimic or miR-199a-5p mimic after 10 days in osteogenic no-dexamethasone media. Data plotted as mean ±SEM, n ≥3 different donors. (D) Alizarin Red staining representative images showing mineralization of MM-MSCs in 6-well plates transfected with negative control mimics or miR-199a-5p mimics to increase miR-199a-5p expression after 10 days in osteogenic no-dexamethasone media. Images are representative of n ≥3 different donors. The scale bars represent 200μm (original magnification ×4), 100 μm (×10), 50 μm (×20), and 20 μm (×40). (E) MM-MSCs transfected to increase expression of miR-199a-3p (E) or 199a-5p (F) demonstrate increased expression of osteogenic markers after 10 days of culture, measured by q-RT-PCR, gene expression normalized to negative control (Control) for each gene. ALPL, alkaline phosphatase; BSP, integrin-binding sialoprotein; Col1a1, collagen type I α 1; OP, osteopontin; OC, osteocalcin; RUNX2, runt-related transcription factor 2. Data plotted as mean ± SEM and analyzed with 1-way ANOVA and a post hoc Fisher least significance difference test for multiple comparisons (each gene vs negative control). Day 10 after transfection with miR mimics or controls and grown in osteogenic-no dexamethasone medium. n ≥ 3 different donors, $^{**}P < .05$, $^{**}P < .01$.

and may play a role in osteogenesis formation,[35,36] although this is currently not well-defined.[37] Hence, the pathways identified here may explain the mechanisms by which miR199a-5p regulates mRNAs that have anti-osteogenic effects (such as semaphorin4D) and may suggest novel pathways that could be targeted to normalize the osteogenic differentiation of MM-MSCs.

Discussion

3D culture models with material properties similar to those found in vivo are materializing as essential tools in cancer biology, owing to their ability to replicate tissue- or organ-specific structural features, biomechanical properties, and cell-cell or cell–extracellular matrix interactions more accurately than conventional 2D culture. Our new preclinical bone cancer model has the capacity to support long-term culture and imaging for expansion of primary myeloma cells, high-throughput drug screening, vessel formation, and osteogenesis in the presence of cancer. Prior published models have used soft, hydrogel matrices that cannot be mineralized and therefore cannot mimic the bone microenvironment.[3,4] Our 3D model uses silk protein–based scaffolds that allow for active cell attachment and adherence to scaffolds rather than passive encapsulation in 3D hydrogel cultures. In addition, the tissue-engineering approach represents a more controllable model compared with culturing whole-patient bone biopsies,[6] because it allows for user-designed introduction of cells of interest, increasing the reproducibility, adaptability, and scalability of the model. Therefore, the silk-based 3D TE-bone model presented herein represents a unique model to examine the interactions of bone and cancer cells in a 3D microenvironment, with mechanical properties similar to bone.

It remains to be determined why a decrease in certain miRs may lead to inhibited osteogenesis in myeloma and what mRNA targets drive this, but it is evident that overexpressing certain miRs within MSCs can increase their osteogenic potential, and our 3D model helped to identify 199a-5p as one such miR. MiR-199a has been described as "flexible and versatile as a chameleon,"[33] because it has a wide variety of important functions across many cell types and systems. In terms of osteogenesis, miR-199a-5p specifically has been shown to have a pro–stem cell differentiation effect in BM-derived human MSCs both in vitro and in vivo, whereas inhibition with siRNAs blocking miR-199a-5p reduced osteogenesis of hMSCs.[38,39] Pathways implicated in this are still uncertain but include HIF1a, TWIST, NADPH-oxidase, PI-3 kinase, mitogen-activated protein kinase, and NF-κB pathways, which are being investigated for their roles in osteogenesis.[38,40] miR-199a is also a BMP2-responsive miR,[41] suggesting that altered BMP2 signaling may be involved in the observed effects of these miRs. Decreased 199a-5p may also increase fibronectin in MM BM, which is elevated in MM patient

From www.bloodjournal.org by guest on January 2, 2015. For personal use only.

Figure 3. Continued.

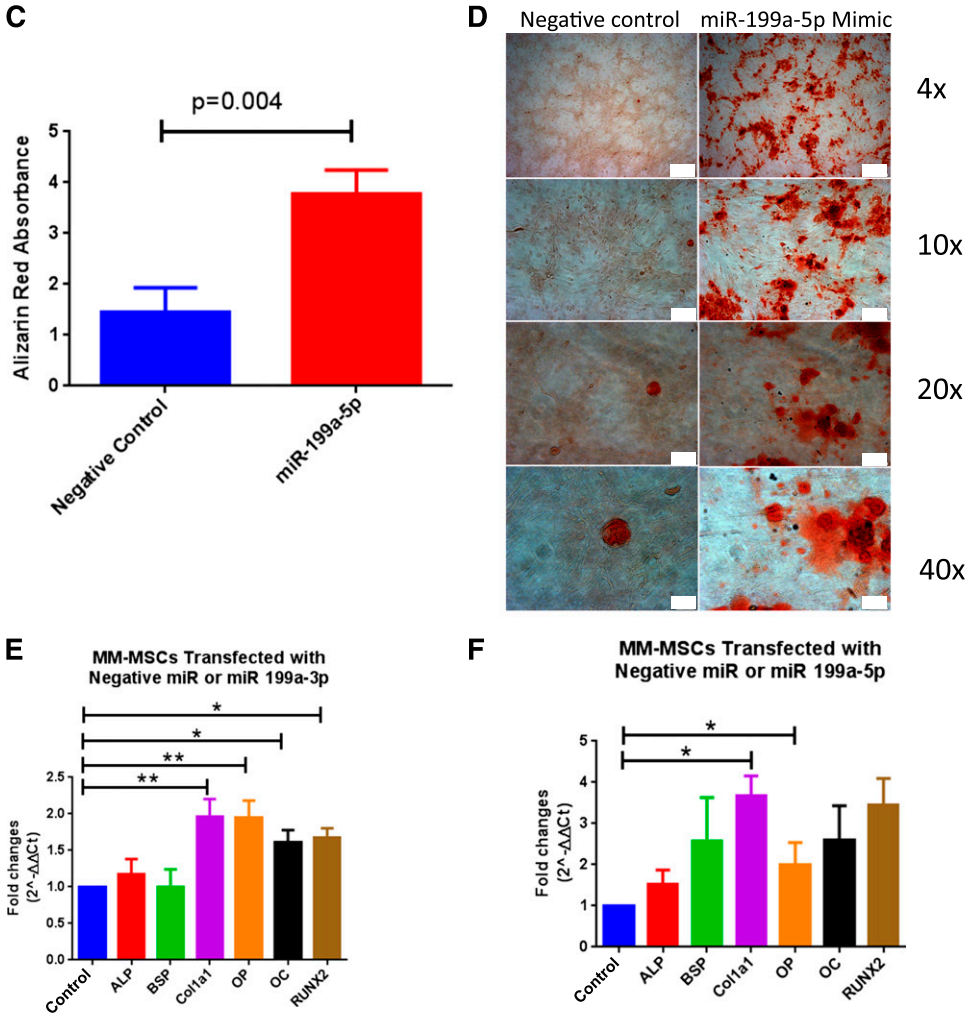

serum[42,43] and has been shown to cause increased MM tumor accumulation within the BM and dictate CAM-DR.[44] Although the exact composition and interaction of mRNAs inhibited by miR-199a appear to be complex, it is clear that miR-199a represents the first miR identified as abnormally downregulated, and one of the first abnormally expressed[45] in bone cancer patients, that may be a therapeutic strategy for enhancing bone formation.

The roles of specific miRs in osteogenesis and MSC-tumor feedback are currently enigmatic,[39,46] but our results suggest that novel target miRs are useful for reactivating the osteogenic abilities of cancer-associated MSCs. Targeting these miRs may provide a new avenue for healing lesions and reversing the osteolytic cancer cycle in myeloma along with other osteotropic cancers. In conclusion, the novel 3D, in vitro bone cancer model developed provides a physiologically relevant platform to investigate osteogenesis, angiogenesis, and cancer growth, as well as drug response with primary samples and cell lines. It allows for nondestructive imaging over long periods and can be used for testing a multitude of other bone cancer hypotheses and modeling an array of biological processes involved in the inhibited osteogenesis of cancer-colonized bones. More broadly, many researchers would likely increase their in vivo success rates by first testing their hypotheses in our 3D model system. Our

Table 1. MicroRNAs altered in MSCs by myeloma

miR name	Fc, 3D model (MSCs in coculture with MM1S vs alone)	*P* value, 3D model (MSCs in coculture with MM1S vs alone)	Fc, MM vs ND MSCs	*P* value, MM vs ND MSCs
hsa-miR-199a-5p	–2.019	.00086974	–1.917	.00115665
hsa-miR-181a-5p	1.771	.00362835	3.190	.02106839
hsa-miR-181c-5p	2.135	.00276756	3.078	.00192591
hsa-miR-222-3p	2.152	.00332040	1.821	.01680615
hsa-miR-601	2.546	.00738047	3.637	.02449335
hsa-miR-146a-5p	17.175	.00405939	15.353	.02622689

Six miRs were found to be similarly upregulated (5 miRs) or downregulated (1 miRs) in the 3D system (MSCs cocultured with GFP$^+$MM1S vs MSCs alone, after 2 weeks in coculture in osteogenic, no-dexamethasone media) and in patient vs normal samples (MM patient MSCs vs normal donor MSCs). Fc $\geq$1.5, $P < .05$, n $\geq$3, 2-tailed Student's *t* test, average expression >25 nanoString counts.

From www.bloodjournal.org by guest on January 2, 2015. For personal use only.

model allows biological questions to be investigated, compounds to be screened, and novel targets or therapeutics to be identified more quickly and cheaply and in a more realistic 3D BM niche setting than is currently available. Resulting research will be more clinically translatable and will advance more quickly and efficiently from the bench to the bedside of patients who have bone cancer.

Acknowledgments

The authors thank Lisa Cameron, Grace O'Callaghan, Priya Dhir, Michele Moschetta, Susanna M. Santos, Wenjing Zhang, and Rucsanda Carmen Preda for their assistance.

This study was supported by the Department of Defense, Peer-review Cancer Research Program (W81XWH-13-1-0390), the National Institutes of Health P41 Center (EB002520) and National Cancer Institute grant R01CA154648.

Authorship

Contribution: M.R.R. designed the experiments, performed in vitro studies and data analysis, and wrote the manuscript; Y.M. created RFP-MSCs; YongZ., YuZ., and S.M. assisted with qRT PCR studies; J.E.R., Y.-T.T., A.S., and Y.A. provided primary MSCs or patient data; S.V.G., M.M., and Z.N.L. assisted with in vitro assays, cell culture, and qRT-PCR; J.S. performed microRNA pathway analysis; D.L.K. provided feedback and silk scaffolds; A.M.R. provided scientific assistance and advice; and I.M.G. supervised the project and edited the manuscript.

Conflict-of-interest disclosure: I.M.G. is on the advisory boards of Millennium/Takeda, Novartis, Onyx, and Celgene. All other authors declare no competing financial interests.

Correspondence: Irene M. Ghobrial, Medical Oncology, Dana-Farber Cancer Institute, 450 Brookline Ave, Boston, MA, 02115; e-mail: Irene_ghobrial@dfci.harvard.edu.

References

1. Baker BM, Chen CS. Deconstructing the third dimension: how 3D culture microenvironments alter cellular cues. *J Cell Sci.* 2012;125(Pt 13): 3015-3024.
2. Hughes V. Microenvironment: Neighbourhood watch. *Nature.* 2011;480(7377):S48-S49.
3. Zdzisińska B, Roliński J, Piersiak T, Kandefer-Szerszeń M. A comparison of cytokine production in 2-dimensional and 3-dimensional cultures of bone marrow stromal cells of multiple myeloma patients in response to RPMI8226 myeloma cells. *Folia Histochem Cytobiol.* 2009;47(1):69-74.
4. Kirshner J, Thulien KJ, Martin LD, et al. A unique three-dimensional model for evaluating the impact of therapy on multiple myeloma. *Blood.* 2008; 112(7):2935-2945.
5. Takeuchi K, Abe M, Hiasa M, et al. Tgf-Beta inhibition restores terminal osteoblast differentiation to suppress myeloma growth. *PLoS ONE.* 2010;5(3):e9870.
6. Ferrarini M, Steimberg N, Ponzoni M, et al. Ex-vivo dynamic 3-D culture of human tissues in the RCCS™ bioreactor allows the study of Multiple Myeloma biology and response to therapy. *PLoS ONE.* 2013;8(8):e71613.
7. Roodman GD. Mechanisms of bone metastasis. *N Engl J Med.* 2004;350(16):1655-1664.
8. Reagan MR, Ghobrial IM. Multiple myeloma mesenchymal stem cells: characterization, origin, and tumor-promoting effects. *Clin Cancer Res.* 2012;18(2):342-349.
9. Markovina S, Callander NS, O'Connor SL, et al. Bone marrow stromal cells from multiple myeloma patients uniquely induce bortezomib resistant NF-kappaB activity in myeloma cells. *Mol Cancer.* 2010;9:176.
10. Yaccoby S, Wezeman MJ, Zangari M, et al. Inhibitory effects of osteoblasts and increased bone formation on myeloma in novel culture systems and a myelomatous mouse model. *Haematologica.* 2006;91(2):192-199.
11. Azab AK, Quang P, Azab F, et al. P-selectin glycoprotein ligand regulates the interaction of multiple myeloma cells with the bone marrow microenvironment. *Blood.* 2012;119(6): 1468-1478.
12. Fuhler GM, Baanstra M, Chesik D, et al. Bone marrow stromal cell interaction reduces syndecan-1 expression and induces kinomic changes in myeloma cells. *Exp Cell Res.* 2010; 316(11):1816-1828.
13. Zangari M, Terpos E, Zhan F, Tricot G. Impact of bortezomib on bone health in myeloma: a review of current evidence. *Cancer Treat Rev.* 2012; 38(8):968-980.
14. Pozzi S, Raje N. The role of bisphosphonates in multiple myeloma: mechanisms, side effects, and the future. *Oncologist.* 2011;16(5):651-662.
15. Xu S, Evans H, Buckle C, et al. Impaired osteogenic differentiation of mesenchymal stem cells derived from multiple myeloma patients is associated with a blockade in the deactivation of the Notch signaling pathway. *Leukemia.* 2012; 26(12):2546-2549.
16. Vallet S, Raje N. Bone anabolic agents for the treatment of multiple myeloma. *Cancer Microenviron.* 2011;4(3):339-349.
17. Pennisi A, Ling W, Li X, et al. The ephrinB2/EphB4 axis is dysregulated in osteoprogenitors from myeloma patients and its activation affects myeloma bone disease and tumor growth. *Blood.* 2009;114(9):1803-1812.
18. Croucher PI, Shipman CM, Lippitt J, et al. Osteoprotegerin inhibits the development of osteolytic bone disease in multiple myeloma. *Blood.* 2001;98(13):3534-3540.
19. Reagan MR, Seib FPP, McMillin DW, et al. Stem Cell Implants for Cancer Therapy: TRAIL-Expressing Mesenchymal Stem Cells Target Cancer Cells In Situ. *J Breast Cancer.* 2012;15(3): 273-282.
20. Azab AK, Runnels JM, Pitsillides C, et al. CXCR4 inhibitor AMD3100 disrupts the interaction of multiple myeloma cells with the bone marrow microenvironment and enhances their sensitivity to therapy. *Blood.* 2009;113(18):4341-4351.
21. Roccaro AM, Sacco A, Maiso P, et al. BM mesenchymal stromal cell-derived exosomes facilitate multiple myeloma progression. *J Clin Invest.* 2013;123(4):1542-1555.
22. Marcucci G, Maharry KS, Metzeler KH, et al. Clinical role of microRNAs in cytogenetically normal acute myeloid leukemia: miR-155 upregulation independently identifies high-risk patients. *J Clin Oncol.* 2013;31(17):2086-2093.
23. Lewis BP, Burge CB, Bartel DP. Conserved seed pairing, often flanked by adenosines, indicates that thousands of human genes are microRNA targets. *Cell.* 2005;120(1):15-20.
24. Subramanian A, Tamayo P, Mootha VK, et al. Gene set enrichment analysis: a knowledge-based approach for interpreting genome-wide expression profiles. *Proc Natl Acad Sci USA.* 2005;102(43):15545-15550.
25. Storey JD, Tibshirani R. Statistical significance for genomewide studies. *Proc Natl Acad Sci USA.* 2003;100(16):9440-9445.
26. Mandal BB, Grinberg A, Gil ES, Panilaitis B, Kaplan DL. High-strength silk protein scaffolds for bone repair. *Proc Natl Acad Sci USA.* 2012; 109(20):7699-7704.
27. von Knoch F, Jaquiery C, Kowalsky M, et al. Effects of bisphosphonates on proliferation and osteoblast differentiation of human bone marrow stromal cells. *Biomaterials.* 2005;26(34): 6941-6949.
28. Gu ZJ, De Vos J, Rebouissou C, et al. Agonist anti-gp130 transducer monoclonal antibodies are human myeloma cell survival and growth factors. *Leukemia.* 2000;14(1):188-197.
29. Corre J, Mahtouk K, Attal M, et al. Bone marrow mesenchymal stem cells are abnormal in multiple myeloma. *Leukemia.* 2007;21(5):1079-1088.
30. Lau E, Lee WD, Li J, et al. Effect of low-magnitude, high-frequency vibration on osteogenic differentiation of rat mesenchymal stromal cells. *J Orthop Res.* 2011;29(7): 1075-1080.
31. Jullien N, Maudinet A, Leloutre B, Ringe J, Häupl T, Marie PJ. Downregulation of ErbB3 by Wnt3a contributes to wnt-induced osteoblast differentiation in mesenchymal cells. *J Cell Biochem.* 2012;113(6):2047-2056.
32. Li B, Moshfegh C, Lin Z, Albuschies J, Vogel V. Mesenchymal stem cells exploit extracellular matrix as mechanotransducer. *Sci Rep.* 2013;3: 2425.
33. Gu S, Chan W-Y. Flexible and Versatile as a Chameleon-Sophisticated Functions of microRNA-199a. *Int J Mol Sci.* 2012;13(7): 8449-8466.
34. Tamama K, Kawasaki H, Wells A. Epidermal growth factor (EGF) treatment on multipotential stromal cells (MSCs). Possible enhancement of therapeutic potential of MSC. *J Biomed Biotechnol.* 2010;2010:795385.
35. Wada N, Maeda H, Hasegawa D, et al. Semaphorin 3A induces mesenchymal-stem-like properties in human periodontal ligament cells. *Stem Cells Dev.* 2014. [Epub ahead of print].
36. Hayashi M, Nakashima T, Taniguchi M, Kodama T, Kumanogoh A, Takayanagi H. Osteoprotection by semaphorin 3A. *Nature.* 2012;485(7396): 69-74.

From www.bloodjournal.org by guest on January 2, 2015. For personal use only.

37. Negishi-Koga T, Shinohara M, Komatsu N, et al. Suppression of bone formation by osteoclastic expression of semaphorin 4D. *Nat Med.* 2011; 17(11):1473-1480.

38. Gu S, Chen B, Chen X, et al. Function of miR-199a-5p in stage-specific osteogenesis of human mesenchymal stem cells. 63rd Annual Meeting of the American Society of Human Genetics. 2013.

39. Oskowitz AZ, Lu J, Penfornis P, et al. Human multipotent stromal cells from bone marrow and microRNA: regulation of differentiation and leukemia inhibitory factor expression. *Proc Natl Acad Sci USA.* 2008;105(47):18372-18377.

40. Gonsalves CS, Kalra VK. Hypoxia-mediated expression of 5-lipoxygenase-activating protein involves HIF-1alpha and NF-kappaB and microRNAs 135a and 199a-5p. *J Immunol.* 2010; 184(7):3878-3888.

41. Lin EA, Kong L, Bai X-H, Luan Y, Liu C-J. miR-199a, a bone morphogenic protein 2-responsive MicroRNA, regulates chondrogenesis via direct targeting to Smad1. *J Biol Chem.* 2009;284(17): 11326-11335.

42. Lee DY, Shatseva T, Jeyapalan Z, Du WW, Deng Z, Yang BB. A 3′-untranslated region (3'UTR) induces organ adhesion by regulating miR-199a* functions. *PLoS ONE.* 2009;4(2):e4527.

43. Spira G, Manaster J, Paizi M. The possible role of fibronectin in multiple myeloma. *Int J Clin Lab Res.* 1994;24(1):1-5.

44. Damiano JS, Cress AE, Hazlehurst LA, Shtil AA, Dalton WS. Cell adhesion mediated drug resistance (CAM-DR): role of integrins and resistance to apoptosis in human myeloma cell lines. *Blood.* 1999;93(5):1658-1667.

45. Xu S, Cecilia Santini G, De Veirman K, et al. Upregulation of miR-135b is involved in the impaired osteogenic differentiation of mesenchymal stem cells derived from multiple myeloma patients. *PLoS ONE.* 2013;8(11): e79752.

46. Eskildsen T, Taipaleenmäki H, Stenvang J, et al. MicroRNA-138 regulates osteogenic differentiation of human stromal (mesenchymal) stem cells in vivo. *Proc Natl Acad Sci USA.* 2011; 108(15):6139-6144.

Supplemental Figure, Video and Table Legends

Supplemental Table I. Primers for mRNA and miRNA q-RT-PCR. URP= Universal Reverse Primer used with all microRNAs.

Supplemental Table II. MicroRNAs Altered in MSCs due to influence of Myeloma cells in 3D Model (Co-culture vs Monoculture) and in 2D Cultures (Patient Samples vs Healthy Donors). NanoString counts of microRNAs significantly different in either the 3D culture conditions (left) and in Patient vs Healthy samples (right). 53 miRNAs were found to be significant in 3D co-cultures (MSCs co-cultured with GFP^{+}MM1S vs. MSCs alone, after 2 weeks in co-culture in osteogenic, no-dexamethasone media) and 41 miRs were found to be significant between patient and healthy donor samples (MM patient MSCs vs. normal donor MSCs). Fold changes, $fc \geq 1.5$, $p < 0.05$, $n \geq 3$, 2-tailed T-test, average expression>25 nanoString counts. Downregulated miRs (green background) and Upregulated miRs (red background) from both analyses were compared and six miRs similarly changed in both groups were identified (indicated in bold).

Supplemental Table III. Pathway Analysis of hsa-miR-199a-5p target genes. 19 Pathways were significantly enriched in the miR-199a-5p mRNA pathway analysis. BioCarta, KEGG and Reactome Pathways were screened and hypergeometric testing was used to assess the enrichment of pathways. Enrichment p-values were adjusted to account for multiple testing, resulting in a false discovery rate (FDR) for each pathway, and pathways were identified using an FDR≤10%.

Supplemental Figure 1. Imaging of MSCs Differentiating on Scaffold in Osteogenic, dexamethasone-containing media. (a) microCT image showing mineralization of scaffolds after 50 days of osteogenic differentiation of ND-MSCs. Silk scaffolds alone show no microCT signal. N=5, with representative images shown **(b)** Scanning electron microscopy images of scaffolds at days 2 and 37. Scaffold pores become infiltrated with ND-MSCs and matrix, creating an artificial bone microenvironment. Scale bar= 1 mm. N=4 scaffolds, with representative images shown.

Supplemental Figure 2. Angiogenesis modeling in 3D scaffolds imaged with Confocal Microscopy. (a) RFP^+HUVECs (red), GFP^+MM1S (green) and silk scaffolds (blue) are shown in mono-culture and co-culture at days 3, 9, 14, 18 in endothelial cell medium. HUVEC tubular, capillary-like structures were observed only in co-culture. Scale bars = 100μm. N=3, with representative images shown. **(b)** HUVEC-myeloma-MSC tri-cultures in hydrogels do not mimic angiogenesis. Confocal images of GFP-MM1S (green), RFP^+HUVECs (blue) and DiR^+MSCs (red) after 24 hours of mono-culture, co-culture or tri-culture in endothelial cell medium. Scale bars = 150 μm. N=6, with representative images shown.

Supplemental Figure 3. BLI quantification of MM1S in 2D and 3D culture in MSC expansion media. (a) MSCs protected GFP^+Luc^+MM1S from bortezomib on scaffolds over 3 weeks only in 3D cultures. Statistically significant increase (*,$p<0.05$) was found at week 3 ($MM1S^+MSCs^+$ Bortezomib vs $MM1S^+$Bortezomib, 2-way ANOVA, Dunnett's post-hoc test). **(b)** In 2D, no differences were found between GFP^+Luc^+MM1S with bortezomib, with or without

MSCs (using a 2-way ANOVA with Dunnett's post-hoc test). No MM1S BLI signal was measurable at 48 hours. Data is mean +/- SEM, n≥3. Experiments were repeated at least 3 times.

Supplemental Figure 4. Confocal Microscopy Imaging shows Primary Patient CD138$^+$ cells alive at Day 4 in 50-50 cell growth media. Top: Overlays, Bottom: Separated Channels. **(a)** Green DiI MM cells, Red DiD MSCs, Royal Blue Scaffold. **(b)** Red DiD-MSCs, Green DiI MM cells. **(c)** Cyan Calcein Live cell stain, Green DiI MM cells, **(d)** Cyan Calcein Live cell stain, Red DiD MSCs. Boxes 1 and 2 denote viable MM cells. Scale bar=100μm. **(e)** Higher magnification of Box 1, Scale=50 μm. **(f)** Higher magnification of Box 2, Scale=10 μm. Cyan calcein live cell stain, Red DiD MSCs, Green DiI MM cells and arrows indicate live myeloma cells. N=3 donors, with representative images shown.

Supplemental Figure 5. Confocal Microscopy Imaging shows Primary Patient CD138$^+$ cells cultured on ND-MSCs alive at Day 7 in 50-50 cell growth media. Maximum projections of z-stack confocal images. **(a)** Overlay and **(b)** individual channels of confocal imaging at day 7. Green DiI MM cells, Red DiD MSCs, Blue calcein stain of live cells. Scale=100 μm. Higher magnification of (a) shown in **(c)**, red box indicates a live MM cell, Scale= 10μm**.** **(d)** Higher magnification of (c) with added channel for scaffold autofluorescent signal (maroon). **(e,f**) Max projections of z-stack confocal images, individual channels and overlay. Autofluorescence of silk scaffolds (blue), patient-derived primary MM cells (DiI, cyan), calcein labeling for live cells (green), ND-MSCs (DiD, red), and merged images. **(f)** Higher magnification of (e). Two live MM cells are identified as calcein positive, DiI postive and DiD-negative, shown in the red box. Scale=10 μm. N=3 donors, with representative images shown.

Supplemental Figure 6. Histological analysis of Primary MM cells on scaffolds, Day 11. Primary MM cells (green arrows) and ND-MSCs (red arrows) on scaffolds (yellow arrows) after 11 days of co-culture in 50-50 cell growth media. H&E (60x) and CD138 (brown, nuclei counterstain blue) indicate stroma and myeloma cells. Scale= 50 µm (60X); Scale=10 µm (100X). N=3 donors, with representative images shown.

Supplemental Figure 7. Decreased proliferation of MM-MSCs vs ND-MSCs. a) Representative images of ND-MSCs and MM-MSCs after 9 days of culture with (bottom) or without (top) MM1S cells. Scale bar=100µm. **(b)** Quantification of MSCs at day 9 plotted as mean+/-SEM of Hoescht-stained cells relative to ND-MSCs Alone. Decreased proliferation of MM-MSCs vs ND-MSCs, and decreased proliferation of ND-MSCs when co-cultures with myeloma cells (MM1S) was observed. Statistical analysis was done using Ordinary one-way ANOVA with Fisher's LSD post-hoc testing (**$p \leq 0.05$, ****$p \leq 0.001$).**(c**) Patient samples (MM-MSCs) and Normal donor (ND-MSCs) at days 6 and 9 show decreased proliferation of MM-MSCs vs ND-MSCs using cell count/cm^2. Statistical significance was determined using two 2-tailed t-tests with α=0.05, p= 0.009 day 6 and p= 0.001, day 9. All samples were grown in 50-50 cell growth media.

Supplemental Figure 8. Myeloma Inhibits MSC Osteogenesis. **(a)** ND-MSCs or MM-MSCs were cultured in osteogenic media containing dexamethasone and stained at day 1 and 10 for mineralization using Alizarin Red. Representative images of n=3 shown here. Only ND-MSCs produced mineralization consistently, while MM-MSCs produced no, or minimal, mineralization. **(b)** ND-MSCs and MM-MSCs were cultured alone (top) or in direct co-culture

with MM1S (bottom) in osteogenic dexamethasone-free media for 10 days. MM1S inhibited the ability of ND-MSCs to produce mineralization. MM-MSCs did not produce mineralization in the absence or presence of MM1S. Shown are representative images of n≥3 normal or myeloma donors, 10X objective.

Supplemental Figure 9. mRNA profiling of MM vs ND-MSCs. (a) Unsupervised clustering distinguishes MM- and ND-MSCs (passage 2) based on 230 cancer-related mRNAs (Nanostring analysis). **(b)** Of these, 49 mRNAs were significantly different ($p<0.05$, ≥1.3 fold change, MM- vs ND-MSCs).

Supplemental Figure 10. MicroRNA transcript levels increased with miR mimic transfection. miRvana microRNA mimics increased the expression of miRs after 10 days of culture measured by q-RT-PCR, demonstrating use of microRNA mimics to increase microRNA concentrations within cells for a 10 day period. Data plotted as mean fold increase above the negative miR control mean +/- SEM.

Supplemental Video 1. RFP^+HUVECs and GFP^+MM1S Co-cultures. Fly-through of confocal z-stack images at day 9 of co-cultures in endothelial medium. RFP^+ HUVECS (red), GFP^+MM1S cells (green) and silk scaffold (blue). GFP^+MM1S cells can be seen intermingled in with tube-like structures formed by RFP^+HUVECs, suggesting myeloma support of angiogenesis. Representative image of n=3 shown here.

Supplemental Video 2. TurboRFP MSCs grown in co-culture with GFP-MM1S for 4 weeks. 3D max projection reconstruction of confocal microscopy z-stack images. Few MSCs (red) can be seen when in co-cultured with GFP-MM1S (green) on scaffolds (blue) in osteogenic (dexamethasone free) media. Representative image of n=3 shown here.

Supplemental Video 3. TurboRFP MSCs grown alone on scaffolds for 4 weeks. 3D maximum projection reconstruction of confocal microscopy z-stack images. MSCs in monoculture (red) are seen stretched across and throughout the scaffold (blue), confluent within the pores of the silk matrix in osteogenic (dexamethasone free) media. Representative image of n=3 shown here.

Supplemental Table I

Gene	Accession Number	Forward Primer	Reverse Primer
ALP	NM_000478	5’-CTATCCTGGCTCCGTGCTC-3’	5’-GCTGGCAGTGGTCAGATGTT-3’
BSP	NM_004967	5’-AAACGATTTCCAGTTCAGGG-3’	5’-TGAAGTCTCCTCTTCTTCCTCCT-3’
GAPDH	NM_002046	5’-AAGGTGAAGGTCGGAGTCAA-3’	5’-AATGAAGGGGTCATTGATGG-3’
COL1A1	NM_000088	5’-AAGAGGAAGGCCAAGTCGAG-3’	5’-CACACGTCTCGGTCATGGTA-3’
RUNX2	NM_001015051	5’-CAGTAGATGGACCTCGGGAA-3’	5’-CCTAAATCACTGAGGCGGTC-3’
OP	NM_000582	5'-CTGCTGACAACCAAGCCC-3'	5'-GGGCTTGGTTGTCAGCAG-3'
OC	NM_199173	5'-ATCTCAGCCTGGAACCAACA-3'	5'-TCTGCCAGTCCCCCTAGAC-3'
MicroRNAs			
RNU6B		5’CGCAAGGATGACACGCAAATT-3’	----------
URP		----------	5’-GTG CAG GGT CCG AGG-3’
hsa-mir-199a-5p	MIMAT0000231	5’-CCCAGTGTTCAGACTACCTGTTC-3’	----------
hsa-mir-199a-3p	MIMAT0000232	5’-ACAGTAGUCTGCACATTGGTTA-3’	----------
hsa-mir-24-3p	MIMAT0000080	5’-TGGCTCAGTTCAGCAGGAACAG-3’	----------
hsa-mir-15a-5p	MIMAT0000068	5’- TAGCAGCACATAATGGTTTGTG-3’	----------
hsa-mir-16-5p	MIMAT0000069	5’-UAGCAGCACGUAAAUAUUGGCG-3’	----------

Supplemental Table II

miRNA Name	Mean MSCs Alone	StDev MSCs Alone	Mean MSCs+MM1S	StDev MSCs+MM1S	Fold change	P-value, t-test
hsa-miR-221-3p	4974.308333	1390.263215	1565.023333	497.8060553	-3.17842	0.0002109
hsa-miR-27b-3p	813.4266667	186.4461039	267.0783333	79.01389888	-3.04565	6.011E-05
hsa-miR-337-5p	417.725	151.9724879	165.2416667	60.86200635	-2.52796	0.0036148
hsa-miR-409-3p	390.7566667	122.1589659	154.985	54.35614473	-2.52125	0.0015147
hsa-miR-485-3p	203.8183333	60.59484678	82.53833333	29.55104426	-2.46938	0.0013215
hsa-miR-376a-3p	364.22	137.0112222	173.9133333	63.76792161	-2.09426	0.0115501
hsa-let-7b-5p	9429.895	1911.551159	4517.905	1488.427844	-2.08723	0.0005647
hsa-miR-196a-5p	252.925	82.59200948	124.2583333	27.93952141	-2.03548	0.0047308
hsa-miR-199a-5p	**2100.938333**	**517.9727653**	**1040.423333**	**200.0690177**	**-2.01931**	**0.0008697**
hsa-miR-593-3p	69.49	30.92600783	35.26833333	7.881242076	-1.97032	0.0253106
hsa-miR-299-5p	126.935	43.84101493	64.94166667	30.15773759	-1.9546	0.0171406
hsa-miR-376c	185.04	75.70317325	95.875	20.47333852	-1.93001	0.0192839
hsa-miR-337-3p	254.0833333	69.47844232	131.8783333	37.41578727	-1.92665	0.0035242
hsa-let-7c	308.24	136.5683915	162.9016667	33.51580369	-1.89218	0.0297858
hsa-miR-27a-3p	179.3116667	39.62781267	94.80166667	16.96313699	-1.89144	0.0007212
hsa-miR-382-5p	213.3116667	64.73086232	120.8	40.87706203	-1.76583	0.0142891
hsa-let-7a-5p	11633.815	3103.012633	6631.48	1059.904462	-1.75433	0.0038667
hsa-miR-543	94.05	26.28140027	53.94333333	18.17416922	-1.7435	0.01175
hsa-miR-432-5p	114.0416667	32.45264453	67.80833333	16.94439071	-1.68182	0.0113784
hsa-miR-196b-5p	162.5316667	29.59327181	97.215	14.78868453	-1.67188	0.0006855
hsa-miR-487b	124.9966667	46.05830855	76.91666667	22.50025126	-1.62509	0.044442
hsa-miR-370	48.6	13.12209435	31.21166667	8.067216166	-1.55711	0.019954
hsa-miR-140-5p	265.1933333	67.57307827	172.2166667	69.95542943	-1.53988	0.0412292
hsa-miR-409-5p	67.78666667	17.49547332	44.17	9.458659524	-1.53468	0.0156012
hsa-miR-26a-5p	227.585	49.30947769	149.675	67.01744362	-1.52053	0.0447343
hsa-miR-548x-3p	49.63833333	13.27809838	74.67833333	11.65988751	1.504449	0.0060113
hsa-miR-342-3p	94.08833333	28.1914678	141.7683333	31.48714431	1.506758	0.020012
hsa-miR-587	32.12666667	12.35509072	48.535	10.44662003	1.510739	0.0323143
hsa-miR-548t-5p	31.49666667	7.9735981	47.655	14.67739589	1.513017	0.0393071
hsa-miR-30e-5p	63.53	16.14146833	96.41	13.71150612	1.517551	0.00347
hsa-miR-627	27.87666667	5.588730327	42.42666667	14.74598612	1.521942	0.0473637
hsa-miR-4531	20.73	5.494484507	31.62166667	8.132707831	1.525406	0.0216254
hsa-miR-891b	35.97666667	7.871840107	55.77166667	10.45944055	1.550218	0.0040816
hsa-miR-579	73.47666667	15.464819	118.4983333	14.56459875	1.612734	0.0004064
hsa-miR-3195	37.42	17.79964943	60.98666667	13.13430572	1.629788	0.0260599
hsa-miR-297	19.85666667	6.186429234	32.55666667	7.144434664	1.639584	0.0081269
hsa-miR-19b-3p	204.1066667	43.10502368	336.4483333	122.383067	1.648395	0.0315347
hsa-miR-23c	31.05	5.400307399	51.395	14.10744732	1.655233	0.0080261
hsa-miR-188-5p	28.90333333	3.403061367	50.15666667	19.38931527	1.735325	0.0245415
hsa-miR-1202	23.39666667	8.82328208	40.97166667	5.838168948	1.751175	0.0022537
hsa-miR-181a-5p	**479.2183333**	**160.4278161**	**848.6683333**	**178.085813**	**1.770943**	**0.0036284**
hsa-miR-4286	128.1783333	43.67348368	232.89	64.87249309	1.816922	0.0082921
hsa-miR-20a-5p+hsa-miR-2(	122.53	10.47527374	234.455	56.30517161	1.91345	0.0007379
hsa-miR-186-5p	44.80833333	17.02545203	90.115	27.59766639	2.011121	0.0065209
hsa-miR-144-3p	108.485	42.33260717	221.5283333	78.91516975	2.042018	0.0114046
hsa-miR-520d-5p+hsa-miR-!	26.7	8.850059887	56.23166667	21.01163241	2.106055	0.0099406
hsa-miR-181c-5p	**16.985**	**4.831354882**	**36.26166667**	**10.96183637**	**2.134923**	**0.0027676**
hsa-miR-222-3p	**911.0383333**	**156.6530427**	**1960.863333**	**652.9397906**	**2.152339**	**0.0033204**
hsa-miR-30d-5p	43.88666667	11.44991645	107.3466667	29.83796351	2.445997	0.0006577
hsa-miR-30a-5p	125.9866667	48.99054834	319.8816667	106.922229	2.539012	0.0023679
hsa-miR-601	**33.98333333**	**9.909913555**	**86.51833333**	**37.12728669**	**2.545905**	**0.0073805**
hsa-miR-630	85.865	20.15764942	376.5816667	296.0230356	4.385741	0.0373142
hsa-miR-146a-5p	**36.10333333**	**11.26964537**	**620.07**	**385.6750977**	**17.17487**	**0.0040594**

miRNA Name	Mean ND	StDev ND	Mean MM	StDev MM	Fold Change	P-value, t-test
hsa-miR-143-3p	1228.57	412.6898	306.992857	258.6299	-4.00195	0.0440827
hsa-miR-199a-5p	**220.69667**	**20.64233**	**115.14**	**46.38334**	**-1.916768**	**0.00115665**
hsa-miR-15a-5p	286.44	47.8235	132.668571	67.31972	-2.159064	0.00764575
hsa-miR-24-3p	333.55667	32.71614	192.597143	66.61681	-1.731888	0.00240849
hsa-miR-374a-5p	209.77	30.22188	102.584286	81.93849	-2.044855	0.01668609
hsa-miR-148a-3p	164.06333	10.3563	59.8642857	32.63697	-2.740588	6.9614E-05
hsa-miR-424-5p	75.83	19.75872	24.0257143	9.983722	-3.156202	0.03420566
hsa-miR-1246	41.383333	7.936034	132.822857	72.43337	3.2095737	0.01530302
hsa-miR-222-3p	**257.88667**	**78.74417**	**469.518571**	**122.7901**	**1.8206392**	**0.01680615**
hsa-miR-181a-5p	**159.00667**	**55.46172**	**507.212857**	**297.7504**	**3.1898842**	**0.02106839**
hsa-miR-127-3p	88.033333	59.29415	300.311429	162.6742	3.4113377	0.0166669
hsa-miR-146a-5p	**5.2166667**	**1.629734**	**80.09**	**67.57914**	**15.352716**	**0.02622689**
hsa-miR-574-5p	63.396667	3.026489	199.668571	135.0669	3.1495121	0.03705204
hsa-miR-382-5p	41.116667	21.42598	133.225714	51.74707	3.2401876	0.00411696
hsa-miR-320e	34.836667	19.41744	122.062857	90.16852	3.5038616	0.04476998
hsa-miR-151a-3p	23.5	5.700167	41.3585714	14.34395	1.7599392	0.02268311
hsa-miR-433	5.63	1.939897	25.3928571	19.31754	4.5102766	0.03520007
hsa-miR-601	**15.806667**	**5.84275**	**57.4871429**	**37.02822**	**3.6368922**	**0.02449335**
hsa-miR-1180	6.7366667	2.532456	19.46	9.008366	2.888669	0.00955829
hsa-miR-548al	11.906667	2.245915	41.4542857	28.14633	3.4816029	0.032017
hsa-miR-769-5p	4.3633333	1.249253	13.6842857	5.454328	3.1361999	0.0034423
hsa-miR-4284	6.2533333	2.48846	13.13	6.512877	2.0996802	0.04233391
hsa-miR-329	5.3433333	1.307147	11.3742857	5.498842	2.1286873	0.02825865
hsa-miR-4488	8.15	1.345102	23.3471429	12.71855	2.8646801	0.01926713
hsa-miR-323a-3p	7.2033333	3.424534	19.78	13.06124	2.7459509	0.04763291
hsa-miR-3185	5.5066667	2.443856	15.0271429	9.863733	2.7289	0.04646598
hsa-miR-1915-3p	17.103333	2.493438	57.4271429	24.00118	3.3576579	0.00412051
hsa-miR-656	8.65	2.061723	19.3642857	9.985723	2.2386457	0.0301359
hsa-miR-1273a	7.8633333	0.300888	21.4642857	12.01318	2.7296675	0.02413251
hsa-miR-151a-5p	14.946667	5.439617	29.6442857	11.73355	1.9833376	0.02780443
hsa-miR-216b	8.5966667	2.864827	26.4957143	19.21622	3.0820916	0.04945125
hsa-miR-212-3p	6.3066667	0.420634	18.3014286	10.69328	2.9019178	0.02498922
hsa-miR-1268a	8.2933333	1.395182	23.57	15.40778	2.8420418	0.03940269
hsa-miR-187-3p	12.673333	2.425064	33.6685714	18.90175	2.6566469	0.0257773
hsa-miR-370	3.97	1.921588	15.5757143	11.36159	3.9233537	0.03577152
hsa-miR-550b-3p	5.9333333	1.665303	12.3885714	5.027512	2.0879615	0.01649711
hsa-miR-320a	6.2566667	1.425143	17.5571429	9.26659	2.8061496	0.01759519
hsa-miR-1290	5.1466667	0.728858	19.6085714	15.50828	3.8099556	0.04865356
hsa-miR-181c-5p	**10.306667**	**3.588319**	**31.7257143**	**11.15009**	**3.0781741**	**0.00192591**
hsa-miR-487a	4.56	2.352169	16.5371429	9.238141	3.6265664	0.01394082
hsa-miR-1973	6.22	0.744849	16.9685714	10.57067	2.7280661	0.03599131

Supp Figure 1

A

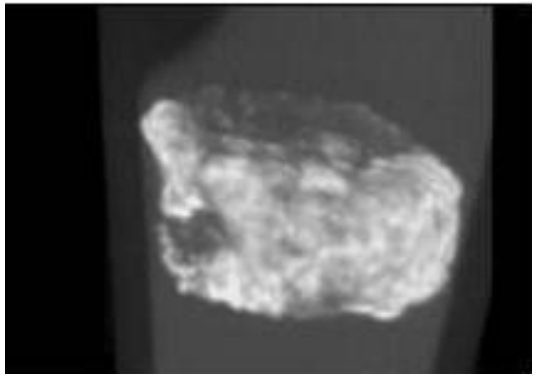

Day 50

B

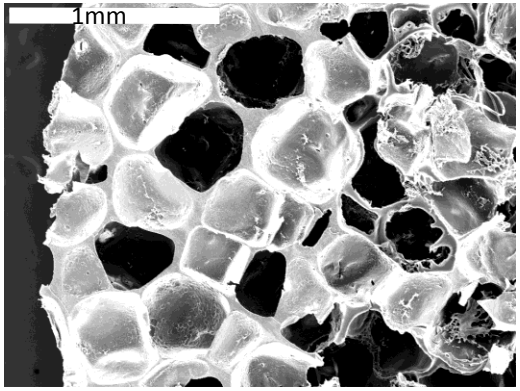

Day 2

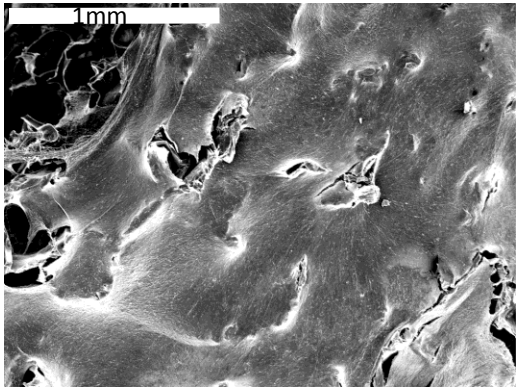

Day 37

Supp Figure 2

A

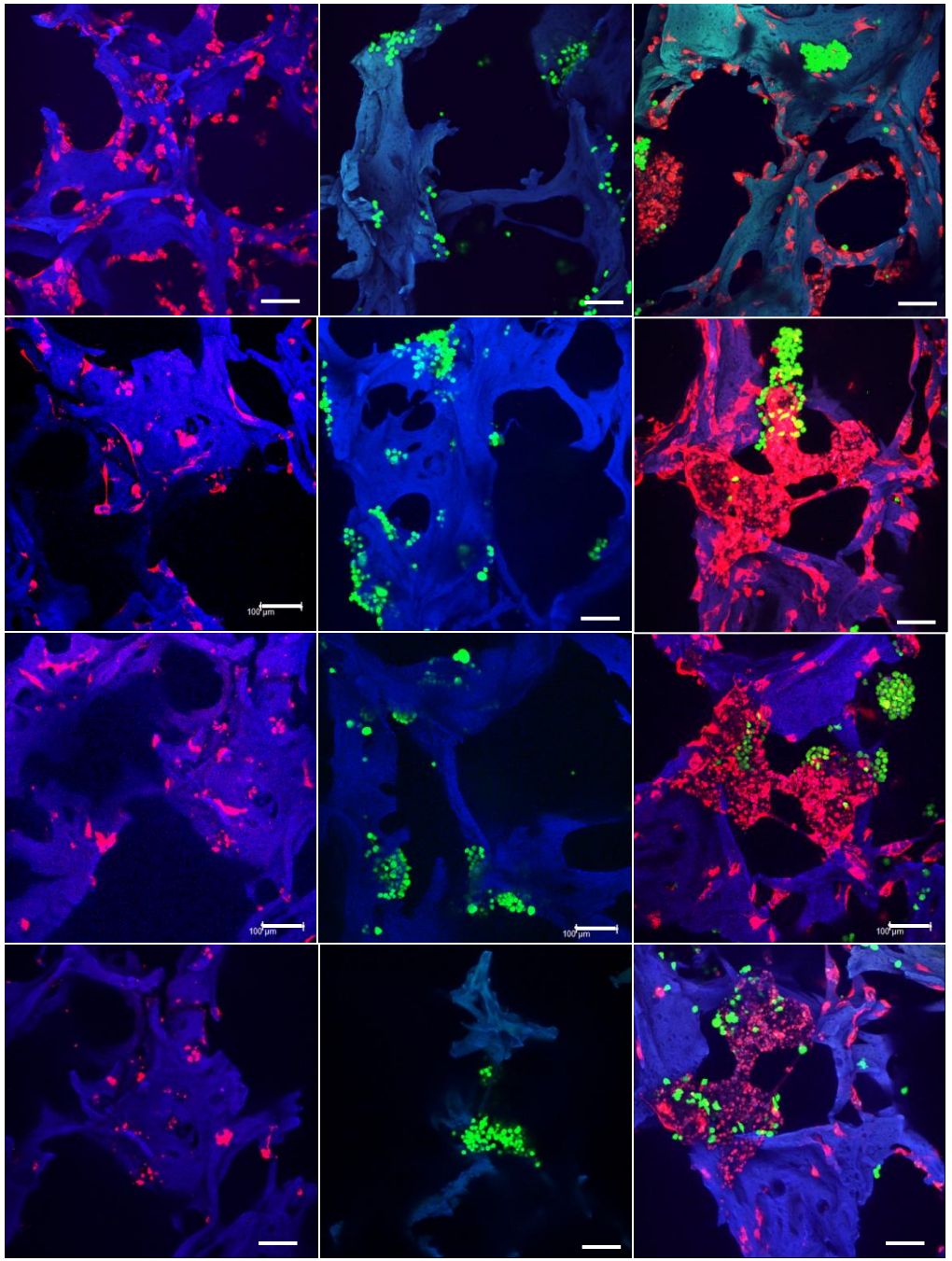

Supp Figure 2

B

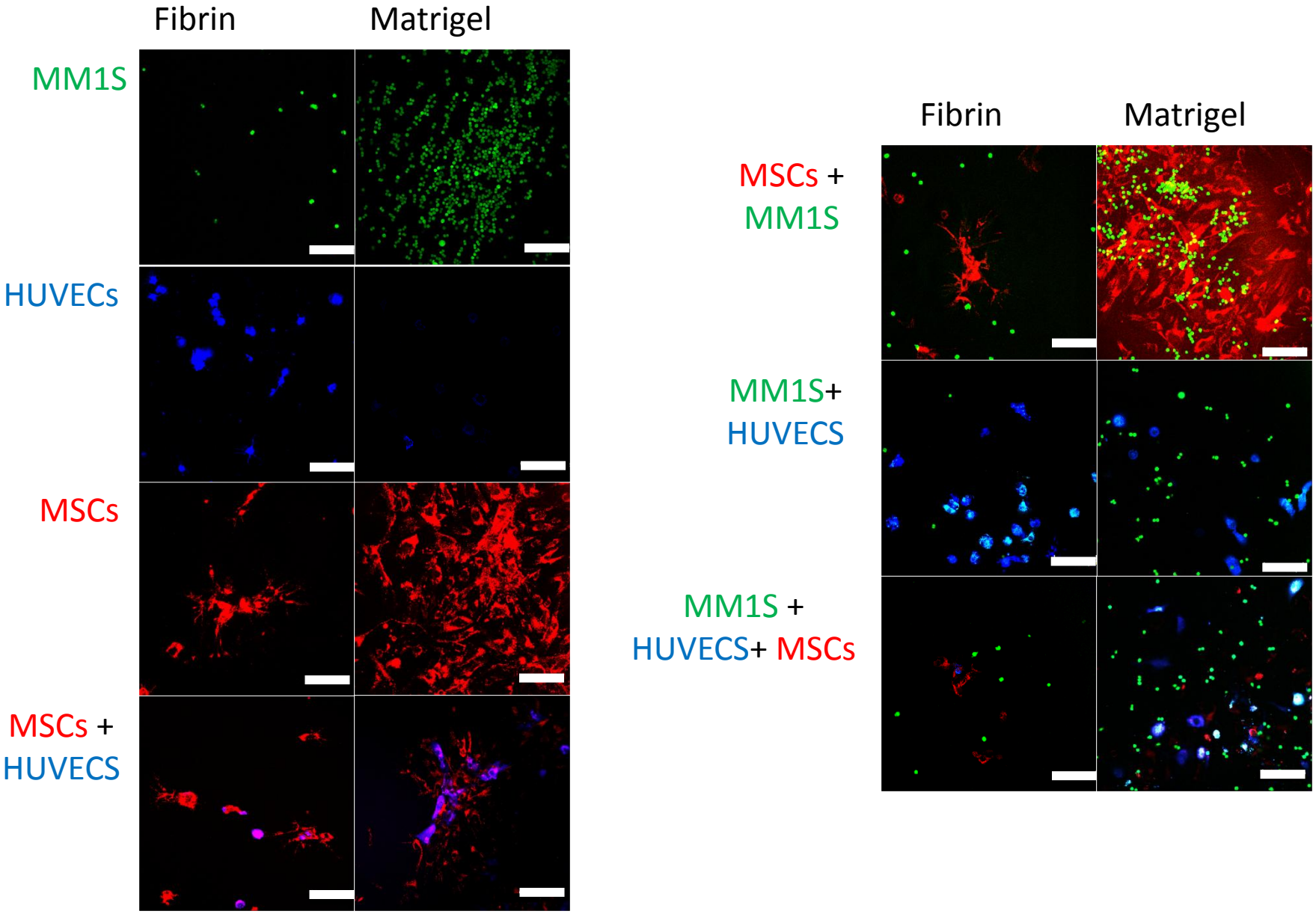

Supp Figure 3

A

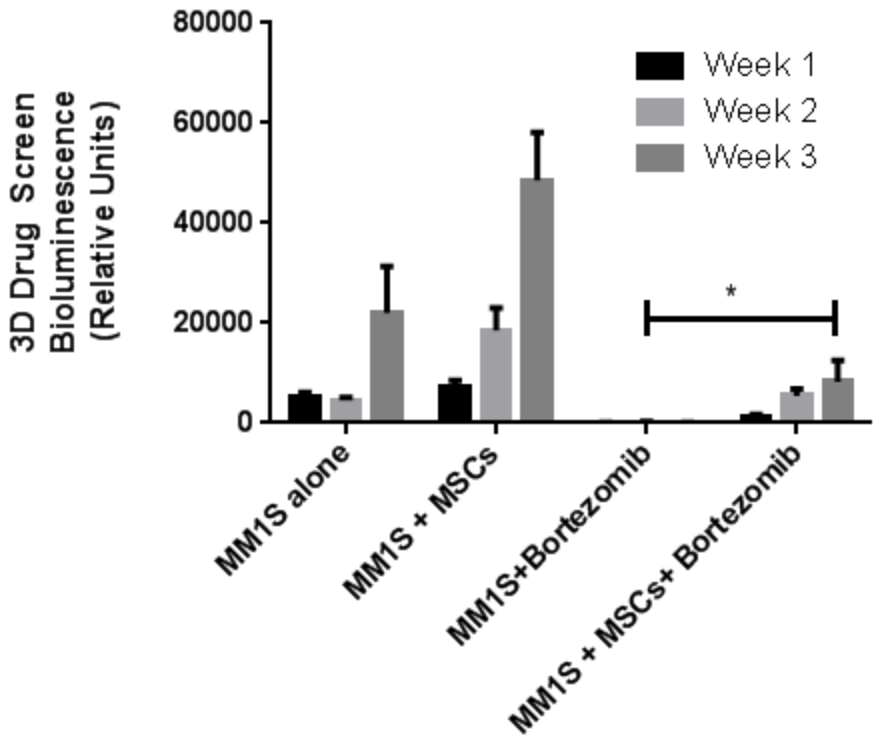

B

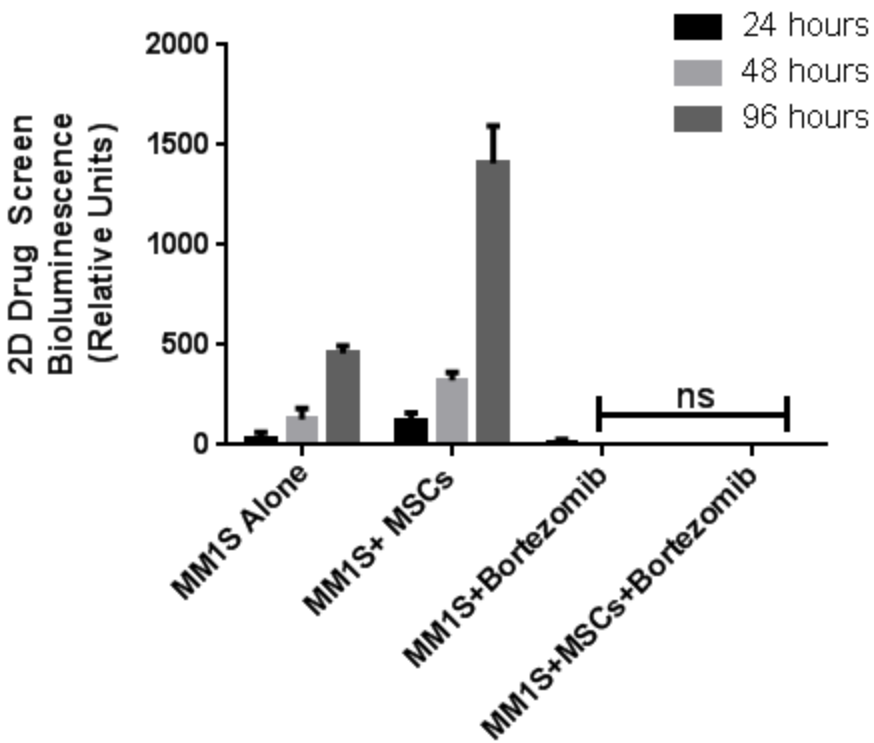

Supp Figure 4

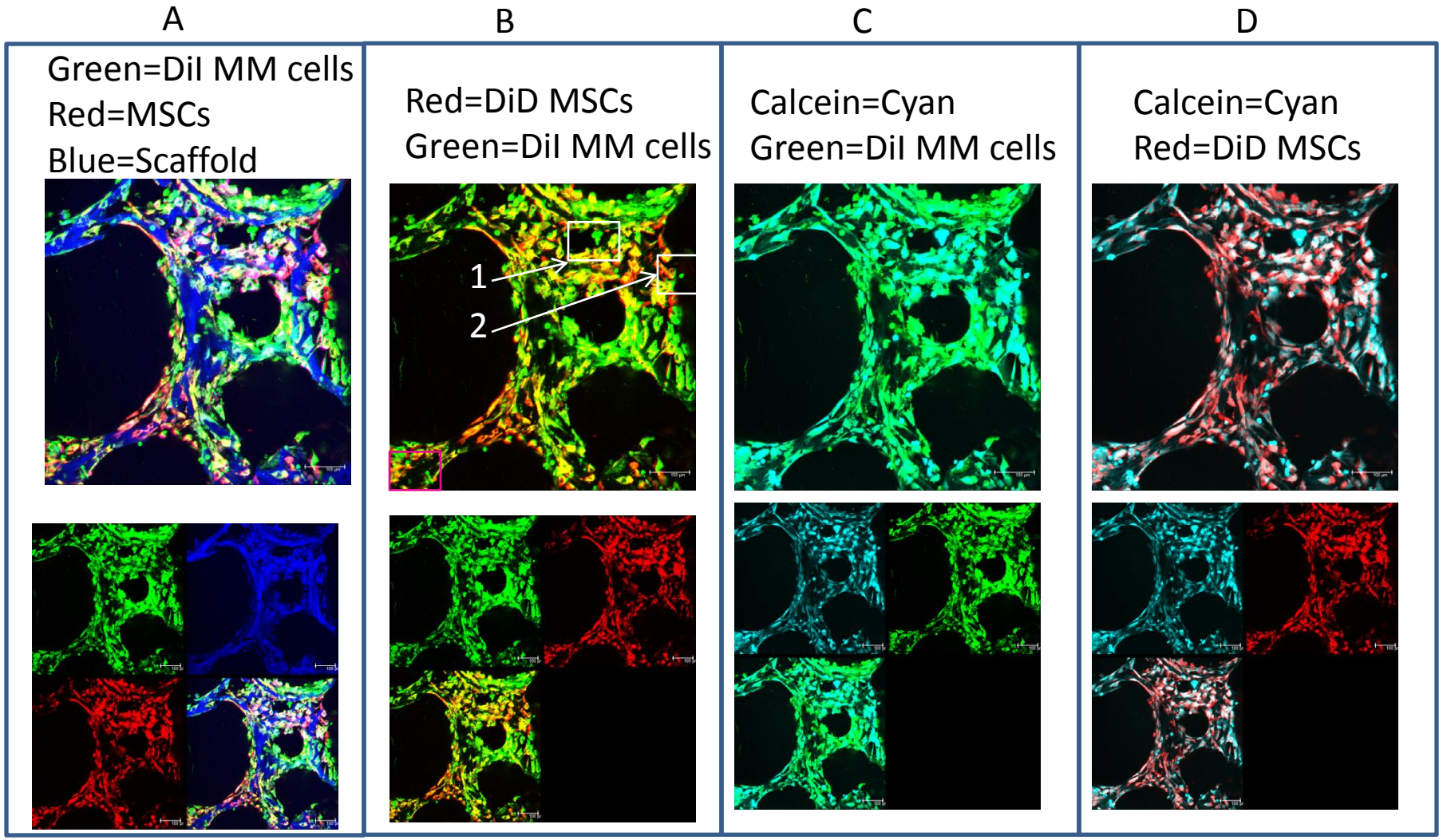

Supp Figure 4

E Calcein, Live cells DiI MM cells

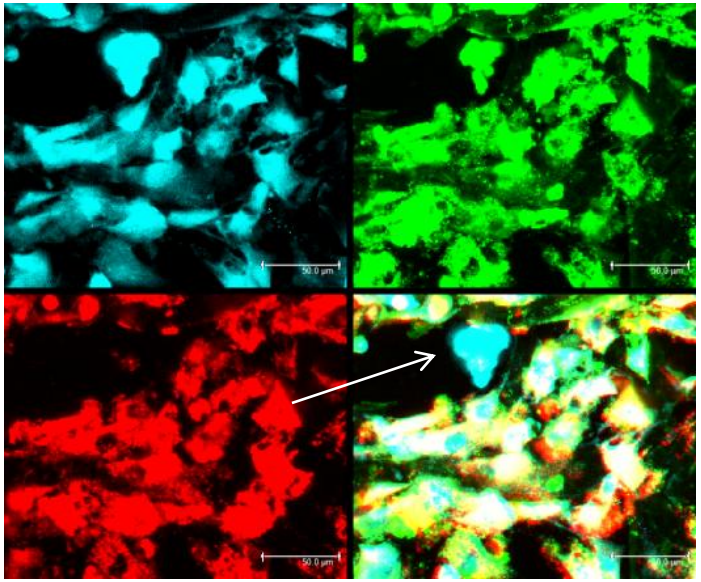

DiD MSCs Merge

F Calcein, Live cells DiI MM cells

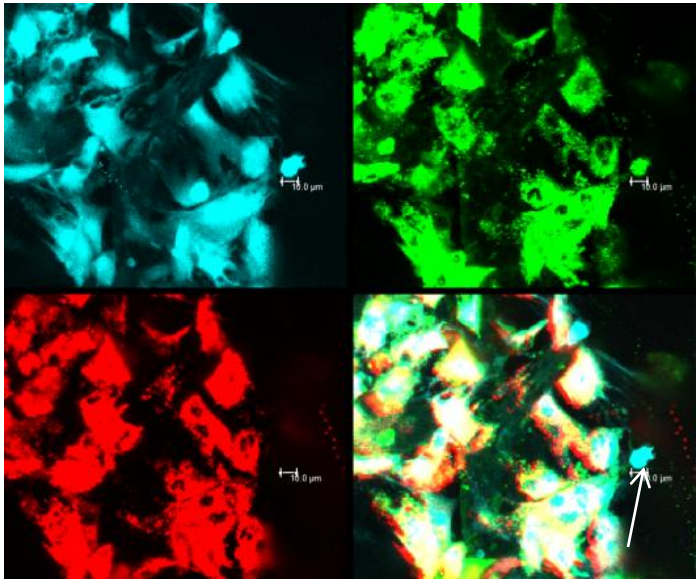

DiD MSCs Merge

Supp Figure 5

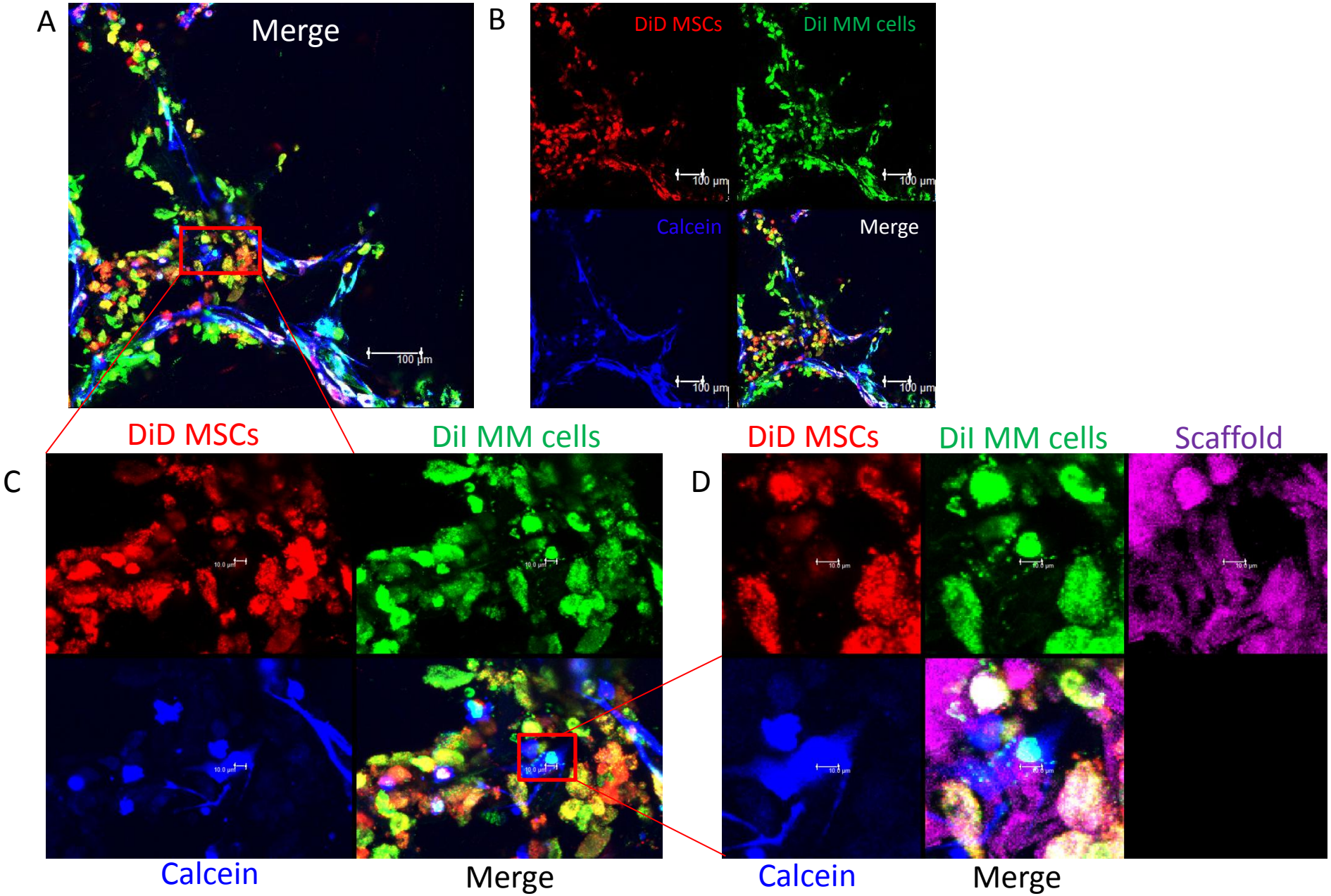

Supp Figure 5

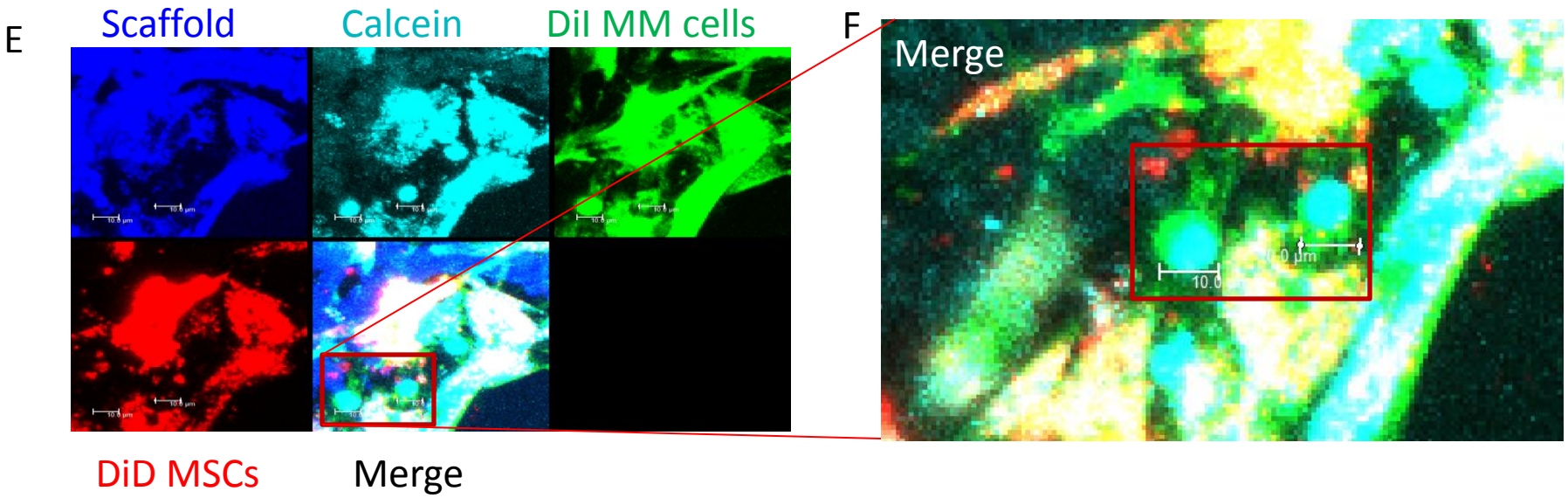

Supp Figure 6

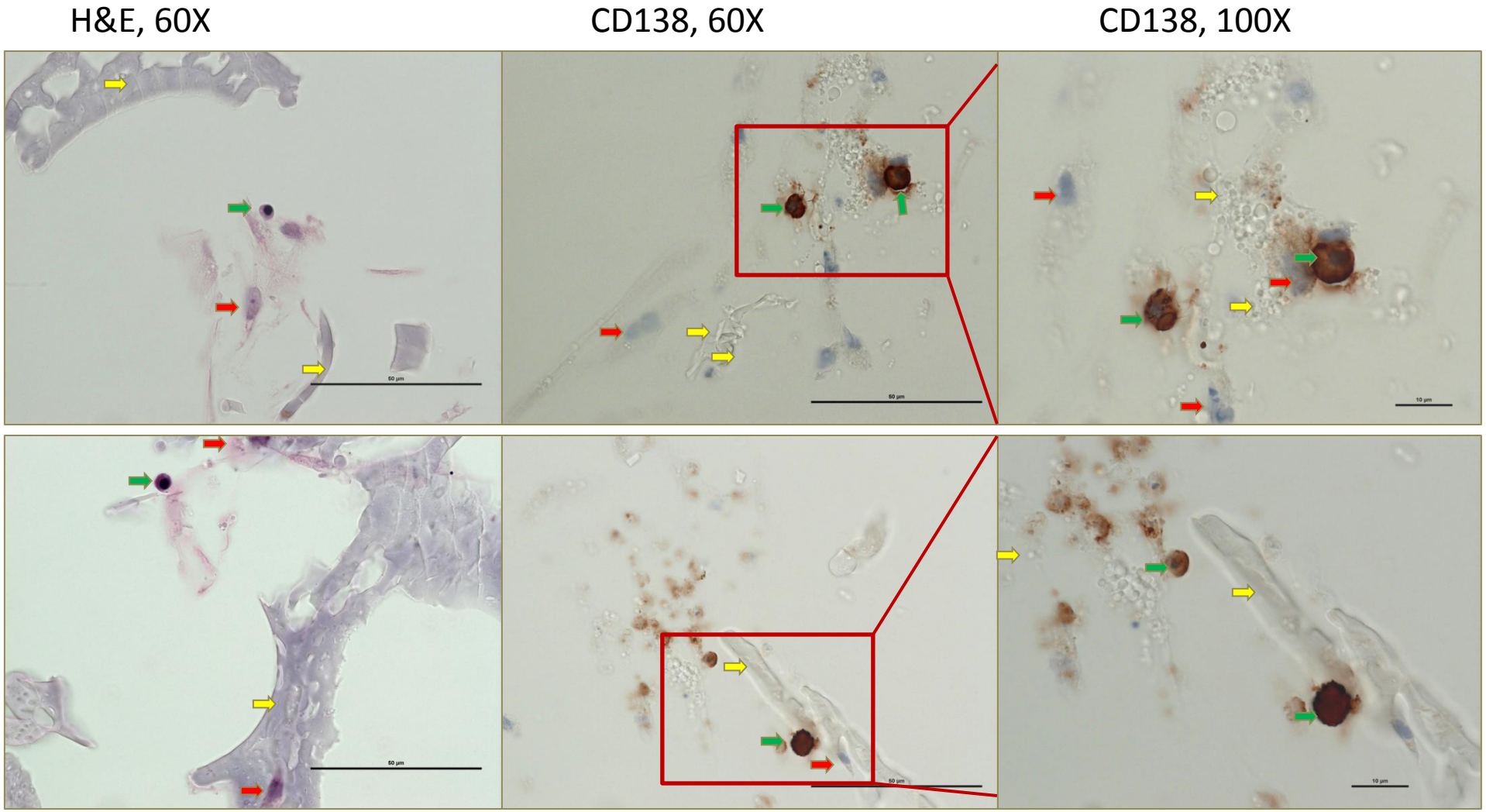

Supp Figure 7

A

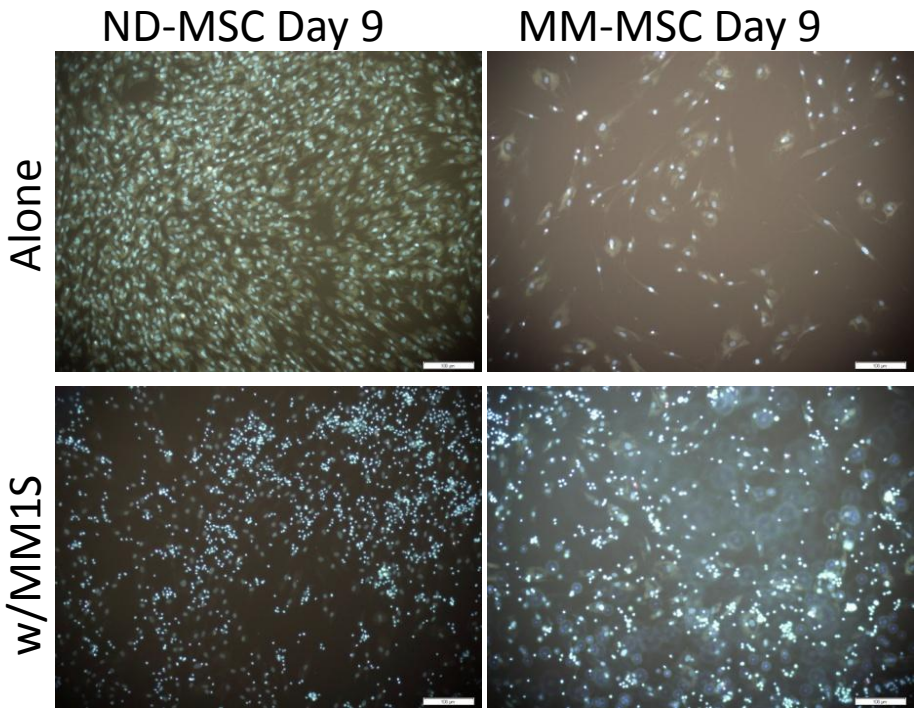

B

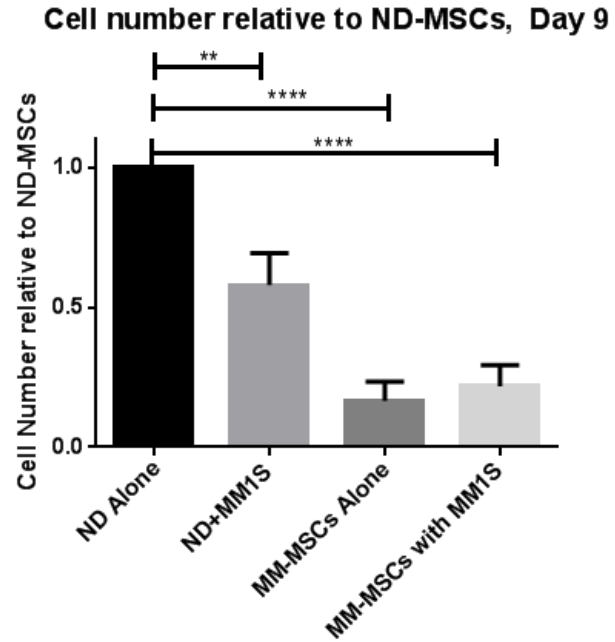

C

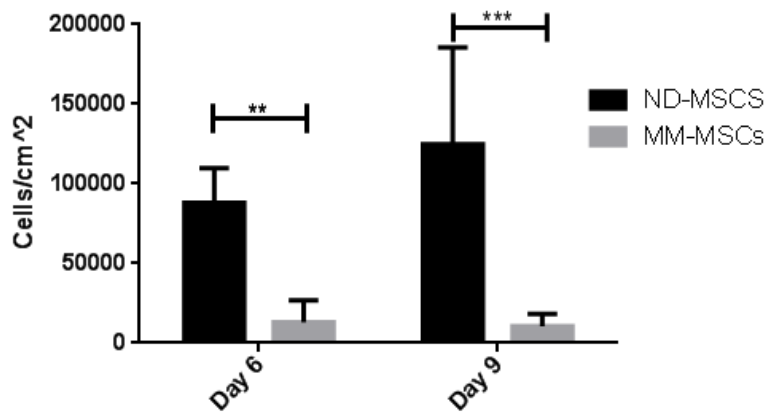

Supp Figure 8

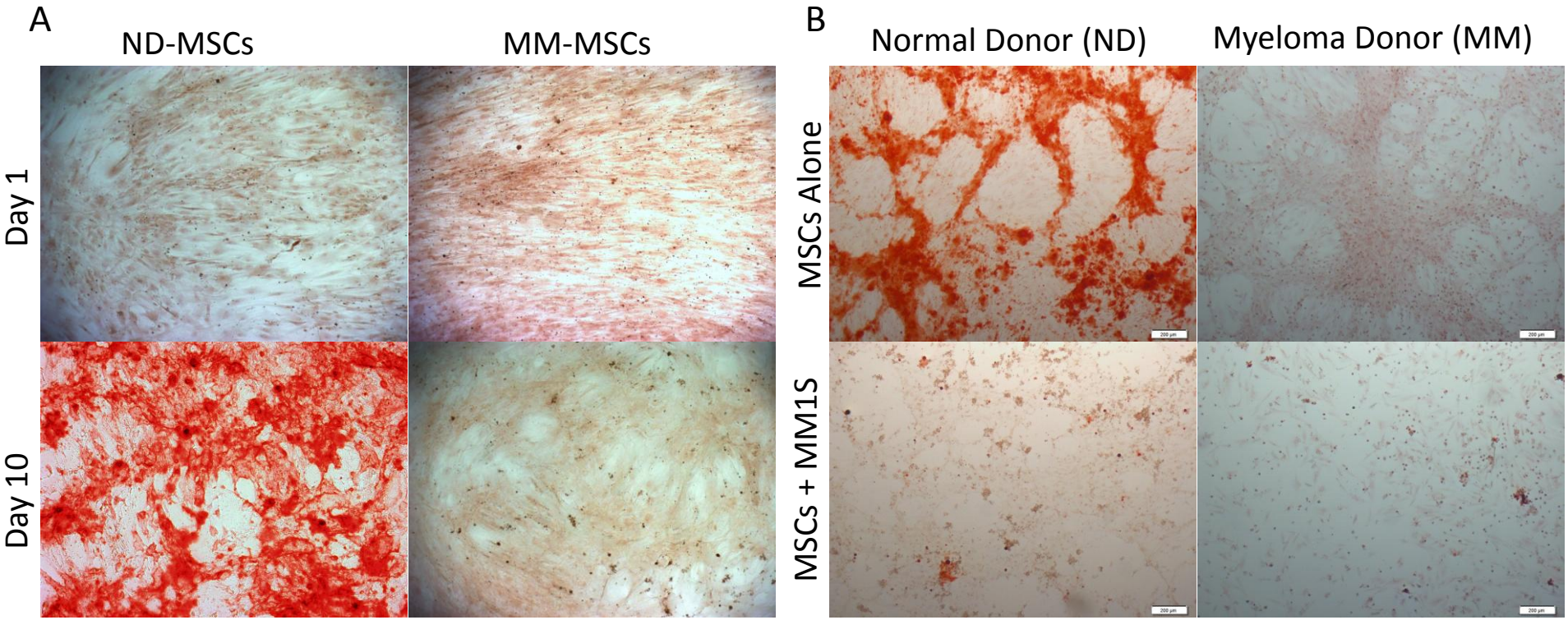

Supp Figure 9

A

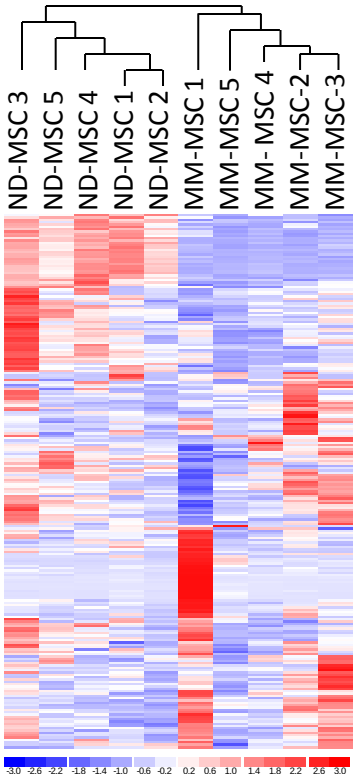

B

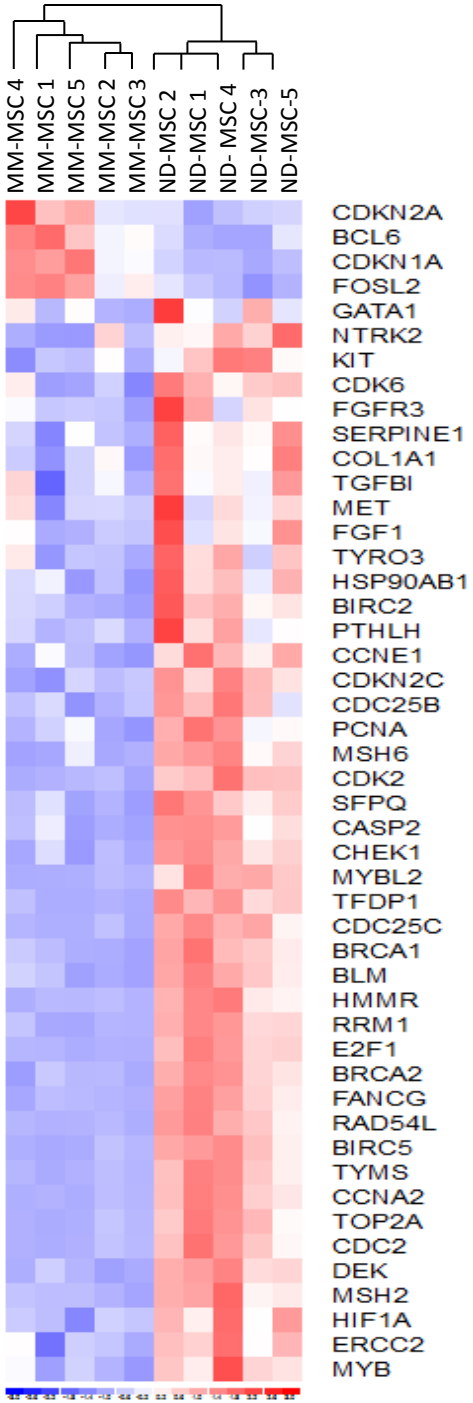
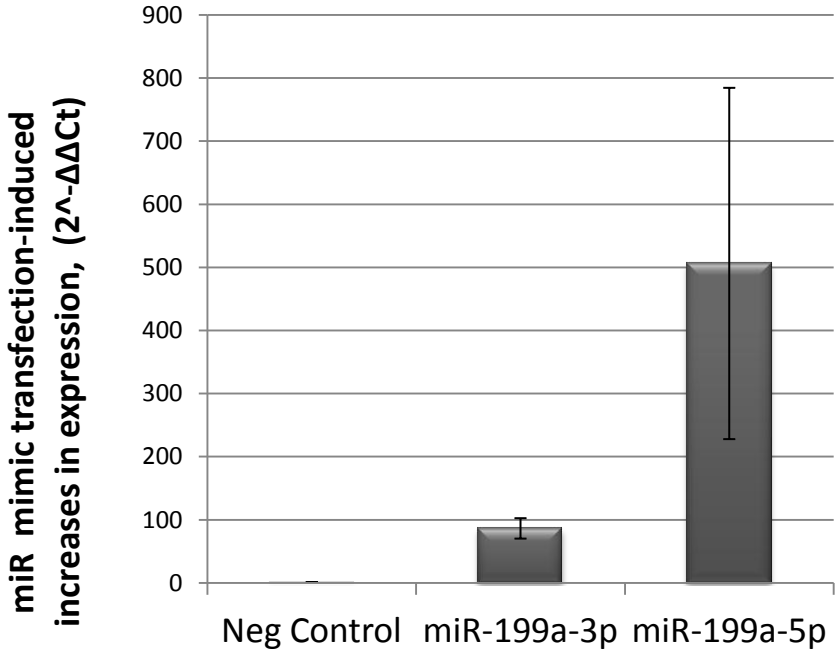
Supp Figure 10